STRUCTURED EPITAXIAL GRAPHENE FOR ELECTRONICS

A Thesis
Presented to
The Academic Faculty

by

Ming Ruan

In Partial Fulfillment
of the Requirements for the Degree
Doctor of Philosophy in the
School of Physics

Georgia Institute of Technology
August 2012

STRUCTURED EPITAXIAL GRAPHENE FOR ELECTRONICS

Approved by:

Walt A. de Heer, Committee Chair
School of Physics
Georgia Institute of Technology

Walt A. de Heer, Advisor
School of Physics
Georgia Institute of Technology

Zhigang Jiang
School of Physics
Georgia Institute of Technology

Phillip N. First
School of Physics
Georgia Institute of Technology

Edward H. Conrad
School of Physics
Georgia Institute of Technology

John D. Cressler
School of Electrical and Computational Engineering
Georgia Institute of Technology

Date Approved: 28 June 2012

To my parents,

Weihong Han and Peiguo Ruan

ACKNOWLEDGEMENTS

I graciously thanks my advisor, Dr. Walt A. de Heer for his mentoring and support on my graduate study. I also would like to thank my other mentors, Dr. Claire Berger and Dr. Xiaosong Wu for their coaching on my research. I would like to express my appreciation to my committee, Dr. Edward Conrad, Dr. Philip First, Dr. Zhigang Jiang and Dr. John D. Cressler.

I am grateful to the colleages that I worked closely in the past five year: Dr. Mike Sprinkle, Dr. Xuebin Li, Dr. Fan Ming, Yike Hu, John Hankinson, Jeremy Hicks, Baiqian Zhang, James Palmer, Zelei Guo, Dr. Rui Dong, Dr. Farhana Zaman, Dr. Miguel Rubio Roy and Andrei Savu. I am also grateful to former and current members in collaborating groups: Dr. Joanna Hass, Dr. Nikhil Sharma, Dr. D. Lee Miller Dr. Kevin Kubista, D. Britt Torrance, Tien Hoang, Dr. Anton N. Sidorov, Wenlong Yu, Chris Malec, Lede Xian, Dr. Jia-an Yan, and Holly Tinkey. Without their generous help, none of my work could have been finished. I also would like to thank all members in the graphene journal club for the informative discussions and the Georgia Tech cleanroom staff for their help on my experients.

I would like to thank my friends who were not included in the previous list, Danjue Chen, Chenyi Pan, and especially, Lian Duan, for their support over these years. Last but not least, I would like to thank my parents, Weihong Han and Peiguo Ruan, who raised me and give me unconditional support since the first day of my life.

TABLE OF CONTENTS

LIST OF TABLES

LIST OF FIGURES

SUMMARY

After the pioneering investigations into graphene-based electronics at Georgia Tech, great strides have been made developing epitaxial graphene on silicon carbide (EG) as a new electronic material. EG has not only demonstrated its potential for large scale applications, it also has become an important material for fundamental two-dimensional electron gas physics. Graphene is generally considered to be a strong candidate to succeed silicon as an electronic material. However, to date, it actually has not yet demonstrated capabilities that exceed standard semiconducting materials. One disadvantage of conventionally fabricated graphene devices is that nanoscopically patterned graphene tends to have disordered edges that severely reduce mobilities thereby obviating its advantage over other materials. The other disadvantage is that pristine graphene does not contain a band gap, which is critical for standard field effect transistor to operate. This thesis will show that graphene grown on structured silicon carbide surfaces overcomes the edge roughness and promises to provide an inroad into nanoscale patterning of graphene. High-quality ribbons and rings can be made using this technique.

CHAPTER I

INTRODUCTION

1.1 Graphene: lattice structure and band structure

Graphene is a single layer of carbon with a honeycomb lattice. It is the building block for many sp^2 carbons: graphite, carbon nanotube, and fullerenes. The in-plane σ bonds between sp^2 carbons give graphene great mechanical strength and chemical stability. On the other hand, the out-of-plane π bonds carriers non-local electrons with unique band structure (energy-momentum relations or E-K relation) as a result of the symmetry of the lattice. The band structure of graphene was first calculated by Wallace [8] using nearest-neighbor tight bonding method and the band structure can be expressed as[8]

$$E(\mathbf{k}) = \pm t\sqrt{1 + 4\cos^2(\frac{k_y a}{2}) + 4\cos(\frac{k_y a}{2})\cos(\frac{\sqrt{3}k_x a}{2})} \tag{1}$$

where t is the tight-bending constant and the $\pm$ are for the conduction and valence band respectively. A more accurate band structure calculation requires advanced technique such as density-function theory. Nevertheless, Equation 1 is sufficient to provide an insight into the main feature of the band structure (Figure 2). According to Equation 1, the conduction and valence band meets at the corners of the hexagonal-shaped Brillouin zone of graphene (Dirac points), near which, the bands become linear and can be approximated as[8]

$$E(\mathbf{k}) \simeq \pm\hbar v_f|\mathbf{k} - \mathbf{K}| \tag{2}$$

where v_f is the Fermi velocity, about 1/300 of the speed of light[9] and $\mathbf{K}$ is the momentum at Dirac points. This conical band structure is exceptional compared with these hyperbolic -shaped bands in regular metal and semiconductors. Instead, it is similar to the energy-momentum relation for photons. Therefore, charge carriers in graphene are quasi-particles (electron and holes) travels at at 1/300 of the speed of light independent of the energy, just like photons.

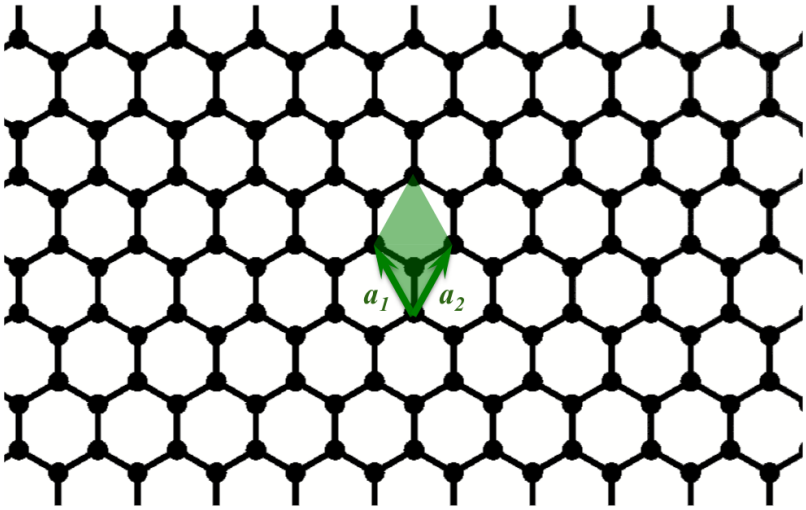

Figure 1: Graphene lattice structure. The unit cell and primitive lattice vectors are in green.

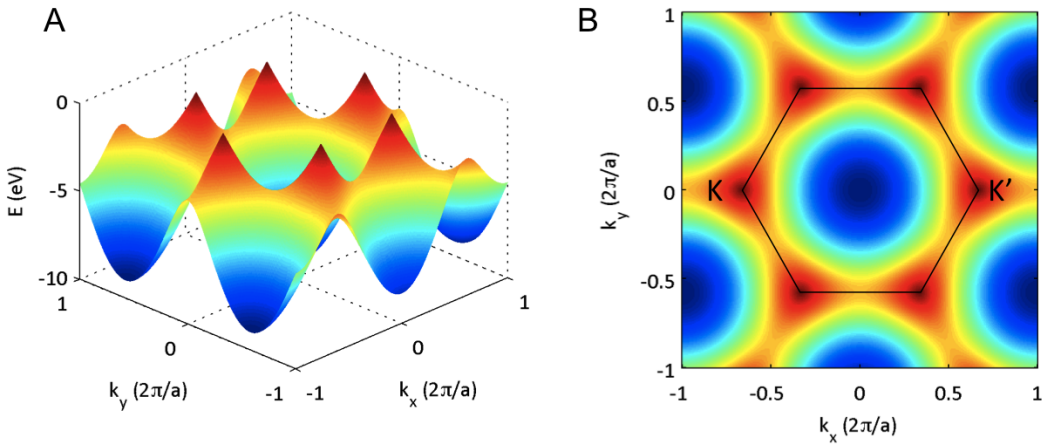

Figure 2: The band structure of graphene calculated using equation 2. (A) Three-dimensional view of the valence band. The conducting band is the mirror reflection of the valence band with respect to E=0 plane. (B) The same band structure as in (A) in plane view. The hexagon indicates the first Brillouin zone of graphene.

The unit cell of graphene contains two carbon atoms (A and B). Hence, the honeycomb lattice is consist of two set of identical hexagonal carbon lattice shifted by the distance of a carbon-carbon bond. These two lattices give rise to unique electron transport properties in graphene. The π band electron state is a combination of two orthogonal states (Φ_A) and (Φ_B), which belong to the A and B lattices respectively. This extra degree of freedom for electron to choose between A and B lattices are called pseudo-spin, for its mathematical similarity to the spin degree of free of electrons[10]. A general expression for the electron state in graphene can be written as[10]

$$\Phi = (\Phi_A, \Phi_B)\frac{1}{\sqrt{2}}\begin{pmatrix} e^{i\theta_A} \\ e^{i\theta_B} \end{pmatrix} \tag{3}$$

where Φ is a π band state $\Phi_A(\mathbf{r}) = \Phi_B(\mathbf{r}+\mathbf{r_{C-C}})$, and the spin-like term is the pseudo-spin. The states with pseudo-spin $\frac{1}{\sqrt{2}}\begin{pmatrix} 1 \\ -1 \end{pmatrix}$ and $\frac{1}{\sqrt{2}}\begin{pmatrix} 1 \\ 1 \end{pmatrix}$ are "anti-bonding" and "bonding" states, which are orthogonal to each other. As a result, electrons in bonding states can not be scattered to anti-bonding states and vice versa. As shown in Figure 3, the forward and backward moving electron states in a single Dirac cone contains different pseudo-spins, which forbids the intra-valley scattering (the scattering of electrons within a Dirac cone). Therefore, electron(hole) mobilities in two-dimensional graphene are expected to be high.

Although suppressed in graphene, electron scattering still exists in the form such as electron-phonon scattering[11] and electron-electron scattering [12], [13]. However, both scatterings are not significant in graphene at room temperature. The electron-phonon scattering is weak as a result of the high Debye temperature of graphene[11], which causes that, even at room temperature, very few phonons are available in graphene to scatter electrons. The electron-electron interaction is weak in moderately doped graphene ($\sim 10^{12} cm^{-2}$) [12]. Therefore it is not a major concern for electron transport in regular graphene devices.

1.2 Methods to produce graphene

While first theoretical paper on the unique band structure of graphene was published in 1947 [8], its significance was ignored for more than half a century. "Monolayer graphite" or "Few-layer graphite" reported in early literature was exfoliated from graphite or found

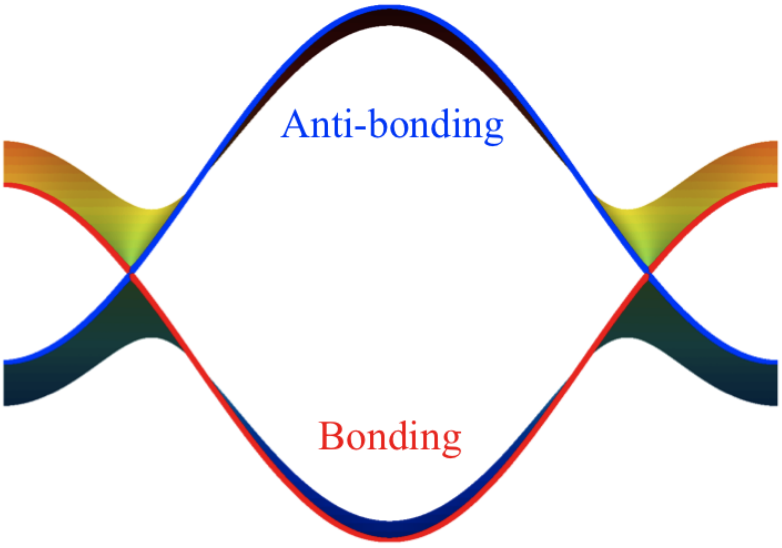

Figure 3: The graphene band structure along $k_y = 0$. The bonding states are in red and the anti-bonding states are in blue. Scattering between the bonding and the anti-bonding states is forbidden due to the conservation of the pseudo-spin.

to form on substrates such as Ni[14], Ir[15], Pt[16], and SiC[17]. In 2004, the Manchester group [1] and the Georgia Tech group ([18], [19]) reported the electron transport observation of graphene obtained from different method. These discoveries marked the onset of the "gold rush" on graphene. Currently, four major methods are used to produce graphene: mechanical exfoliation, chemical-vapor deposition (CVD), reduction from graphene oxide, and epitaxial growth on SiC.

The mechanical exfoliation method (the "Scotch tape" method) was introduced by Geim et al. in 2004[1]. In this method, graphene is peeled off from graphite using a Scotch tape, and then transferred onto a silicon wafer with 300nm silicon oxide. Mono-layer graphene can be identified under optical microscopy because of its unique color under white light (Figure 4(A)). Because of its simplicity, the "Scotch tape" method is widely used in research. After all, most experiments only need graphene domains to be larger than a few micrometers. The disadvantage of this method is its lack of scalability[20]. Therefore it can not be the route towards real application[20].

CVD is another method adopted by many graphene research groups ([2], [21], [22], [23], and [24]. Molecules containing carbon atoms (such as methane [2], [21], [22], and

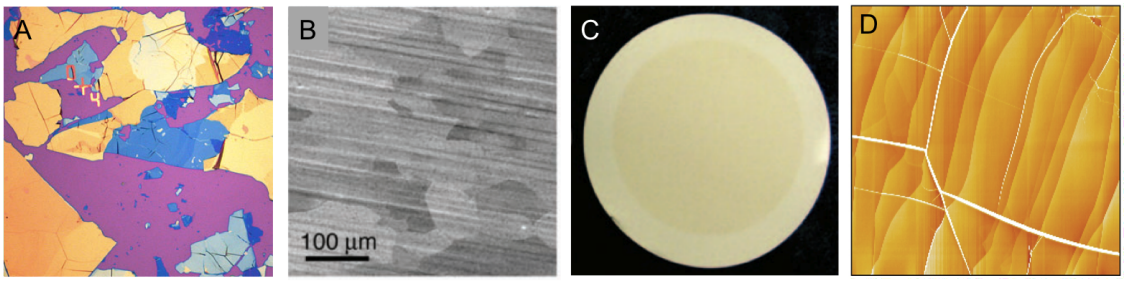

Figure 4: Methods for producing graphene. (A) Optical image of mechanically exfoliated graphene flakes [1]. (B) CVD graphene on copper [2]. (C) Reduced graphene oxide deposited on a substrate [3]. (D) Topography image of epitaxial graphene on SiC.

[23]) desiccate at high temperature and carbon atoms deposite on the substrate to form graphene[25] (Figure 4(B)). Many metals can be used for substrates, such as Cu[2], Ni[23], Ir [26][27] and Ru[28]. Graphene sheet over 30 inches in size has been produced using CVD on Cu [21]. Disadvantages of the CVD method includes the small domain size of graphene[29] and the necessity of transferring the graphene sheet from the metal to an insulating surface[22].

Reduction of oxidized graphene is another route to produce graphene[3]. In this method, graphite bulk is oxidized, hence oxidized graphite layers detach from the bulk to become graphene oxide flakes[30]. These flakes is then chemically reduced to become graphene flakes and can be deposited on to a substrate [3] (Figure 4(C)). This method allows mass production of graphene flakes[3]. Disadvatanges of this method includes the small flake size and the relative low quality of graphene compared with graphene produced with other methods[31] [32].

The graphene production method used in this thesis is the epitaxial growth on SiC. Van Bommel et al. first showed in 1975 that a graphene layer grows on hexagonal silicon carbide in ultrahigh vacuum (UHV) at temperatures above about 800 ^{o}C [33] . Silicon sublimation from the SiC causes a carbon rich surface that nucleates an epitaxial graphene layer. The graphene growth rate was found to depend on the specific polar SiC crystal face: graphene forms much slower on Si-face than on the C-face. Van Bommel et al. identified monocrystalline graphite monolayer films (i.e., graphene) [33] that were found to be essentially decoupled from the SiC substrate [17] and thus were electronically similar to

isolated graphene sheets [19]. This method has then being developed into the confinement-controlled sublimate growth technique at Georgia Tech[20] . Details of this technique will be discussed in Chapter III. Since the year 2004, epitaxial graphene has been an important platform for graphene research. Shubnikov-de Haas oscillations are observed on multilayer graphene [19], the half-integer quantum Hall effect are achieved in monolayer graphene[34]. The graphene mobility is more than 20,000 $cm^2V^{-1}s{-}1$ on doped monolayer graphene [34] and over 250,000 $cm^2V^{-1}s{-}1$ for nearly charge neutral layers with in the mutlilayer graphene [35]. The nearly-ideal graphene band structure is also observes [9]. Importantly, epitaxial graphene is a scalable platform that is compatible with current manufacturing platform[20] in the semiconductor industry. Therefore, epitaxial graphene on SiC is important for graphene application[20].

1.3 Electron transport theory

This section will introduce fundamental theories on electron transport. It starts with the semi-classical theory for diffusive transport, then move on to quantum mechanical theory on diffusive transport, and lastly the ballistic transport and the Landauer-Buttinger formalism.

1.3.1 Semi-classical theory of electron transport

A simple but powerful semi-classical theory for diffusive transport is the the Drude model [36]. Drude model treats electrons as particles with effect mass determined by the band structure [36]. The use of effective mass instead of real electron mass is the reason for the word "semi". In diffusive transport regime, electrons are scattered frequently during the transport. The average frequency of electron scattering is defined as [37]

$$1/\tau_m, \tag{4}$$

where τ_m is the momentum relation time, the average time between two scattering events of a electron. The mean free pass, the distance between two scattering events is defined as[37]

$$L_m = v_f \tau_m, \tag{5}$$

where v_f is the Fermi velocity. In an external field, electrons will drift, causing the macroscopical electron current. In the steady state, the loss of momentum of a electron by scatterings is fully compensated by the force of the external field. This steady state can be described as[37]

$$\left(\frac{d\mathbf{p}}{dt}\right)_{scattering} = \left(\frac{d\mathbf{p}}{dt}\right)_{field} \tag{6}$$

where

$$[37]\left(\frac{d\mathbf{p}}{dt}\right)_{scattering} = \frac{m\mathbf{v}_d}{\tau_m} \;\; \& \;\; \left(\frac{d\mathbf{p}}{dt}\right)_{field} = e(\mathbf{E} + \mathbf{v}_d \times \mathbf{B}), \tag{7}$$

when both electrical and magnetic field exist. For a two-dimensional conductor, the equation (6) and (7) can be combined and written as[37]

$$\begin{pmatrix} m/e\tau_m & -B \\ +B & m/e\tau_m \end{pmatrix} \begin{pmatrix} v_x \\ v_y \end{pmatrix} = \begin{pmatrix} E_x \\ E_y \end{pmatrix} \tag{8}$$

where v_x and v_y are the velocities of a electron along x and y directions while the magnetic field is assumed to be perpendicular to the x-y plain. By defining the current density $\mathbf{J} = en\mathbf{v}$, the conductivity$\sigma = J/E$, and the mobility $\mu = e\tau_m/m$, in which n is the 2D carrier density and e is the electron charge, equation (8) can be re-written as[37]

$$\begin{pmatrix} E_x \\ E_y \end{pmatrix} = \begin{pmatrix} \rho_{xx} & \rho_{xy} \\ \rho_{yx} & \rho_{yy} \end{pmatrix} \begin{pmatrix} J_x \\ J_y \end{pmatrix} \tag{9}$$

where $\rho_{xx} = \sigma^{-1}$ is the two dimensional resistivity or "square resistance" and ρ_{xy} is the Hall resistivity. By comparing Equation 8 and 9, the Hall resistivity can be expressed as

$$\rho_{yx} = -\rho_{xy} = \mu B/\sigma = B/en \tag{10}$$

Equation (10) is frequently used to estimate the carrier density in a two dimensional film[37].

1.3.2 Quantum mechanical transport theory

At low temperatures, the electron transport can no longer be described by the semi-classical theory[37] and the wave feature of electrons has to be taken into the consideration. Electron waves start exhibit interference effects even in the diffusive transport regime[37]. The relevant time scale for quantum interference is the phase-coherent time τ_ϕ. τ_ϕ is the average

time between two scattering that can randomize the phase of the electron wave[37]. The phase coherent length is defined as $L_\phi = v_f \tau_\phi$ accordingly, which is the average distance that an electron can travel without losing its phase memory. Phase memory of a electron can only be destroyed by inelastic scattering, so the phase coherent length can be longer than the mean free path. Major inelastic scattering sources include electron-phonon scattering, electron-electron scattering, and electron scattering involving internal degree of freedom of a electron like spin[37]. The last two scattering processes are rare for graphene at normal carrier densities [12][38]. Electron-phonon scattering is also weak in graphene and will become even less significant at low temperature[11]. Therefore, graphene can have long phase coherent length exceeding the dimension of the device (i.e. many micronmeters) at low temperatures so that devices are fully coherent and transport has to be described quantum mechanically.

One important quantum mechanic effect at low temperature is the Landau quantization of the electron states: cyclotron orbits of electrons will quantize with the presence of a magnetic field[39]. In a metallic conductor, the Landau quantization is theoretically described by including the magnetic potential in the Laudau gauge into the Hamiltonian. The eigenenergy of the Hamiltonian is[39]

$$E_n = \hbar\omega_c \left(n + \frac{1}{2}\right), \quad \omega_c = \frac{eB}{m^* v_f} \tag{11}$$

where ω_c is the cyclotron frequency of electron is a magnetic field, m^* is the electron effective mass, v_f is the Fermi velocity of the electron, and n is the Landau level index. For graphene, a similar development gives a modified spectrum[40]

$$E_n = sgn(n)\sqrt{2\hbar e B v_f^2 |n|}. \tag{12}$$

The relation between Landau level energies and B and n are no longer linear in graphene. More importantly, a Laudau level appears at zero energy, which implies that electrons in graphene acquired a Barrier's phase of π[41][42][18][19]. As the linear band only exist in mono-layer graphene, the Barrie's phase can be used in transport to distinguish mono-layer graphene from bilayer or multi-layer graphene[41][42][18][19].

The Landau quantization manifest in transport in the Shubnikov-de Haas oscillation (SdH)[19] and the quantum Hall effect (QHE)[41][42][34]. The former is the oscillation of the magnetoresistance and the later is the appearance of plateaus on the Hall resistance[37]. During a magnetic field sweep, the Landau level peak positions moves following the relation in Equation 11 while the Fermi level stays unchanged. This relative shift of the Fermi energy with respect to the Landau level creates the registered oscillations[37]. Every time the Fermi level aligns with a Landau level, the resistance attributes to a maximum[37]. On the other hand, the Hall resistance is the voltage difference between the two edges of a film divided by the current. In a magnetic field, the electron states are spatially quantized along the film[37], causing electron states with opposite propagation directions to spatially separate. The forward current is along one edge and the backward current is along the other. Back scattering of electron states from one edge to the other edges become almost impossible and edge states become ballistic channels for transport[37]. When the Fermi level is between two Landau energies, all Landau levels below the Fermi energy are fully occupied. The voltage is constant along the same side because of the absence of scattering and the voltage difference between two edges equals to the voltage between the two contacts that provides the current. The converted Hall resistance is thus equals to the resistance of a perfect ballistic conductor (See the next section for ballistic transport) and the resistance drop is limited at the contacts. The number of conducting channels equals to the number of Landau levels below the Fermi energy. When the Fermi-level moves between two Landau level, the Hall resistance will remains, giving rise to plateaus to the Hall resistance in a magnetic field sweep.

1.3.3 Ballistic transport

Transport on length scales that are smaller than the mean free path is ballistic. In a ballistic wire, transport of electrons is similar to the propagation of light in a waveguide[37]. Electrons move at the Fermi velocity and the conductance is quantized[37]. The resistance of a perfect ballistic channel is not zero but has a well defined value. The following development follows the reference [37] and will provide a simple picture of the ballistic conductance. The

simplest ballistic conductor is the one dimensional conductor with a parabolic conduction band(Figure 5(B)). The conductor is connect to two contacts, which are electron reservoirs that contains electron states with a thermal distribution of energies and momentums[37]. In addition, both contacts are assumed to be "reflectionless", which means electrons come into the contact have zero chance to be scattered back to the conductor. Therefore, all left-moving electrons (k^-) are from the contact on the right and all right-moving electrons (k^+) are from the contact on the left (Figure 5(B)). An external voltage creates a difference between the chemical potential of two contacts:

$$\mu^- - \mu^+ = eV. \tag{13}$$

This gives rise to a difference between the number of left-moving and right-moving electrons, and generates a net current, which can be calculated as

$$I = I^- - I^+ = \frac{e}{L}\sum_k vf^- - \frac{e}{L}\sum_k vf^+, \tag{14}$$

where L is the length of the conductor and f^+ and f^- are the Fermi-Dirac distributions describing the electron density of state at finite temperature for the left and the right contacts. By applying the relation

$$v = \frac{1}{\hbar}\frac{\partial E}{\partial k} \quad and \quad \sum k \to 2 \times \frac{L}{2\pi}\int dk, \tag{15}$$

equation (14) converts to

$$I = \frac{2e}{h}\int_0^\infty (f^-(E) - f^+(E))dE = \frac{2e}{h}(\mu^- - \mu^+), \tag{16}$$

Note that the detailed shape of the Fermi-Dirac function $f^-(E)$ and $f^+(E)$ cancels out and thus the final result is temperature independent. Equation 13 and Equation 16 together provide an expression of the conductance of a perfect ballistic channel[37]

$$G = \frac{1}{R} = \frac{I}{V} = \frac{2e^2}{h}. \tag{17}$$

For a conductor with multiple ballistic perfect channels, the total conductance is[37]

$$G_M = \frac{2e^2}{h}M. \tag{18}$$

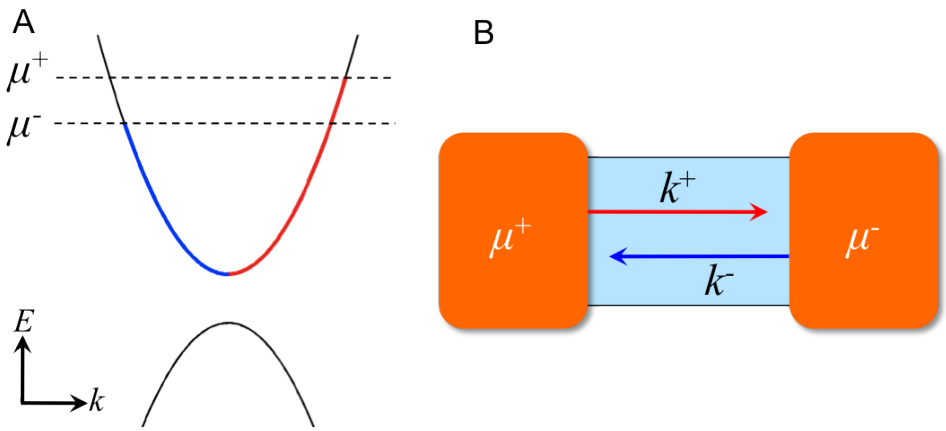

Figure 5: An illustration of ballistic transport. (A) The one-dimensional band structure of semiconductor. (B) A two-terminal conductance measurement configuration. For a ballistic channel connect to two "reflectionless" contacts.

The number of channels in a conductor is proportional to its width as a result of the lateral quantum confinement and corresponds to the number of transverse modes in the conductor up to the Fermi level.

An imperfect channel must have conductance smaller than the perfect channel conductance (Equation 18) and can be expressed in a form similar to a waveguide[37]:

$$G = \frac{2e^2}{h} \sum_{n=1}^{M} T_n. \tag{19}$$

Equation 19 is the Landauer equation. A perfect ballistic conductor has transmission coefficient $T = 1$ and imperfect conductors have $0 < T < 1$. For a more complete discussion, see the reference [37]. The Landauer equation provides an alternative picture of electron transport. Following Landauer, transport in any conductor can be formulated into a channel picture, in which each channel is appropriately weighted with transverse coefficient T.

1.4 Graphene band gap engineering

Graphene has not demonstrated its capability to replace Si as an alternative material for digital electronics. The major reason is that graphene has no energy gap[8][9]. Having the conduction and the valence band meet at a single point in the Brillouin zone, pristine graphene is a semi-metal instead of semiconductor[8]. The consequence of the lack of a band gap is that the current in a graphene channel can never be turned off using a electrostatic

gate[41][43]. This is not a problem for analog devices such as RF transistors[44], but for digital applications, the absence of the "off" state is equivalent to the absence of "0" in a binary switch, which is the foundational of a digital circuit [45]. Therefore, introducing a band gap into graphene is critical for digital electronic applications. Two majors methods were proposed to solve this problem. One method is to use quantum confinement effect in narrow ribbons [46] [47] [48]. The other method is chemically modify graphene [49] [50].

Quantum confinement can be observed in graphene with ribbon width smaller than 100nm[46][47][48]. Confinement cause the transverse momentum of electron states to quantized and the two-dimensional graphene band structure to break into one-dimensional sub-bands[46], very much like electromagnetic wave in a waveguide[51]. The energy separation between the sub-bands is inversely proportional to the ribbon width as $\Delta E \sim 1eV/w$[46], in which w is the width of the ribbon in nanometers. For specific ribbons, this can cause a gap at the Fermi level analogous to the energy gap in semiconducting carbon nanotubes[46]. Early research [47] [6] [48] suggested band gaps in lithographically patterned graphene nanoribbons. However, it was later concluded that the gaps observed in transport measurement are transport gaps instead of band gaps[52]. The lithography processes create rough edges that cause electron scatters. At low charge densities, electron become locally trapped and transport becomes activated, in which electrons have to hop from one puddle to the next. This process is called strong localization[52][6]. Consequently, the mobility of these lithographically patterned nanoribbon approaches zero as the ribbon width decreases [53]. One method to overcome solves the edge roughness problem is by unzipping carbon nanotubes [54] [55]. This method significantly increase the mobility of nanoribbons, but it shares the same scalability issue as carbon nanotubes[54] [55].

As predicted by theoretical calculation, chemical modification of graphene can introduce large band gaps [49][50]. Experimental research has been done on modified graphene such as hyogenated graphene ("graphane" [49] [56]), oxidized graphene (graphene oxide [57]), florinated graphene[58], and aryl group funtionalized graphene [59]. Some of these research suggest that chemically modified graphene causes a band gap. However, more work is required.

1.5 Thesis outline

The motivation of this thesis is to explore the potential of epitaxial graphene as a electronic material. Chapter II will introduce the experimental methods used in this research, including material characterization, device fabrication, and electronic transport measurement. Chapter III will discuss on the technique for epitaxial graphene growth and the method for templated graphene growth. Chapter IV will focus on graphene nanoribbons selectively grown on off-axis facets of SiC and show that these ribbons are ballistic conductors.

CHAPTER II

EXPERIMENT METHODS

2.1 Surface characterization

2.1.1 Atomic force microscopy

One type of scanning probe microscopy (SPM) widely used for surface topography characterization is the atomic force microscopy (AFM)[60]. The key component of an AFM is a cantilever provided with a sharp tip. The tip responds to the surface Van der Waals (VDW) forces, so it can follow surface topography changes to generate images. A standard AFM operates in two modes. One mode is the contact mode[60]. In this mode, the AFM tip is pressed at the surface with a fixed force, which is typically a few nN. As the tip follows the surface topography during a scan, the cantilever will be deformed to adjust the tip position. The magnitude of this deformation is detected through measuring the deflection of a laser beam that aligned at the back of the cantilever. The deflected beam angle is recorded by a photodetector and thus converted to the surface height variation. The other AFM mode is the non-contact mode, or the "tapping mode"[60]. In this mode, the cantilever is lifted by a small distance and driven to oscillate slightly above its resonance frequency. As the VDW force reduces, the resonance frequency, and thus the oscillation magnitude decreases. Therefore, the oscillation magnitude, which is monitored by the laser beam, is used in a feed-back loop that maintains a constant tip-sample distance. The trace of the cantilever is thus recorded to construct the topography image.

These two AFM modes are not equivalent and both have some advantages and disadvantages. The contact mode is more straightforward in design and data interpretation[60]. However, the tip might scratch the surface and move surface objects around during a scan[61]. In contrast, the non-conatct mode is non-invasive, which avoids direct contacts with the surface. However, the non-contact mode is harder to operate on soft surfaces or in liquid[62][63]. Both methods are applied in more advanced SPMs such as conductive AFM

and electrostatic force microscopy. AFM is popular in nano science research because of its high resolutions and the easiness to use comparing to the scanning tunneling microscopy[60]. The vertical resolution of the AFM is about 0.1 $\mathring{A}$ in the equipment used in this thesis research, primarily limited by the noise level in a measurement system. This resolution allows the AFM to resolve a single layer of atoms. The lateral resolution of the AFM is limited by the dimensions of the tip[60]. The radius of a typical AFM tip(type PPP-NCHR by NANOSENSORS^{TM}) is about 10nm.

2.1.2 Electrostatic force microscopy

Another SPM that is frequently used in this thesis is the electrostatic force microscopy (EFM)[64]. The EFM is developed based on non-contact AFM and senses the electrostatic force between the tip and the surface. The major issue in building an EFM is to differentiate the electrostatic force from the VDW force. Two solutions are commonly used. The first solution is the one used in the standard EFM mode, or "lift-mode". In the lift-mode, the electrostatic force is measured at a tip-sample distance larger than that in the normal AFM. Since the VDW force ($\propto 1/r^6$) decays much faster than the electrostatic force ($\propto 1/r^2$) away from surface, the force the tip senses at a large distance is dominated by the electrostatic force. In operation, the tip will first take a AFM scan, then traces back the AFM profile at a lifted position to take a EFM scan. This double-scan excludes the effect due to the variable tip-sample distance. However, the double-scan procedure also doubles the time to take a image. The other method to differentiate these two forces is used in enhanced EFM. In the enhanced EFM mode, the electrostatic force is distinguished by a different frequency by applying an small AC bias voltage to the tip. The measured electrostatic force corresponds to this frequency, thus can be detected using a lock-in amplifier (details about lock-in amplifier will be discuss later in this chapter). This dual-frequency technique allows simultaneous imaging of topography and electrostatic force. Therefore it is most frequently used EFM mode in this thesis

EFM is a powerful tool to distinguish graphene from the substrate even when the surface topography cannot do so. A clean graphene surface has different surface potential compared

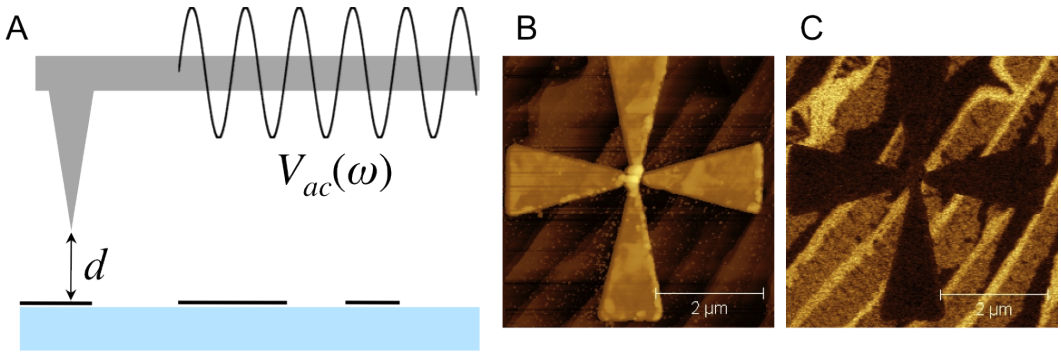

Figure 6: The operation principle of EFM is illustrated in (A). As an example, the AFM and EFM of a sample with gold mark on Si face SiC with 0, 1, and 2 layers of graphene is shown in (B)

with it is in the substrate. As the surface potential difference between the tip and the sample directly relates to the electrostatic force, EFM images can locate the surface region covered with graphene. The relation between the surface potential difference and the electrostatic force can be understood using a parallel plate capacitor model. In the enhanced EFM mode, the electrostatic force at the frequency corresponds to the tip bias is[65]

$$F(t) \propto \frac{C}{d} \times (V_{dc} - V_s) \times V_{ac} sin(\omega t), \tag{20}$$

in which C and d are the capacitance and distance between the tip and the sample surface respectively, V_{dc} and V_{ac} are DC and AC voltage applied between a tip and a sample respectively, and V_s is the surface potential difference between the tip and the sample surface. During a EFM imaging, all parameters in Equation 20 are fixed except the surface potential V_s. Therefore, the EFM image maps the surface potential of the sample surface. Since graphene on with different number of layers might have different surface potentials, EFM can be used to manifest the thickness of graphene[66]. An illustration of the enhanced EFM is shown in Figure 6(A) and Figure 6(B) and (C) are comparison between a AFM and a EFM image taken at the same surface area. While the AFM image only shows the topography change from the substrate to the cross mark, the EFM image provides much more information on the surface.

2.1.3 Conductive AFM

One advanced application of contact AFM is the conductive AFM (C-AFM). During a C-AFM scan, voltage is applied between a conducting tip and the sample to generate a current, which is recorded at each image location to construct a C-AFM image. The current in each image pixel reflects the conductance between the tip and the place where the current is drained on the sample, but not the local surface conductivity. As a result, C-AFM image might show zero current at a conducting domain, which is separated from the current drain by an insulating area.

The C-AFM can also be used for current-voltage (I-V) spectroscopy[67]. Instead of using a fixed bias voltage, the I-V spectroscopy records the current-voltage response (I-V) at each scanning location. The I-V spectra provide a deeper insight into the surface conductance: the shape of the I-Vs distinguishes between metallic and semiconducting films and the slope of the linear I-Vs provides an accurate estimation of the conductance. A disadvantage of the I-V spectroscopy is its long imaging time since the tip has to stay at each surface location for much longer time compared to regular C-AFM. The long time imaging is susceptible to drift of the sample, which causes it difficult to capture the targeted surface area.

2.1.4 Raman spectroscopy

Similar to the electron band structure, the vibration modes of a crystal(phonons) also have energy-momentum (E-K) dispersion relations (phonon modes)[36]. The phonon modes can be detected using Raman spectroscopy[68], which measures the energy shift of single energy photons due to phonon scatterings[68]. Most phonon modes dost not interact with photons unless certain selection rules are satisfied[68]. Therefore, a change in the Raman spectrum of a crystal usually suggests a change of the crystal structure that cause the change of the phonon-mode or the selection rule[68].

Graphene has its major peaks located at 1350 cm^{-1} (D peak), 1590cm^{-1} (G peak), and 2700cm^{-1} (2D peak)[69] with 532nm laser. The G peak is the direct scattering of photon by the zone-center E_{2g} phonon[70]. Meanwhile, the 2D peak involves four scattering steps[69]: (i) A incident photon excites a electron-hole pair in a Dirac cone near K; (ii) a A_{1g} phonon

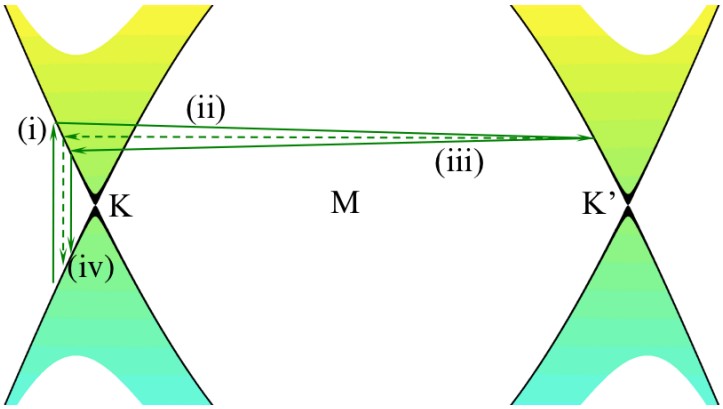

Figure 7: The four-step process for generating the D and 2D peak. (i) electon-hole pair excitation, (ii) electron scattering by large momentum phonon, (iii) electron scattering by phonon(solid line) or by elastic scatter (dashed line), and (iv) electron-hole pari recombination.

with momentum $\mathbf{q} = \mathbf{k}$ scatters the hot electron to another Dirac cone at K'; (iii) a second A_{1g} phonon with $\mathbf{q} = -\mathbf{k}$ scatters the hot electron back to the K point Dirac cone; and (iv) the electron-hole pair recombines to emit a photon. The amount of energy shift of the phonon equals the total energy of the two A_{1g} phonons. The scattering process for the D-peak is similar as the 2D peak except that in step (iii), the hot electron is scattered by an elastic scatter such as graphene lattice defects or boundaries. Therefore, the energy shift of the D peak equals the energy of a single A_{1g} phonon. This scattering process is illustrated in Figure 7. A Raman spectrum can be converted into a few quantities that can characterizes the graphene. The following are frequently used ones.

• **Intensity ratio of the D and G peak.** Intensity in the D peak requires lattices defects or graphene boundaries while the G peak is not effected as long as the sp^2 C-C bond is still intact. Therefore, the ratio of the peak intensity (I(D)/I(G)) is a good indicator of the quality of a graphene sheet. Graphene with very few lattice defect should have I(D)/I(G) close to zero except at the edge of the graphene sheet[70].

• **Shape of the 2D peak.** The shape of the 2D peak is an important indicator of the number of layers of graphene. A Raman peak typically has a single Lorentizan shape, arising from the finite lifetime of phonons[70]. Each Lorentizan-shaped peak corresponds to a Raman scattering process.While the 2D of a monolayer graphene can be fitted by a

single Lorentizan, the 2D peak of bilayer or multilayer graphene with AB stacking are a combination of multiple Lorentizan-shapes peaks[71]. For example, as the bilayer graphene has two conduction bands(π_1 and π_2) at K/K' points, the step (i) and (ii) in the four-step scattering process for 2D peak can both have two options, thus in total, the 2D peak of bilayer graphene contains four Lorentizan-shaped peaks([69][71]). Therefore, the single Lorentizan-shaped 2D peak is an important indictor of a monolayer graphene or multilayer epitaxial graphene on C-face SiC, in which graphene layer are electronically detached from each other to maintain a monolayer-like band structure[72].

• **Position of the G and 2D peak** The combined shifts of the G and 2D peak are a good indicators of Fermi level of graphene[73]. Both electron and hole doping of graphene cause the stiffening of the E_{2g} phonon and shift the G peak to higher energy[73]. Meanwhile, the electron and hole doping shifts the 2D peak to the opposite direction[73]. Hence the position of the G and 2D peak together provide information on the doping of graphene.

2.2 Device fabrication

2.2.1 Electron-beam lithography

Electron-beam (e-beam) lithography is a technique to fabricate devices with small dimensions. The focused electron beam can write features as small as $10nm$[74]. A typical lithography process involves the following steps: coating the sample surface with e-beam resist, exposing the selected areas with e-beam, developing resist in a developer that selectively dissolves exposed or unexposed resist areas, and transfering the resist pattern onto the sample with plasma etching or thin film deposition[74]. Choices have to be made in each step based on the requirement of the lithography step. Below are a few tips on making these decisions. An illustration of the entire lithography process is shown in Figure (8) and an example of multi-step device fabrication is shown in Figure 9.

• **Resist** Resist is central to any e-beam lithography recipe. All subsequent lithography steps must conform to the nature of the resist. A resist is positive-tone, if the e-beam exposed area will be dissolved, or negative-tone, if the e-beam exposed area will remains after development. In this thesis, the most frequently used positive and negative-tone resist are

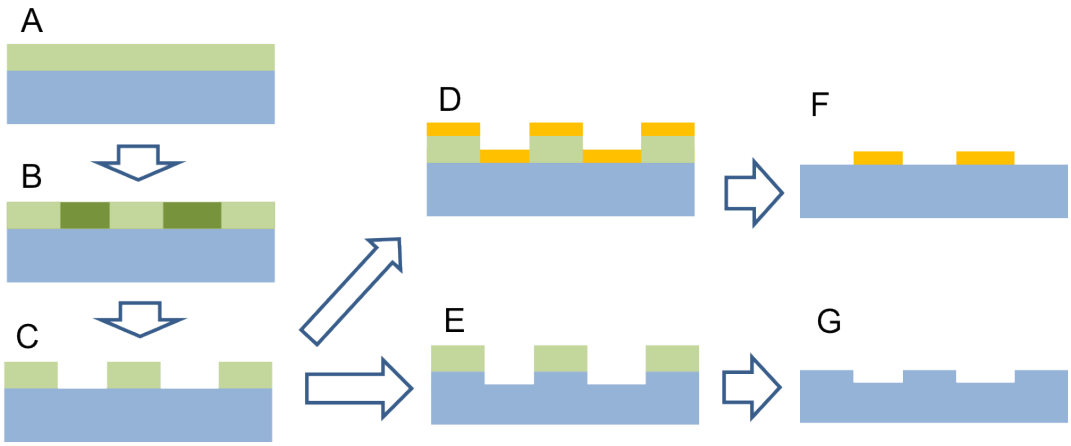

Figure 8: An illustration of the lithography process. E-beam resist is spin coated on the substrate(A), then selected area is exposed to the e-beam (B) and then the resist pattern is developed (C). After that, the sample can go through depostion (D) and (E) or etching (F) and (G). The distance between two alignment marks (the top-right and bottom-right crosses) is $40\mu m$.

polymethyl methacrylate (PMMA)[75] and hydrogen silsesquioxane (HSQ)[76] respectively. As-coated PMMA molecules are cross-linked into long polymer chains[75]. The high-energy electron beam breaks links between molecules, thereby significantly increasing the solubility of the polymer in the developer[75]. In contrast, as-coated HSQ is soluble in the developer and only the e-beam exposed are remain after development. The selection of resists depends on the purpose the lithography. PMMA can be easily removed in acetone, so it is good for the lift-off of thin films(see the following section) and plasma etching. Removal of e-beam exposed HSQ requires the use of strong chemical such as hydrofluoric acid (HF)[77], but it is excellent in patterning lines with less than 10nm in width[78].

Below are the lithography process used in this thesis. For general discussion of e-beam lithography, see [74].

- **Spin coating** Spin coating is a step to uniformly coat resist on a sample surface. Before the spin, a few drops of solvent carries the resist polymer are put on the sample. During the spin, the centrifuge force spreads the resist, uniformly coat the surface[74]. The thickness of the coating layer can be adjust by using solvents with different concentrations or fine tuned by using different spin speeds[79]. After spin, the sample is baked on a hot plate to evaporate residual solvents and promotes cross-linking for the case of PMMA[].

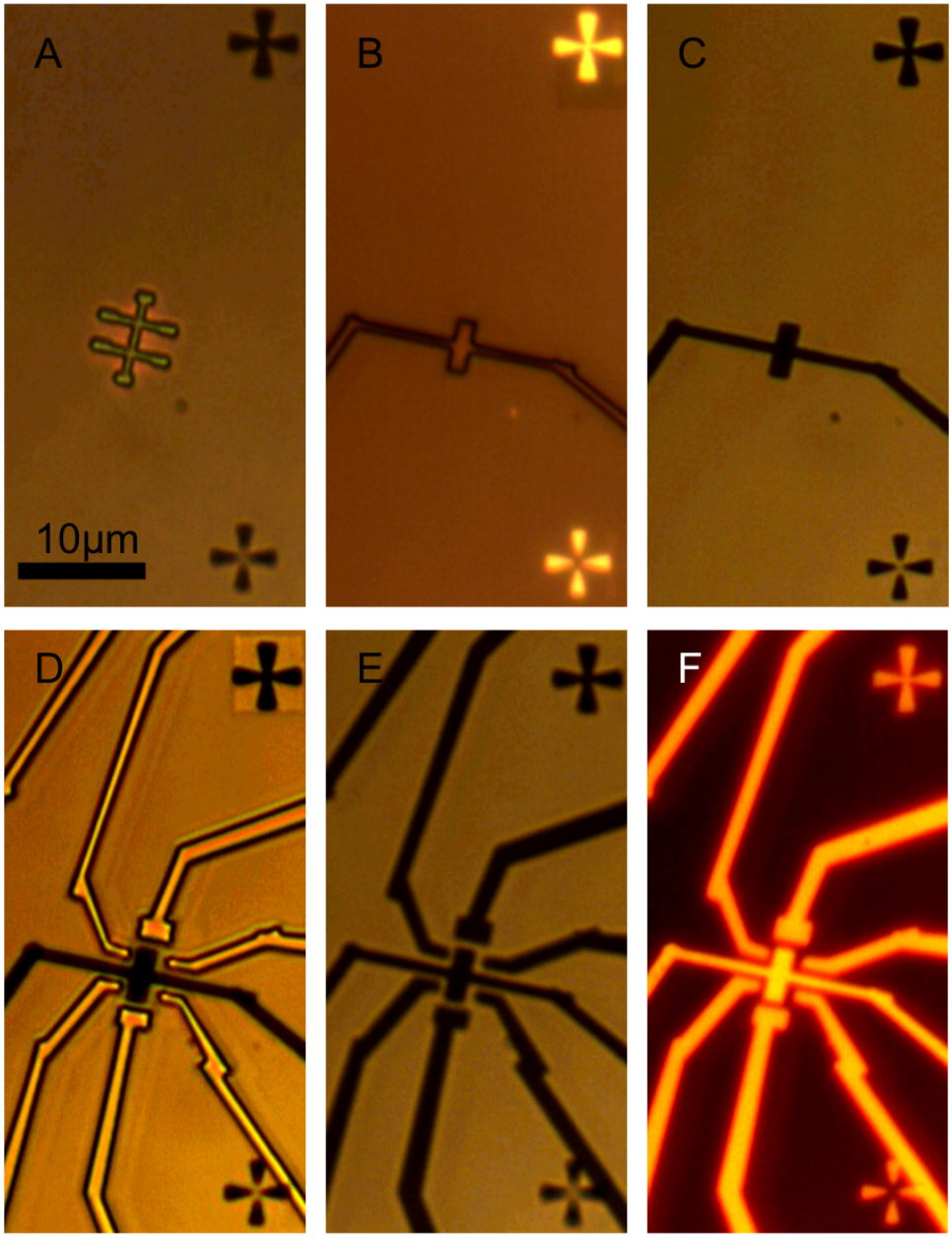

Figure 9: An series of optical images taken after each lithography step. This sample is a single layer Si-face graphene on SiC (see the next chapter for details. (A) Back-light optical image of a resist pattern. This sample is then etched in O_2 plasma to transfer this pattern into graphene. (B) Top-light optical image after the second e-beam lithography. The removed resist is for gate pattering. (C) Back-light image after dielectric and metal lift-off. (D) Back-light image of the third lithography for metal leads pattering. (E) and (F) are back and top-light images of the device after the lift-off of metal contacts.

The baking temperature and time are optimized for this purpose.

• **E-beam exposure** The e-beam exposure processes in this thesis are operated with two system. One is the JEOL JSM-5910 system, with e-beam energy at 30kV and a resolution of 100nm. The other system is the JEOL JBX-9300FS EBL System, with e-bean energy at 100kV and a resolution about 10nm. Both systems are computerized. During the exposure, the user-import pattern is converted into a matrix of exposure pixels. The focused e-beam stays at each pixel to apply the electron dose. Dose tests are frequently conducted in order to find the best dosage for certain patterns and resist.

The required "nominal dosage" depends on the dimension of features. The nominal dosage determines the density of electrons impinging on the sample surface but not the total number of electrons that will eventually interact with the resist, or the real dosage. The difference between the nominal and real dosage arises from the secondary electrons that are back-scattered by the substrate. Since the back-scattering electrons covers a large range of the surface area, large exposure features are more susceptible to the secondary electron[74]. This effect can be simulated using the software "Sceleton", which uses a molecular dynamic model to calculate the diffraction of electrons in a substrate. The simulated result can be incorporated into the pattern generation process so that the additional exposure by the secondary electrons are compensated. For 100eV electron beams on SiC substrate, the nominal dosage for a $(1\mu m)^2$ feature is about 50% higher than the it is for a $(100\mu m)^2$ feature.

• **Pattern develop.** The last step in a e-beam lithography is developing the pattern. In this step, the e-beam exposed resist is submerged in a developer to selectively dissolve either exposed or unexposed areas. The developing process includes three major parameters: developer concentration, developing time, and developing temperature. Room temperature is usually good enough for most developers. For the concentration, I used a mixture of methyl isobutyl ketone (MIBK) and isopropyl alcohol (IPA) with volume ratio 1:2 or 1:3 for PMMA development and 2.3% or 25% tetramethylammonium hydroxide (TMAH) in water for HSQ development. The developing time is a trade-off between a sharp feature and a clean removal of unwanted resist, and is affected by the dosage. A long developing time can

compensate a slight under-dose during the exposure.

• **Alignment** The fabrication of devices usually requires multiple sequential lithography steps. For these cases, alignment marks are necessary to keep the overlapping patterns mutually aligned. I usually use a matrix of gold crosses for this purpose because of the sharp contrast between gold and the SiC substrate during e-beam imaging. I also found that with height difference larger than 100nm, SiC features on SiC substrate can used for alignment purpose. The SiC alignment mark technique ensures an impurity-free SiC surfaces after lithography, which is important for the subsequent graphene growth, and saves the step for patterning alignment marks after the graphene growth.

2.2.2 Plasma etching.

Plasma etching is a powerful dry etching tool for graphene and SiC. The plasma ionizes the reactants and reduces the barrier for chemical reaction[74]. Both reactants (except the material to be etched) and products are in gas form so the etching can stay at a constant rate[74]. The plasma etching is usually conducted in a reactive ion etching system (RIE), in which plasma is generated by AC electric field near the sample surface. The free ions in the plasma is accelerated by the field to strike on to the sample surface. This process involves both sputtering and chemical reaction, so the etching is anisotropic: the etching rate is much higher in the vertical direction than the lateral. Therefore, with an etching mask, only the exposed surface area will be etched and the lithographically defined pattern can be transferred into the sample surface.

Graphene is usually etched by O_2 plasma with a patterned PMMA mask. SiC etching requires additional reactant that reacts with Si atoms. Gases such as SF_6[80] and CF_4[81] can fulfill this requirement. PMMA is still sufficient for shallow SiC etching with etching depth less than 20nm. But for deeper etching, a mask with high etching selectivity is necessary. I use Ni film as the etching mask because of its double digit selectivity in the SiC etching process [80].

2.2.3 Thin-film deposition

A process that is opposite to etching is deposition: materials are added to the surface instead of being removed[74]. In this thesis, most of the deposition processes are conducted using a e-beam evaporator, in which an focused electron beam locally heats a material source with an focused electron beam to enable a controlled evaporation in a high vacuum chamber. The atoms from vaporized source move in a straight line to the sample surface. The deposition rate is controlled by the power of the beam and can be monitored by a sensing crystal. A feed-back controller maintains the evaporation at a set rate. After deposition, unwanted film area is lifted-off by dissolving the underlying resist in a solvent (acetone for PMMA), thus the lithography pattern is transferred to the thin film.

Although the deposition chamber is in high vacuum, certain amount of water molecules are still present. For most metals, the oxidation rate due to the water in chamber is negligible compared to the deposition rate. However, readily-oxidized metals such as aluminum can have a oxidization rate comparable to the deposition rate. In the evaporation process used in this thesis, the deposited aluminum film will stay as aluminum when the deposition rate is $1\mathring{A}/s$ or higher, but will become aluminum oxide when the aluminum deposition rate is lower than 0.3 $\mathring{A}/s$. Therefore, by controlling the deposition rate, one can choose between aluminum and aluminum oxide. This controlled oxidation is very useful in coating graphene with aluminum oxide layer since this process can not be done in conventional methods like atomic layer deposition(ALD) due to the hydrophobic nature of graphene [82].

2.3 Low temperature transport measurement

2.3.1 Cryogenic system

Electron transport measurements require a cryogenic system andh height magnetic fields. The cryogenic system used in this thesis is cooled by liquid He (LHe), which can cool the sample down to $4.3K$. A LHe tank surrounds the sample chamber and maintains a LHe flow between into sample chamber. The LHe is surround by a liquid nitrogen (LN2) tank, being separated by a vacuum layer. The LN2 tank shields the heat from the environment to save LHe. The LN2 tank is also surrounded by a vacuum layer to reduced the heat

transfer between the LN2 and the environment. A heater and a thermometer is installed on the sample hold inside the cryogenic for transport measurement at different temperature. This cryogenic system is also equipped with a superconducting magnetic that can generate a magnetic field up to $9T$. The high magnetic field is generated by a superconducting coil, which has to be submerge in LHe to stay superconducting. The amplitude of the magnetic field is controlled by the current passing through the coil provided by a power supply and controlled by a LabView^{TM} program on PC. As the superconducting coil can maintain a constant current, the power supply only provides current during a sweep of magnetic field. A simpler low temperature system is also used in my experiments. This simple system consists of a vacuum chamber with a dipstick to hold a sample. The chamber is submerged in LN2 for cooling and the sample temperature is controlled and monitored by a heater and a thermometer installed on the sample holder.

2.3.2 Lock-in amplifier

The lock-in amplifier (lock-in, model Stanford Research System SR830) is a very convenient equipment to measure weak signals in an noisy environment[83]. A lock-in operates as both the voltage/current source and the measuring device for electronic measurements. As a source, a lock-in provides a low frequency AC signal for the measurement circuit. As a meter, the lock-in detects only the signal having the same frequency as the source. As the noise from the environment usually has a uniform distribution of power among all frequencies, the noise in the small window that can pass through the filter is much weaker than the total noise. As a result, the response can be accurately measured even in a noisy environment.

In an AC measurement, the measured signal contains two quantities: the amplitude and phase. In the lock-in, these two quantities are measured by mixing the input signal with two reference signals. One reference signal is phase with the source signal and the other is phase shifted by 90^o. The mixing of the input and a reference signal can be expressed as

$$\widetilde{V}_{meas} = V_{meas} cos(\omega t + \phi) \tag{21}$$

$$\widetilde{V}_{ref} = V_{ref} cos(\omega t) \tag{22}$$

$$\widetilde{V}_{meas}\widetilde{V}_{ref} = \frac{1}{2}V_{meas}V_{ref}cos(2\omega t + \phi) + \frac{1}{2}V_{meas}V_{ref}cos(\phi) \tag{23}$$

The DC term after the mixing contains both the amplitude and the phase. This signal is filtered out by a low pass filter with a small bandwidth. The other mixed signal will contain a DC term $\frac{1}{2}V_{meas}V_{ref}cos(\phi)$. By combining these two DC terms, the amplitude and the phase of the input signal can be calculated. A pure resistor has a phase that equals zero. However, as a real measurement circuit always contains some capacitor and inductor terms that produce phase shifts, the tolerance margin of the phase for a resistor is about 5^o.

A typical circuit for four-point resistance measurement is shown in Figure 10(A). The voltage source of the lock-in is in series with a resistor that is at least two orders of magnitude higher than the device so that it can serve as a constant current source. Typical values for the AC voltage amplitude, AC frequency, and the serial resistor is $1V$, $10M\Omega$, and $13Hz$ respectively. Meanwhile, the voltage meter in the lock-in picks up the voltage response in the device.

2.3.3 DC measurement

For current-voltage response (I-V) measurements, a DC source and a DC meter are used. The DC voltage source is generated using a Keithley 2400 and connected in series with the device. The current is measured by the same device and the voltage on the sample is measured by the voltage meter Agilent 34410. By sweeping the source voltage, the I-V curve of a device can be recorded.

The response of the differential conductance to bias voltage (dI/dV-V) can be obtained by taking derivative of the I-V curve. Since the numerical derivative amplifies the measurement noise, the dI/dV-V curve is usually calculated from the average of multiple I-V scans, which is time consuming. A more efficient and accurate method that directly measures dI/dV-V is illustrated in Figure 10(B). The DC current source bias the sample at a DC voltage, which is measured by the DC voltage meter. Meanwhile, the AC current source adds a differential current on top of the DC current and the AC voltage response is measured by the AC voltage meter. Therefore, the AC source/meter directly measures the different conductance and the dI/dV-V can be measured by recording the dI/dV at

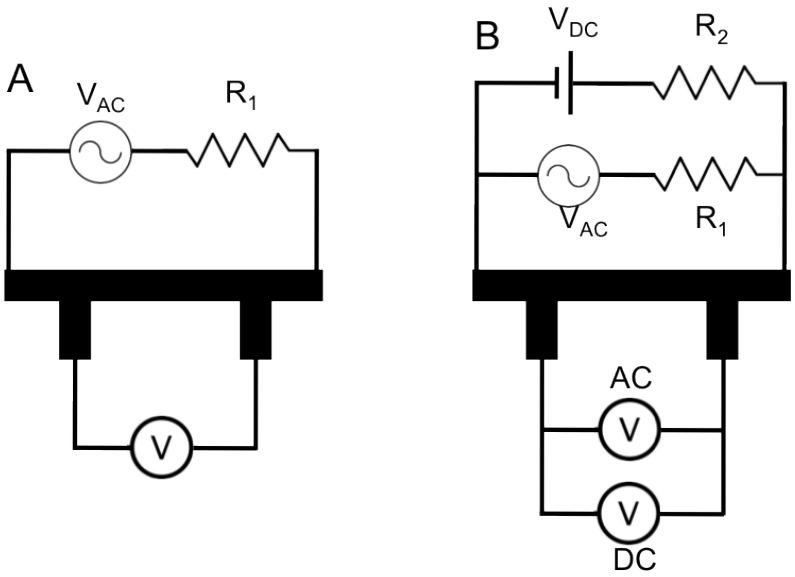

Figure 10: (A). A typical circuit for device resistance measurement using a lock-in amplifier. The output and the input of the lock-in issue drawn as AC source and meter in this figure. (B). A circuit for dI/dV-V measurement. The AC voltage source and meter is from the same lock-in. The DC voltage is provided by Keithley 2400 and the voltage is measured using Agilent 34410.

different DC voltages.

CHAPTER III

EPITAXIAL GRAPHENE GROWTH ON SIC

3.1 Silicon carbide

3.1.1 Silicon carbide structure

Silicon carbide (SiC) is comprised of equal amount of carbon (C) and silicon (Si) atoms. Each C atoms are bonded with four Si atoms and vise versa. A SiC crystal can be viewed as a stack of Si-C bilayers. When a new bilayer is added to the SiC crystal, it may stack in the same orientation as the layer beneath it, or it may rotated 60^o relative to the previous layer. This degree of freedom in the stacking allows SiC to have more than 200 crystal polytypes. Among these polytypes, the most important ones are the 3C SiC, in which all bilayers stay the same orientation; the 4H SiC, in which every other bilayer changes the stacking orientation; and the 6H SiC, in which the orientation changes every three bilayers[84]. The 3C SiC has a face-center cubic lattice structure and both 4H SiC and 6H SiC have a hexagonal lattice where the z axis periods equal 4 and 6 Si-C bilayers respectively[84](Figure 11). In this thesis, the mainly used SiC is on-axis semi-insulating 4H SiC, which is commercially available from Cree Inc. A semi-insulating substrate is critical for transport measurement.

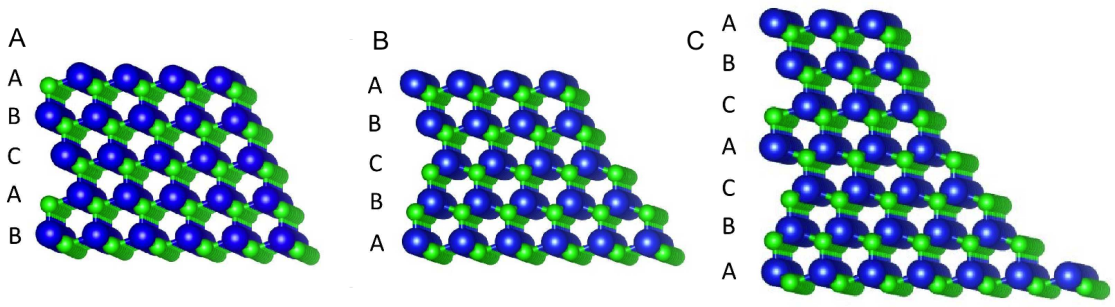

Figure 11: A Crystal structure of SiC polytypes. (A) 3C, (B) 4H, and (C) 6H SiC. Reprinted from [4].

Table 1: Facet slope angle relative to the (0001) surface

n	$(1\bar{1}0n)$	$(11\bar{2}n)$
1	75.1	81.3
2	62.1	73.0
4	43.4	58.6
8	25.3	39.3
12	17.5	28.6
16	13.3	22.2
32	6.7	11.6

3.1.2 Silicon carbide crystal facets

The commonly used SiC facets (on-axis facets) are the silicon-terminated SiC(0001) face(Si-face)and carbon-terminated SiC$(000\bar{1})$ face (C-face). SiC wafers cut along these two facets are on-axis wafers. However, even on-axis wafers have slight angles with respect to the perfect SiC (000 ± 1) surfaces. The mis-cut angle is on the order of 0.1^o for on-axis wafers. As a result, the surface of an annealed on-axis SiC wafer surface is composed of SiC steps with micrometer wide terraces. Besides the on-axis facets, SiC has other crystal facets with low crystal indies and can be stable in the high temperature anneal. An example of these are the SiC "sidewalls" that connect the terraces on the on-axis wafer surface. These low-index facets can be grouped as $(1\bar{1}0n)$ and $(11\bar{2}n)$ and their angles relative to the on-axis surface for 4H SiC are listed in Table (3.1.2).

3.2 Confinement controlled sublimation method

Van Bommel et al. first showed in 1975 that a graphene layer grows on hexagonal silicon carbide in ultrahigh vacuum (UHV) at temperatures above about 800 C [33]. Silicon sublimation from the SiC causes a carbon rich surface that nucleates an epitaxial graphene layer. The graphene growth rate was found to depend on the specific polar SiC crystal face: graphene forms much slower on Si-face than on the C-face. Van Bommel et al. identified monocrystalline graphite monolayer films (i.e., graphene) [33] that were found to be essentially decoupled from the SiC substrate [17] and therefore were electronically equivalent to isolated graphene sheets [85].

The first graphene transport measurements were performed on epitaxial graphene films

grown by sublimation in UHV[18], these mobilities are still low compared with nanotubes [86] or graphite [87]. Defects in UHV sublimed silicon carbide was traced to the relatively low growth temperatures and the high graphitization rates in the out of equilibrium UHV sublimation process. Whereas increased growth temperature will anneal vacancies and grain boundaries, the UHV growth method still leads to unacceptable high sublimation rates. There are a number of way to control the rate at which silicon sublimes. For example by supplying silicon in a vapor phase compound (e.g., silane [88]) or by flowing an inert gas over the hot silicon carbide surface [89].

The confinement controlled sublimation (CCS) method used by the Georgia Tech research group since 2002[18][19] relies on confining the silicon carbide in a graphite enclosure (either in vacuum or in an inert gas)[20]. This limits the escape of Si and thus maintains a high Si vapor pressure so that graphene growth proceeds close to thermodynamic equilibrium Figure 12(B). Graphene growth over macroscopic areas can be controlled on both polar faces of SiC to produce either monolayer graphene or multilayer graphene films(Figure 13(B)&(C)). Particularly relevant examples are the demonstration of infrared Landau level spectroscopy showing very high mobility [35], quantum Hall effect [34], scanning tunneling Landau level spectroscopy [90], fractional Landau level filling factors [91], and self assembly of graphene ribbons [92] large scale patterning, electronic confinement and coherence [19], electronic structure of decoupled layers in multilayered epitaxial graphene [9], [93].

The principle of CCS can be understood from kinetic gas theory[20]. Graphene growth is proportional to the rate of silicon depletion from the SiC surface, because each evaporated silicon atom leaves behind one carbon atom on the surface. In thermodynamic equilibrium the Si evaporation rate, n^-, and the Si condensation rate, n^+ at the SiC are exactly balanced so that graphene does not form. This condition will eventually be established in a hermetically sealed, nonreactive, enclosure at any temperature, after the enclosure surfaces have been passivated[20]. In this design, a graphite enclosure is used, and passivation of the enclosure is achieved after several graphene growth cycles. In more detail, assume that a Si atom impinging on the surface condenses with a sticking probability ϵ, $(0 \leq \epsilon \leq 1)$ then $n^+ = \epsilon v_{ave} \rho_{eq}$ where $v_{ave} = \sqrt{8KT/\pi m}$ is the average thermal speed of a silicon atom

in the vapor, m is its atomic mass and $\rho_{eq}(T)$ is the vapor density of silicon in equilibrium with silicon carbide at temperature T. Consequently $n^+ \approx \epsilon\rho_{eq}(2KT/\pi m)^{1/2}$. The sticking coefficient (but not the vapor density) depends on the local surface structure, and the polar face. For simplicity, in the rest of this discussion we assume $\epsilon = 1$, independent of T. However we note that graphene growth rates are greater on the C-face than on the Si-face, implying that ϵ is greater on the former than on the latter, which is important for certain implementations of the method. Clearly, the silicon must escape through the layers that have already formed, so that the rates depend on the graphene thickness. It appears however, that for thinner layers, silicon manages to readily escape from the silicon carbide surface.

If the enclosure is not hermetically sealed, but supplied with a small calibrated leak (Figure 12(B)), then $n^- > n^+$ causing graphene to grow at a rate $n^{gr} = n^- - n^+$[20]. Consequently, n^{gr} is controlled by the size of the leak[20]. In general, the rate at which silicon atoms escape is $N = Cv_{ave}/\rho_{eq}$, where C is the effective area of the leak (for a cylindrical hole of diameter D and length L, $C = D^3/3L$). Consequently, $n^{gr} = N/A$ where A is the crystal surface area[20]. For example, for a $1cm^2$ crystal in vacuum, with L=$1cm$ and D=$0.75mm$ the graphene formation rate is reduced by more that a factor of about 1,000 compared to the UHV sublimation method (in which $n^+ = 0$). Note that the carbon vapor pressure at the typical growth temperatures is approximately $10^{-10}Torr$, which is negligible compared to the Si vapor pressure or that of the residual gasses in the vacuum chamber, so that it is unlikely that gas phase carbon plays a significant role in the graphitization process[20].

The actual rates can be estimated from the vapor pressure of $P_{Si}(T)$ of Si over SiC, as has been determined by Lilov [94]: $P_{Si}(1500K) = 1.7 \times 10^{-6}Torr$. $P_{Si}(2000K) = 1.1 \times 10^{-2}Torr$, $P_{Si}(2500K) = 1.4Torr$, consequently, P_{Si} and ρ_{eq} increase by about a factor of seven per 100K[20]. Assuming the sticking coefficient for the C-face is $\epsilon = 1$, and that one carbon atom remains for every evaporated silicon atom, then a graphene monolayer forms on the C-face in about 1 min at $T = 1200^oC$ for a SiC crystal that freely sublimes in vacuum. This formation rate reasonably agrees with the experimental graphene formation

rate in UHV. Consequently, compared with the UHV sublimation method, the CCS method allows the sample temperature to be increased by about 300 K for a given rate of graphene growth[20]. This has been experimentally confirmed for the enclosure described above.

Introducing an inert gas further decreases the growth rate[20][89]. In that case, silicon atoms must diffuse through the gas-filled leak to escape the enclosure. This reduces the Si leak rate by a factor $R = (D/\lambda + 1)^{-1}$ where λ is the mean free path of a silicon atom in the gas (see, for example reference [95]). For example, for argon, $\lambda = (\sigma_{Ar-Si}\rho_{Ar})^{-1}$ where ρ_{Ar} is the Ar density and $\sigma_{Ar-Si} = 30\mathring{A}$ is the estimated [95] ArSi gas kinetic scattering cross section so that for $P = 1bar$, $R \approx 10^{-3}$ in the example above. Hence, the graphene formation rates can be reduced by an additional factor of up to 10^3 by introducing argon into the enclosed volume[20]. Consequently, the CCS method allows growth rates to be adjusted over a factor of 10^6 compared with UHV growth[20]. Moreover, the growth temperature and the growth rates can be independently tuned: coarsely tuned by the leak out of the confinement volume and finely tuned by introducing an inert gas[20]. Compared to the Edison Lightbulb Method introduced by Emtsev et al. [89], which only uses flowing argon to restrict Si sublimation, the CCS method is more flexible[20]. Furthermore, the Lightbulb method is intrinsically far from equilibrium and its effectiveness for C-face graphene growth has not yet been demonstrated[20].

3.3 Furnace design

During this research, I built and maintained a CCS furnace system. This system consists of three parts: a high vacuum chamber, heating components, and a feed-back controller. Details on each parts are as following.

• **Vauum chamber** The main component of the vacuum chamber is a test-tube-shaped jar made of quartz. Quartz is transparent and can withstand temperature exceeds 1,000^oC. The quartz tube is connected to a pump station through a six-way crosses and a vacuum hose. The pump station includes a mechanic pump and a turbo pump and can maintain the chamber at $10^{-6}mbar$ at the room temperature and $10^{-5}mbar$ when the heating components is at 1600 ^oC. In addition, three other components are connected to the crosses: a dual-range

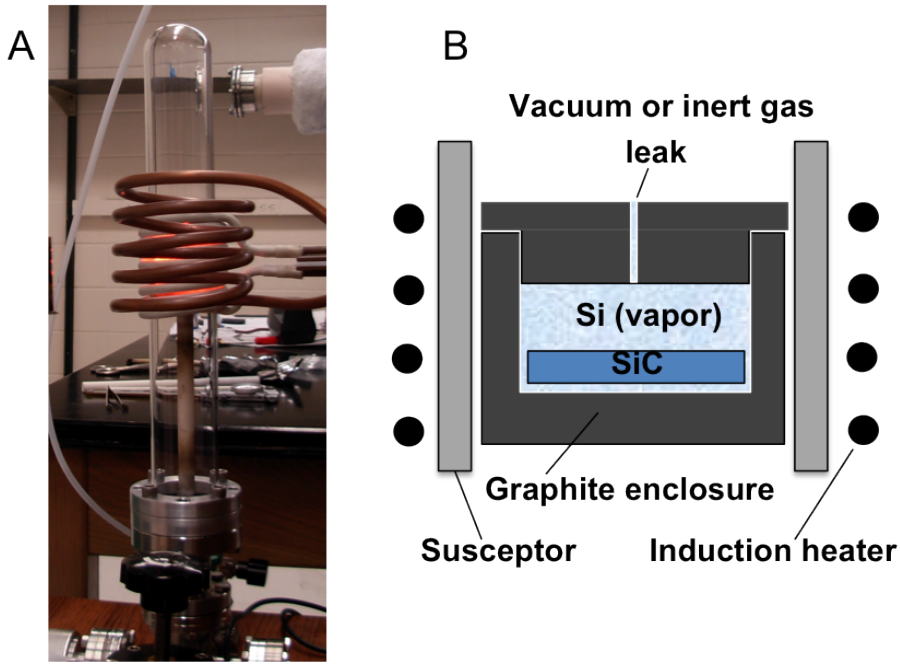

Figure 12: (A) The inductance furnace for graphene growth. (B) An illustration of the furnace design. The induction heater heats up the susceptor and the graphite enclosure. The enclosure contains the SiC chip and suppresses the sublimation rate of Si by confining the Si vapor from diffusing out of the enclosure.

vacuum gauge measures the chamber pressure from 1 bar down to $10^{-8} mbar$, a thermal couple outlet that allows the thermocouple reading, and a gas outlet that allows injection of Ar gas.

• **Heating components** The heating components consists of three layers. The outside layer is a ceramic enclosure made of foam aluminum oxide. This layer serves as thermal insulator that confines the heat radiation, so that the quartz tube can stay below its melting temperature and the required heating power stays low. The middle layer is a cup-shaped molybdenum susceptor for inductance heating. Molybdenum is commonly used in high temperature furnaces because of its high melting point. For the CCS furnaces, several high temperature materials were tested and molybdenum was chosen because it does not react with neither the outside aluminum oxide layer nor the inside graphite at high temperature. The graphite enclosure for graphene growth is inside the molybdenum cup. The enclosure contains SiC chips and confines the sublimation of silicon atoms. An additional graphite piece is inserted underneath the graphite enclosure to allow the direct contact with

a thermocouple wire, which goes through the holes drilled at the bottom of the outside and mid-layer components, for an stable and accurate temperature measurement. The heating components is supported by a ceramic rod. This design allows the furnace to be heated up to 1900 ^oC. Heating is achieved by activating an inductance coil placed outside the quartz tube. The radio-frequency currents in the coil generates an AC magnetic field that induces Eddy current in the mid-layer susceptor, so that the temperature of the heating components are raised.

•**Feed-back controller** The heating power from the inductance coil is determined by a feed-back controller. I wrote the controller program using LabView^{TM} on a PC. The controller reads the measured temperature and compares it with the set temperature to calculates the output power and then sends the control signal to the power supply of the inductance coil. This process is repeated every two seconds to allow a smooth control of the entire heating process. The output signal is calculated using the proportional−integral−derivative (PID) feed-back mechanism. The P, I, and D stand for the difference between the set temperature and measured temperature (ΔT), the time integral of ΔT, and the time derivative of ΔT, which provide the information on the current situation, the history, and the feature trend of the heating system. Each of the three terms is assigned with a weight(PID parameters) that quantifies their importance in determining the output value. The PID parameters require adjustments for each heating system. The D parameter is set at zero in the CCS furnace, because it amplifies the noise in the temperature measurement and the temperature control is good enough will P and I terms.

The recipe for graphene growth includes three temperature stages. The first stage is around 200 ^oC and removes surface-adsorbed molecular from the air, such as water. The second stage is at 1200 ^oC and removes natural oxide on SiC surface and allow the mass flow on SiC surface to form steps. The cleaned sample is then heated up to the last stage for graphene growth. The exact temperature and time for the graphene growth varies, depending on the graphite enclosure design, the temperature calibration, and the type of graphene grown on the SiC. For instance, the growth of 5-10 layers graphene on the C-face requires 1550 ^{o}C for 10 mins and monolayer graphene on the Si-face requires 1600 ^{o}C for

20 mins.

3.4 Graphene growth on polar surfaces

Van Bommel first observed the differences between graphene grown on the Si-face and the C-face of hexagonal silicon carbide [33] . Low-energy electron diffraction (LEED)[18] and angle resolved photoemission spectroscopy (ARPES) reveal that Si-face graphene monolayers exhibit the characteristic linear bandstructure[96]. Typical monolayer mobilities using CCS on the Si-face are found to be modest and typically on the order of $10^3 cm^2 V^{-1} s^{-1}$[89]. Like in graphite, Si-face graphene multilayers are Bernal stacked[96][97]; Si-face grown bilayers exhibit parabolic bands and with increasing thickness, the band structure evolves to that of graphite [96]. Consequently Si-face graphene multilayers are actually ultra-thin graphite films and known as few layer graphite (FLG)[20].

Van Bommel also observed that UHV grown graphene on the C-face is both rotationally disordered and defective [33]. However, C-face graphene grown by the CCS method shows rotational order, consisting primary of two principle rotational orientations[93], in contrast to the single orientation in Bernal-stacked graphene and Si-face FLG[96]. Whereas the exact structure is not known, it is consistent with a stacking where every other layer is aligned within approximately 7^o of the SiC $< 21\bar{3}0 >$ direction and separated by layers rotated by 30^o with respect to the $< 21\bar{3}0 >$ direction[93] (Bernal stacked layers make up no more than 15% of the film and are considered stacking faults in this structure) [98]. An important consequence of this stacking is that each graphene layer in the stack has the same electronic structure as an isolated graphene sheet and therefore behaves as if it is electronically decoupled from its neighbor[93]. Therefore, C-face multilayers produced by the CCS method are multilayer epitaxial graphene (MEG)[99], [93] and not thin graphite. This important property has been confirmed by a variety of probes. For instance the Raman spectrum of the approximately 100 layer MEG sample of Figure 14 shows the characteristic G and single Lorentzian 2D peaks of single layer graphene. More specifically, ARPES was used to directly image the linear graphene band structure [92]. In addition, optical transitions between Landau levels in MEG have been observed even at room temperature

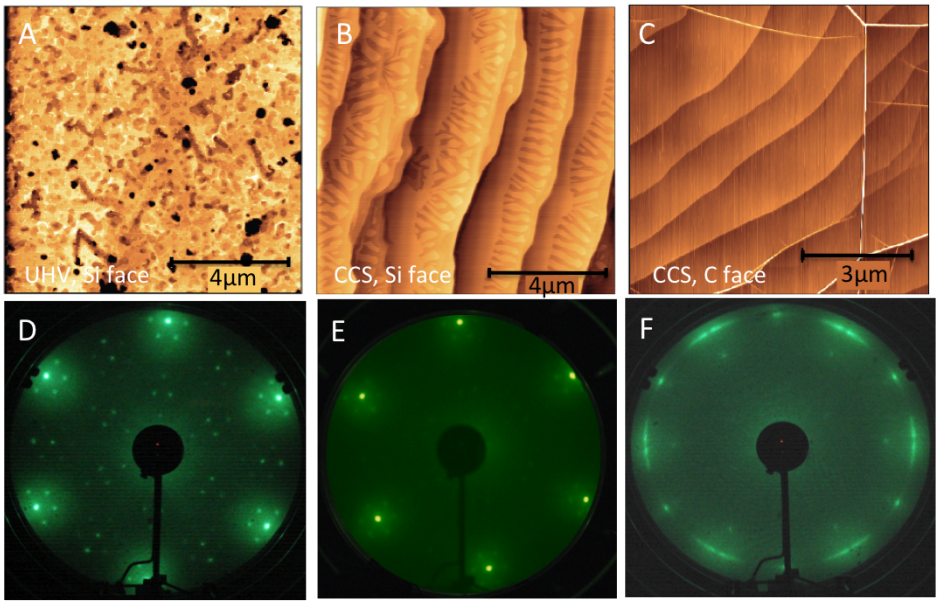

Figure 13: AFM topography images of (A) UHV-grown graphene on the Si-face, (B) CCS-grown graphene on the Si-face, and (C) CCS grown graphene on the C-face. (D)-(G) Low-energy electron diffraction patterns of Si-face UHV, Si-face CCS, and C-face CCS graphene samples.

in low magnetic fields, indicating very weak electron phonon coupling and room temperature mobilities exceed $250,000 cm^2 V^{-1} s^{-1}$ for interior MEG layers [35]. These features are clearly important for graphene science. Recent low temperature high magnetic field scanning probe investigations have directly imaged the quantum Hall states in MEG [90]. This work also demonstrated that MEG layers are atomically flat (with 50 pm height variations) between substrate steps (that can be up to 50 μm apart). An important property of both varieties of EG produced by the CCS method, is that the graphene layers are continuous over substrate steps: the morphology is likened to a carpet that is draped over the SiC surface [99]. In fact scanning tunneling microscopy has not revealed a break in the top graphene layer[90]. Hence, at least the top MEG layer covers the entire surface of a macroscopic SiC wafer.[20]

The graphene/SiC interface on the Si-face is well understood and is defined by a non-conducting carbon rich buffer layer with a $6\sqrt{(3)} \times 6\sqrt{(3)}$ structure that causes a corrugation between 0.5-0.8 $\AA$ of the first graphene layer [100]. The C-face interface is less well-understood so it will not be covered in this thesis. On both faces, the graphene/SiC interface is charged, inducing a negative charge density $n_{gr} = 5 \times 10^{12} - 1 \times 10^{13} cm^{-2}$

on the first graphene layer[19]. ARPES and transport measurements show that this layer (C-face) or the layer just above it (Si-face) in CCS produced epitaxial graphene has the characteristic linear graphene dispersion and high mobility (graphene ribbon mobilities are $500 - 2000 cm^2 V^{-1} s^{-1}$ for the Si-face and $10,000 - 30,000 cm^2 V^{-1} s^{-1}$ for the C-face) [99]. The interior layers in MEG are essentially neutral (a screening length of about one layer has been measured ([101], [102])).

As an important indicator for graphene quality, the quantum Hall effect (QHE) is observed on both C-face and Si-face monolayer graphene grown in my furnace, as plotted in Figure 14. The $n = 0$ QHE plateau is observed in both Hall bar samples when the carrier density is about $1 \times 10^{12} cm^{-2}$. The low carrier density in the C-face sample is by environmental doping that compensates the n doping, which compensates n doping from the substrate[34]. The mobility of the C-face device is about $5,000 cm^2 V^{-1} s^{-1}$[34]. Meanwhile, the carrier density in the Si-face sample was tuned by a local top gate. The quantum Hall plateau becomes significant at low carrier density and the sample mobility at this carrier density is about $4,100 cm^2 V^{-1} s^{-1}$[103]).

3.5 Templated graphene growth on SiC sidewalls

The phenomena that graphene can epitaxially grow on SiC are not limited to the two polarized faces. Other crystal facets such as $(1\bar{1}0n)$ and $(11\bar{2}n)$ can also be the substrate for graphene growth[92]. This section will discuss about graphene growth on these off-axis crystal facets, i.e., sidewalls.

3.5.1 SiC faceting

Surfaces with relatively low energy, like the low-index off-axis SiC facets $\{1\bar{1}0n\}$ and $\{11\bar{2}n\}$ are preferred in high temperature annealed[92][20]. For example, the hydrogen etched SiC surface always has terraces that are aligned along the $< 1\bar{1}00 >$ or $< 11\bar{2}n >$ directions. The faceting can be illustrated in the mesa experiment. The on-axis Si-face SiC is patterned into mesas with 1 μm in diameter and 100 nm in height. As shown in Figure 15, the patterned mesa is almost circular with some lithography defects around the edge. The sidewall slope around the mesa edge is about 70^o from the bottom, which is determined

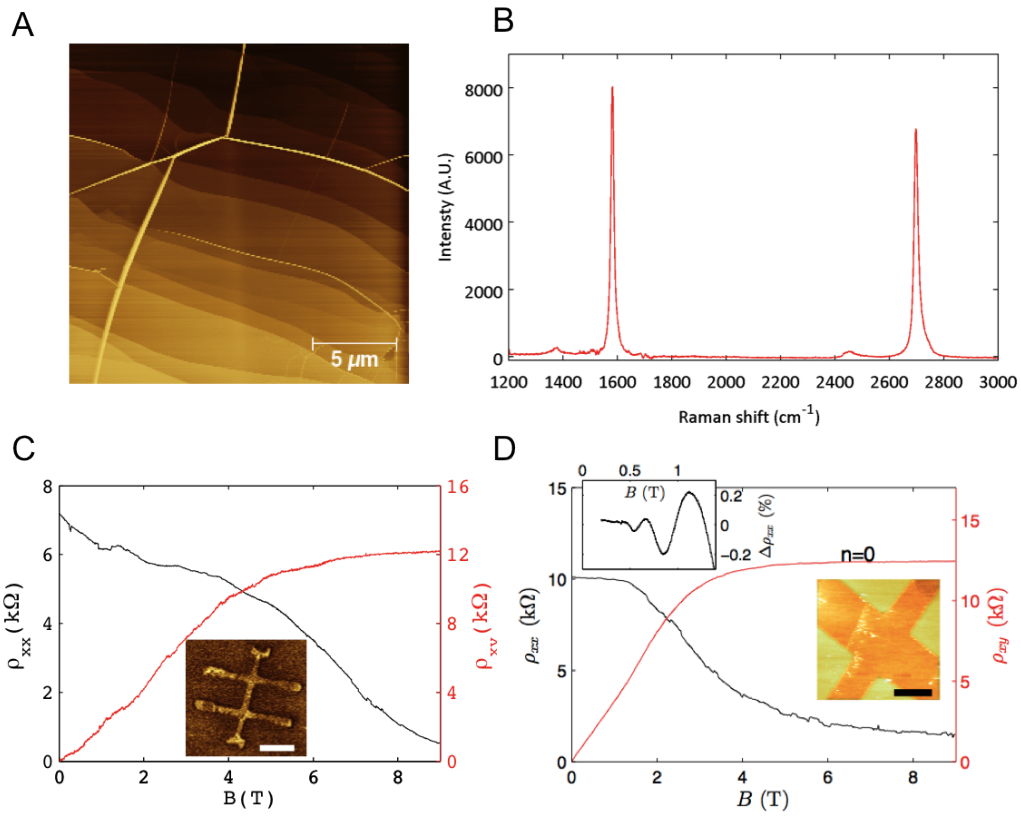

Figure 14: (A) A $20\mu m$ AFM image of C-face MEG. (B) A typical Raman spectrum of MEG. (C) QHE observed on Si-face graphene. Inset: EFM image of the Si-face Hall bar. (D) QHE observed on C-face graphene. Top inset: magnetoresistance ρ_{xx}. Very weak oscillation can be discerned at n=1, 2, 3. Bottom inset: AFM image of the Hall bar device. Both scale bars are $2\mu m$

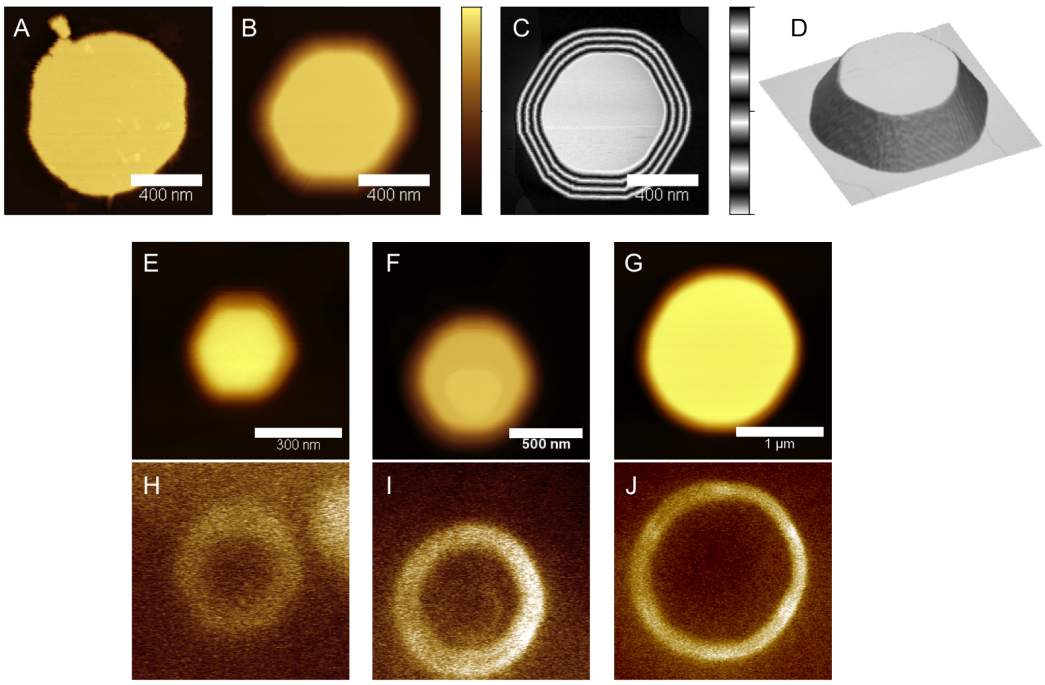

Figure 15: Faceting and selective graphene growth of mesas on SiC (0001) surface. (A) AFM image of a SiC mesa fabricated by e-beam lithography. (B)-(D) AFM images of the same mesa after furnace annealing. Images are in color scale, periodical color scale, and three-dimensional view for (B), (C), and (D) respectively. Vertical scale: 120nm. (E)-(G) AFM images of SiC mesas with different diameters after graphene growth. (H)-(J) EFM amplitude images of the mesa showing graphene forms preferentially on sidewalls.

by the plasma etching process. After annealed at 1600 ^oC in the CCS furnace, the mesa transfers into an almost perfect hexagon and the sidewall slope is significantly reduce to about 29^o. The orientation of the hexagon and the slope angles are used to determine the crystal indices. According to the hexgon, the facet with the lowest energy are toward the $< 1\bar{1}00 >$ directions and the secondary facets, which appears at the corner of the hexagon are toward the $< 11\bar{2}0 >$ directions.

3.5.2 Selective graphene growth on sidewalls

Crystal faceting is not the only phenomenon take place at the SiC surface when sidewalls are present. The other important finding is that the graphene grows faster on the sidewall than it does on the Si face. Difference in graphene growth rate can be observed in cross section high-resolution transmission electron microscopy (HRTEM) image of a step with both the sidewall and the Si face after long-time graphene growth in the furnace[92](Figure 16). In

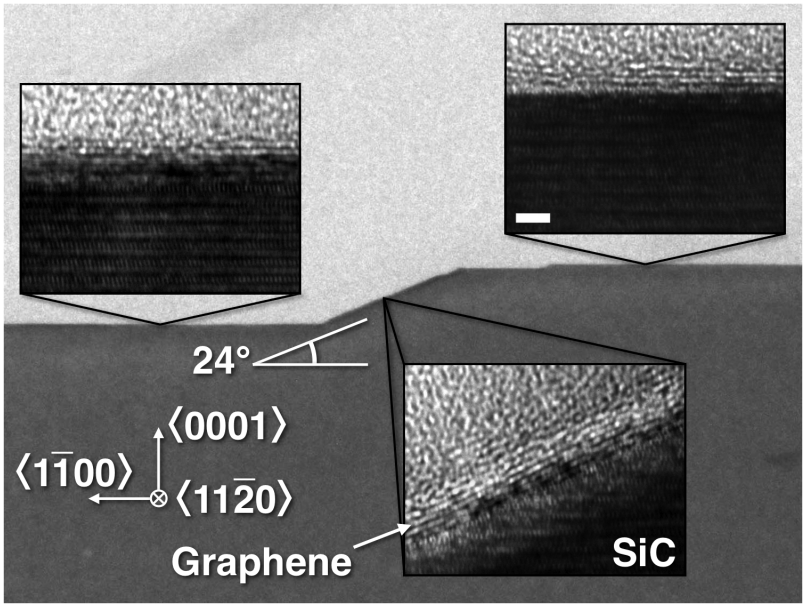

Figure 16: HRTEM cross-sectional images of a similar step on (0001) confirm preferential growth on the $(1\bar{1}0n)$ facet. Scale bar, 2 nm (and for all insets).

this image, more than six layers of graphene can be counted on the sidewall while the the Si-face only has two to three layers of graphene. This sample was lithographically patterned to have a 100nm deep sidewall towards the $[1\bar{1}00]$ direction. The annealed sidewall is 24^o from $\{0001\}$, indicating a faceted index of $(1\bar{1}08)$.

By optimizing the annealing parameters, graphene can form preferentially along sidewalls without any forming any graphene on the Si-face. This selective growth of graphene can be observed in both Raman mapping and electrostatic force microscopy(EFM) image[92]. Figure 17 shows the Raman spectra 2D peak intensity mapping of a patterned SiC surface after graphene growth. In this image, the 2D peak intensity is near zero every where except along the sidewalls. The EFM images of SiC mesas show that these mesas not only facet into hexagons but also form hexagonal graphene rings along the sidewalls.

By taking advantage of selective growth, the self-organized patterning of graphene becomes possible. In this technique, Si-face SiC is patterned to expose sidewalls. which will facet during annealing and become the template for graphene growth. Graphene will selectively form along the template to have desired shape and no subsequent lithography on the graphene is required. The whole process can be summarized as following[92]: (i) The

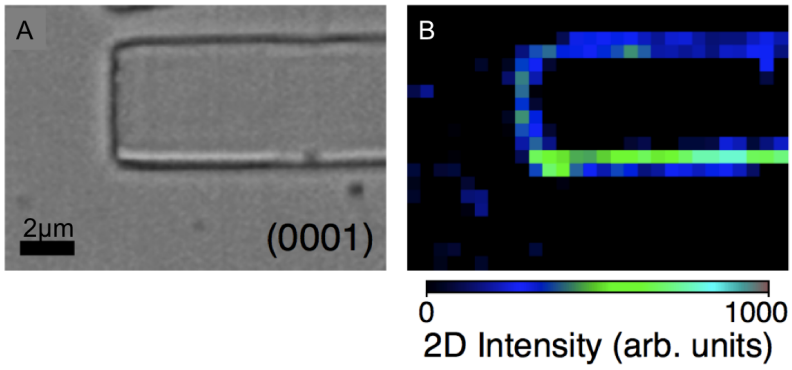

Figure 17: Raman spectroscopy of graphene selectively grown along SiC sidewalls. (A) Optical microscopy image of patterned SiC surface. (B) Intensity mapping of 2D peaks in Raman spectra of graphene

Si-face SiC is patterned to expose sidewalls; (ii) the SiC sidewalls facet into low index crystal faces during the high temperature annealing; (iii) graphene preferentially forms on the faceted sidewalls; and (iv) devices components such as contacts and top gates are fabricated to finish a device (Figure 19). Compared with conventional lithography, the selective growth does not save lithography steps, but it keeps the graphene film intact by avoiding the usual plasma etching step. Therefore, the edge of the graphene pattern is expected to have much fewer defects. This feature will become a big advantage when the dimension of graphene devices falls below 100nm. Figure 18 shows a few examples of self-organized graphene patterns.

3.5.3 Templated growth case study: sidewall Hall bar

One of the most important devices for transport measurement is the Hall bar[19][41][42]. A Hall bar is a two-dimentional ribbon with at least two arms on each side. This geometry allows the measurement of both the four-point resistance and Hall voltage at the same time. A conventional graphene Hall bar is lithographically shaped by plasma etching. In contrast, the fabricate of a sidewall graphene Hall bar starts from patterning the SiC template. This patterning includes two steps, as illustrated in Figure 19. The first step defines the sidewall for the main ribbon by covering half of the SiC surface with a Ni mask during a 300nm $CF_4/O_2/Ar$ plasma etching. After removing the first Ni mask, the second Ni mask is patterned to expose the Si surface perpendicular to the main ribbon.

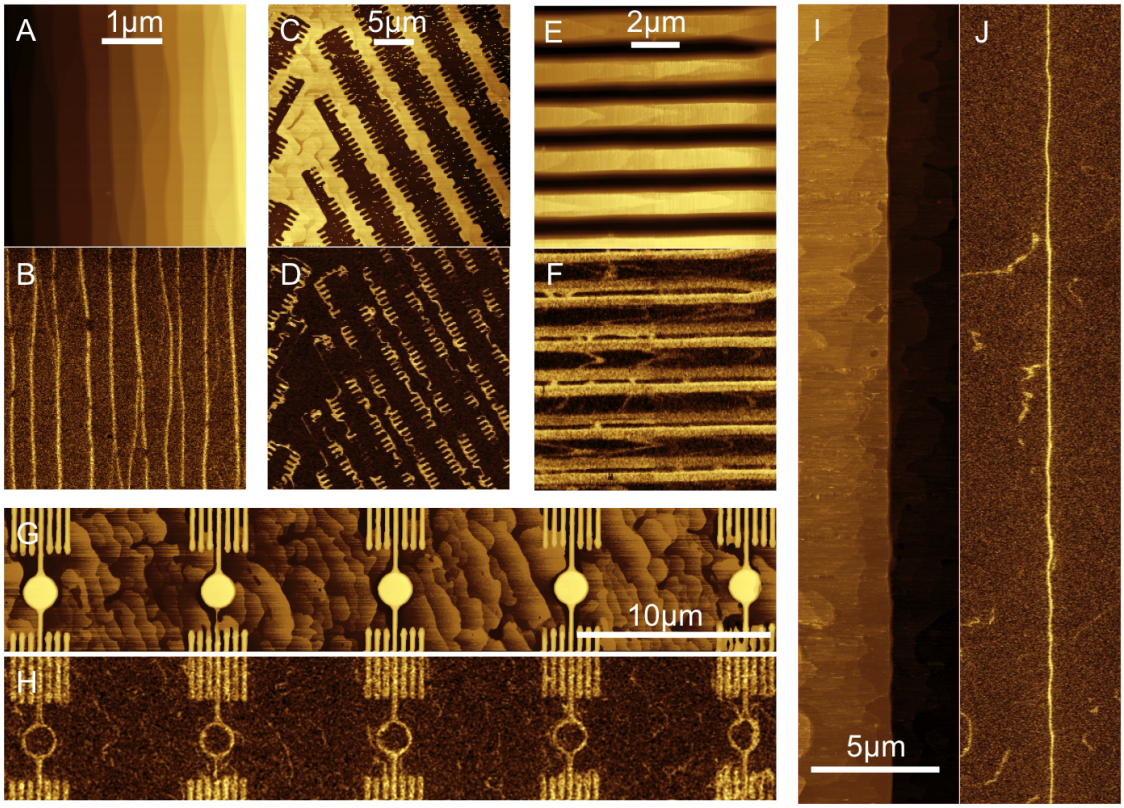

Figure 18: A few examples of templated graphene growth. (A) and (B) AFM and EFM images of parallel graphene ribbons grew along bunched SiC step edges. (C) and (D) AFM and EFM images of a patterned SiC surface for graphene ribbons. (E) and (F) AFM and EFM images of wide sidewall graphene ribbons. (G) and (H) AFM and EFM images of sidewall graphene rings. (I) and (J) AFM and EFM images of a continues graphene nanoribbon at least 30um in length.

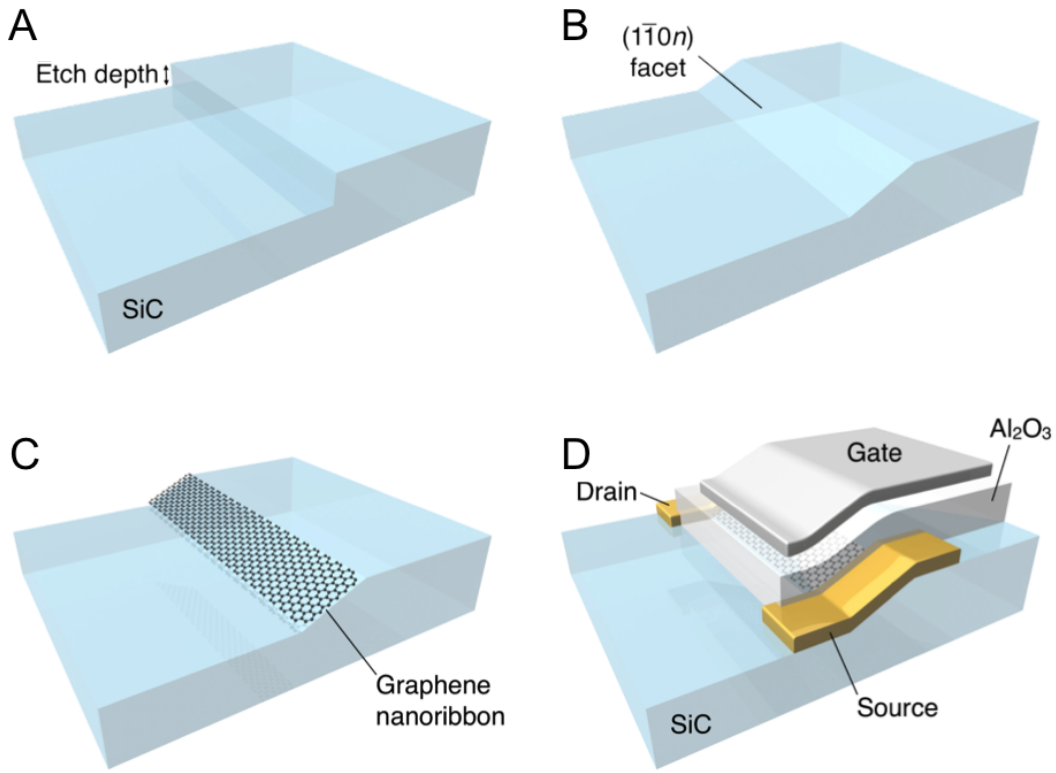

Figure 19: Process for tailoring of the SiC crystal for selective graphene growth and device fabrication [92]. (A) A nanometre-scale step is etched into SiC crystal by fluorine-based RIE. (B) The crystal is heated to 1,200-1,300 ^{o}C (at low vacuum), inducing step flow and relaxation to the (1$\bar{1}$0n) facet. (C) Upon further heating to $\sim$1,550 ^{o}C, self-organized graphene nanoribbon forms on the facet. (D) Complete device with source and drain contacts, graphene nanoribbon channel, Al_2O_3 gate dielectric and metal top-gate.

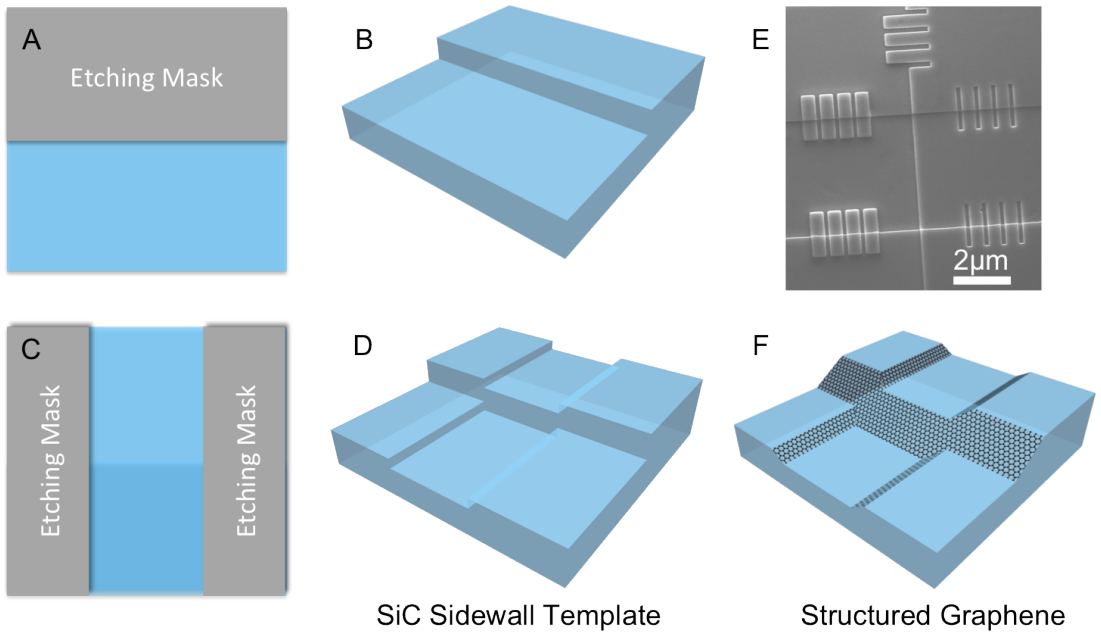

Figure 20: Illustration of the lithography process of sidewall Hall bars. (A) A flat SiC surface is partially covered with etching mask. (B) Plasma etched SiC surface. The residual etching mask has been removed. The sidewall here will become the major sidewall for graphene Hall bar growth. (C) The same SiC surface is covered by another etching mask perpendicular to the main sidewall. (D) A 3D view after the second plasma etching. The etching mask has been removed. Sidewalls for Hall bar arms are clearly seen. (E) A top view SEM image of a patterned SiC surface with the template for the growth of graphene Hall bar. Extra small features are added for larger contact area between graphene and metal lead. (F) Graphene with Hall bar shape forms along the sidewalls

The exposed SiC surface is then etched down by 150nm using the CF_4/O_2 plasma and the Ni mask is removed afterwards. One main sidewall and two sidewalls perpendicular to it combined to form a Hall bar template (Figure 20). A real Hall bar template also includes extra small features for larger contact area between graphene and metal leads. The scanning electron microscopy (SEM) image in Figure 19(E)shows the top view of a patterned Hall bar templated.

The patterned SiC chip was then loaded into the furnace for graphene growth. With proper graphene growth parameters, the SiC sidewalls will first facet into low-index crystal faces, then graphene will grow along the sidewall but not on the SiC (0001) terrace. Figure 21 compares the SEM images of a SiC Hall bar template before and after graphene growth. Before annealing, the SiC sidewalls are almost vertical with sharp corners around edges.

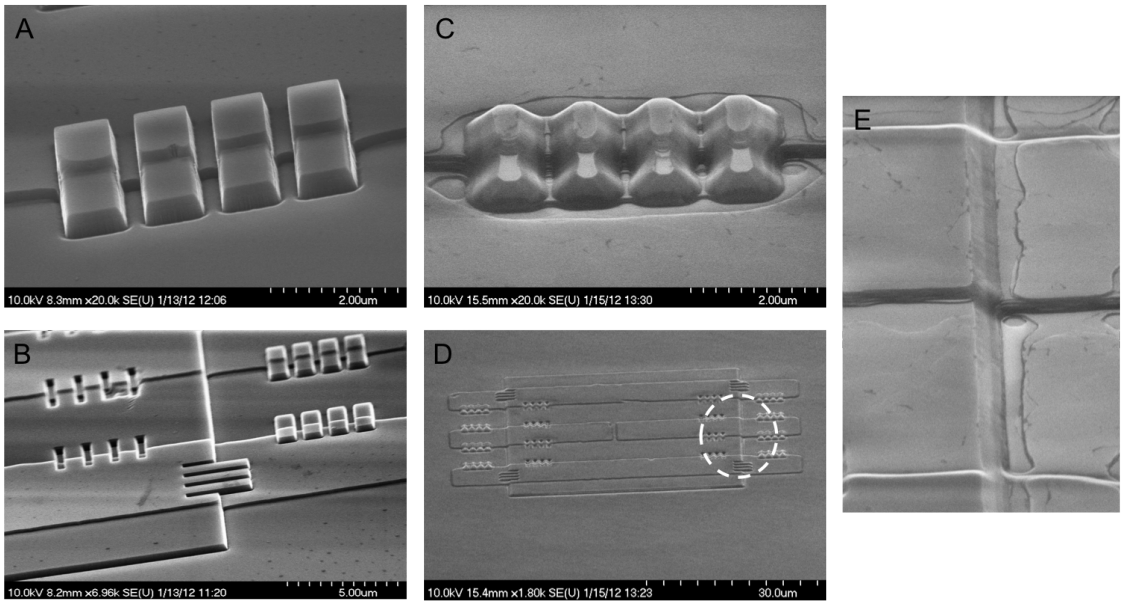

Figure 21: (A) and (B) SEM images of lithographically patterned SiC surface for sidewall wall graphene Hall bar growth. A overlook of the whole pattern (B) and a zoom in view of fine features (A). (C)-(E) The same SiC surface area after graphene growth. (C) The fine features faceted into hexagon edges with small slope angles. (D) A overlook of the entire device. (E) A zoom in view of the area marked in (D).

After annealing, the small patterns round into hexagons and the sidewalls acquire smooth slopes with relatively small angles with respect to the substrate.

More details about the sidewall Hall bar can be found from the AFM and EFM images. The sidewall Hall bar shows a slope angle about 39^o (Figure 22), which matches well with the angle for the $(11\bar{2}8)$ facet, according to Table 3.1.2, suggesting a well defined substrate for sidewall graphene. In addition, a side-by-side comparison of the AFM error image and the EFM image shows where graphene grows. The AFM error records the deviation of the tip-sample distance from the set point, thus it is sensitive to topography changes, for example, sidewalls. The sidewalls found in the AFM error image are identical to the graphene pattern seen in the EFM image, suggesting that the graphene growth is perfectly selective.

After the the contacts were fabricated, the sidewall Hall bar sample was cooled down to liquid helium temperature for electron transport measurements. The magnetic field was swept up to 9T for the magnetoresistance measurement. To reach the best effect on

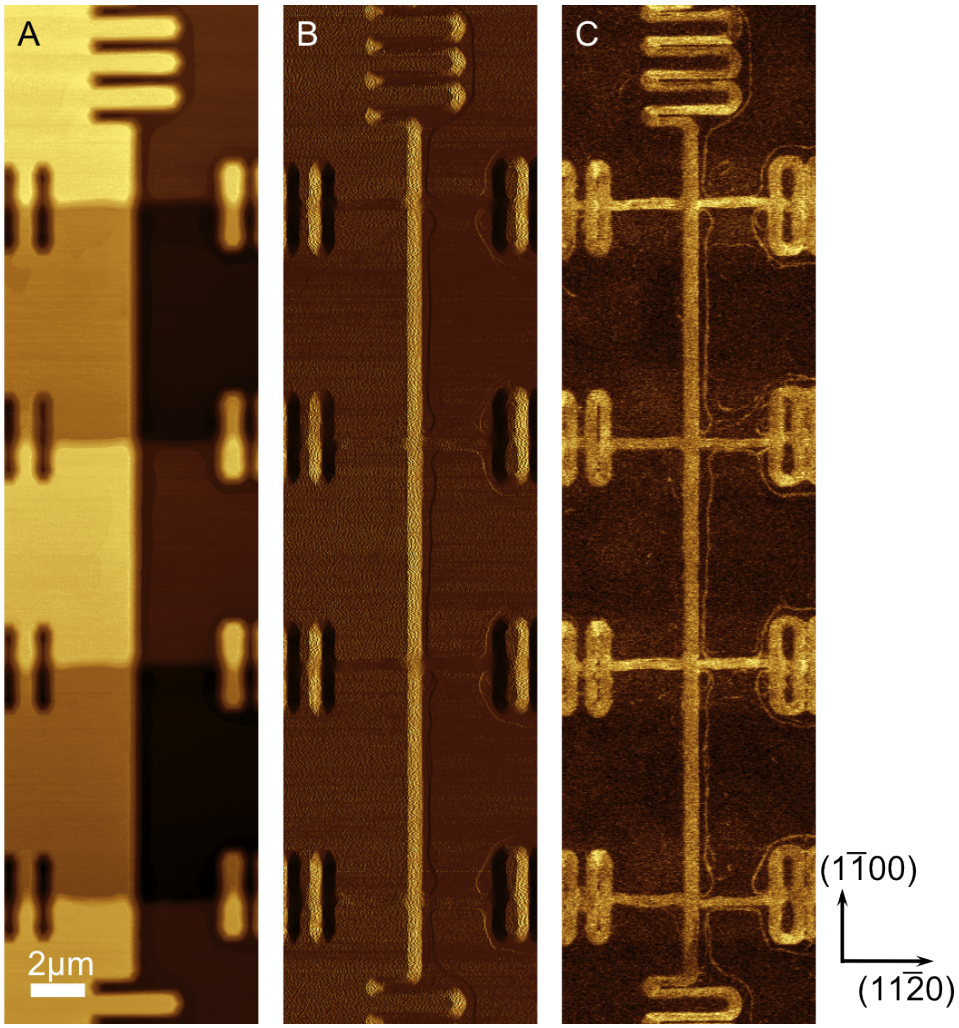

Figure 22: (A)-(C) AFM topography, AFM error, and EFM amplitude images of a sidewall graphene Hall bar.

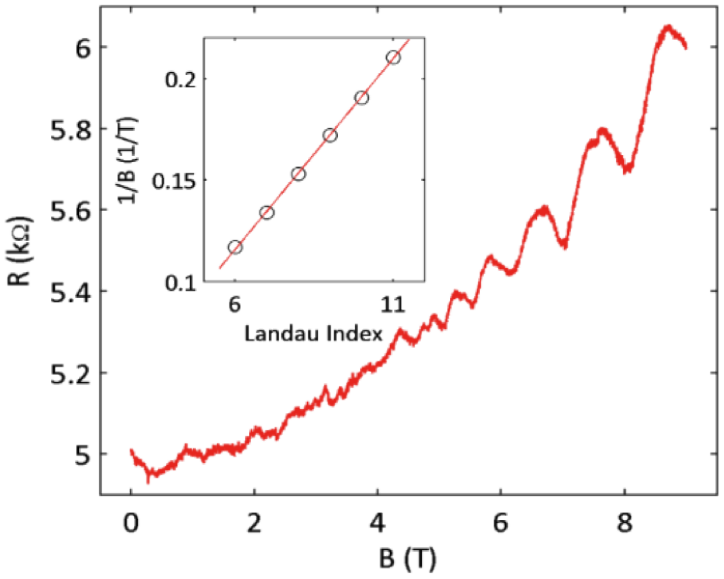

Figure 23: shubnikov de Haas oscillation observed on a sidewall Hall bar sample. The oscillation maxiums vs Landau index is plotted in the inset.

magnetic field, the sample was rotated to have the sidewall Hall bar perpendicular to the magnetic field. The Shubnikov-de Hass (SdH) oscillations were observed on a sidewall Hall bar sample, as plotted in Figure 23. The inverse of the the field for SdH oscillation maxima are linearly correlated with the Landau indices, as plotted in Figure 23. The slope of this linear relation indicates a carrier density equals $5.1 \times 10^{12} cm^{-2}$. The intersection of the linear fit is nearly zero, suggesting the Berry's phase in this Hall bar material equals π, a feature that only belongs to monolayer graphene but not graphite[19]. Therefore the material selectively grown on the sidewall is either a monolayer graphene or electronically decoupled few layer graphene with the electron transport dominated by the bottom layer, similar to graphene grown on the C-face [19].

CHAPTER IV

SIDEWALL GRAPHENE NANORIBBON

4.1 Introduction

4.1.1 Background

The excellent properties of carbon nanotubes provided a model[18][104] for graphitic electronics based on one-dimensional ballistic transport[105][106], promising ultra-high-speed nanoelectronics that could outperform standard semiconductor electronics. However, nanotubes are difficult to select, assemble, and interconnect. In contrast, interconnected graphene nanostructures constructed by lithographically patterning graphene sheets deposited on an insulating substrate promised to resolve this problem[18][104] and nanopatterned graphene transistors demonstrated impressive electronic switching properties[52]. However, electronic scattering effects at rough and poorly defined edges were found to dominate electronic properties[107][108]. This disorder-induced mobility reduction erases the advantage of graphene compared to standard semiconductors[48], not only indicating that lithographically patterned graphene sheets, despite how perfect they are before patterning, are not suitable for high-speed graphene nanoelectronics, but also casting doubt on the viability of graphene nanoelectronic[48]. Consequently, industry now focuses primarily on graphene analog devices on the micron scale (not the nanoscale)[109][110][44], but even these devices cannot compete with standard semiconductor technology, which has achieved frequencies as high as 500 GHz[111]. This chapter provides a new scalable method that overcomes the rough-edge problem in the graphene nanostructure. Metallic graphene nanoribbon devices fabricated with this method show near-ballistic transport properties, which suggests a new route for graphene nanoelectronics.

4.1.2 Theories

4.1.2.1 Band structure of graphene nanoribbons

As a one-dimensional (1-D) form of graphene, graphene nanoribbons are graphene with a lateral confinement, which results in the quantization of the transverse momentum of electrons (k_y) and breaks the band structure of 2-D graphene into a series of 1-D sub-bands. As a result, the band structure of a graphene nanoribbon depends on the orientation of the ribbon relative to the graphene lattice ("chirality")[46]. Two main chiralities of graphene nanoribbons are armchair and zigzag. The armchair chirality is parallel to the direction of the C-C bond and the zigzag chirality is 30^o rotated from the armchair. Band structures of both cases can be calculated using the nearest-neighbor tight-binding method (Figure 24)[46]. Compared with the 2-D graphene band structure (Figure 2(A)), the 1-D band structure of graphene nanoribbons are subsets of the band structure of graphene projected along directions defined by the chirality[46]. However, this relationship still has an exception: two flat bands at $\frac{2}{3}\pi/a < |k| < \pi/a$ in the zigzag ribbon (Figure 24(A)) do not have counterparts in the band structure of 2-D graphene. These flat bands are localized states of electrons and holes at the edge of the nanoribbon and belong to the bottom conduction band and the top valence band. Also, the flat band is not a unique feature of the zigzag nanoribbon, but instead, it appears in graphene nanoribbons of any chirilaty except for armchair nanoribbons. [46][112].

4.1.2.2 Perfect conduction channel in graphene nanoribbons

One important effect originating from the flat bands is that nanribbons might contain perfect conduction channels (PCC). A PCC is a channel with transmission coefficient equals one[37]. The PCC does not exist in regular parabolic sub-bands of graphene nanoribbons, in which both intervalley and intravalley scattering of electrons are allowed. In contrast, the sub-band with a flat-band forbids the intravalley scattering because of the absence of backward-moving states in a single valley (Figure 25). Meanwhile, the intervalley scattering is suppressed in graphene nanoribbon with few lattice defect, because the conservation of

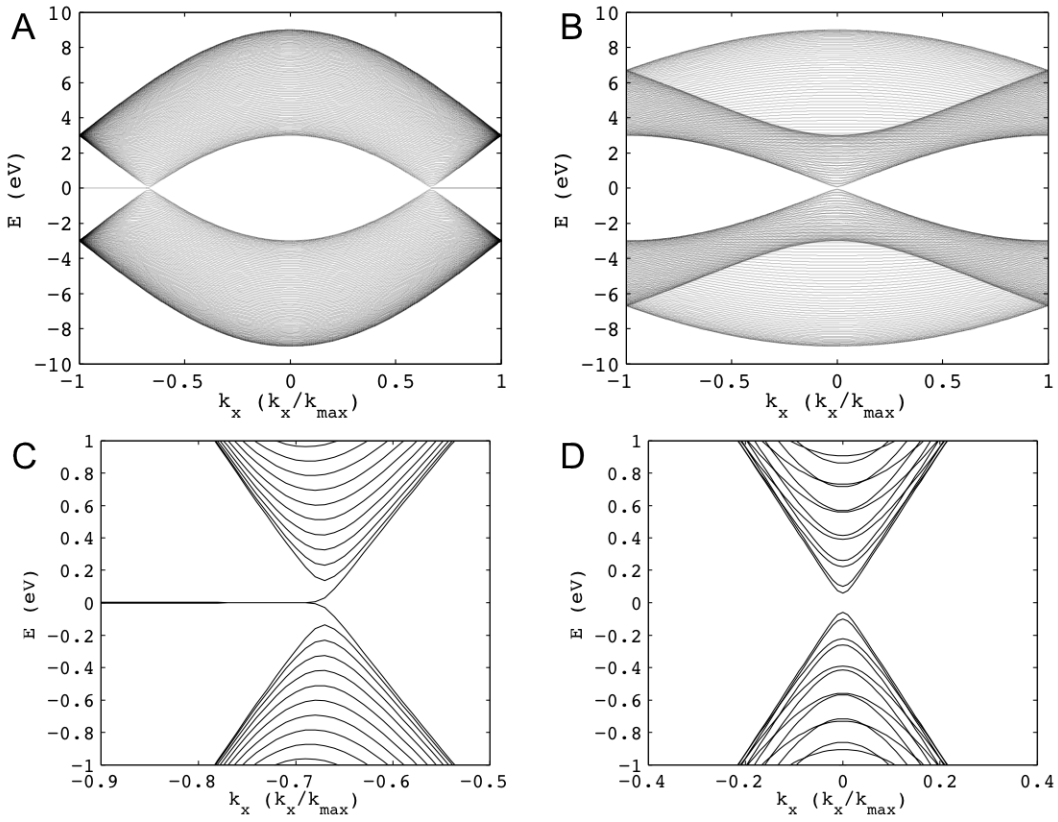

Figure 24: Tight-banding calculation of zigzag (A) and armchair (B) graphene nanoribbons. Both ribbons contains 50 unit cells across the ribbon. (C) and (D) are zoom view of (A) and (B) near the Dirac point. The calculation uses the online source provided by [5]

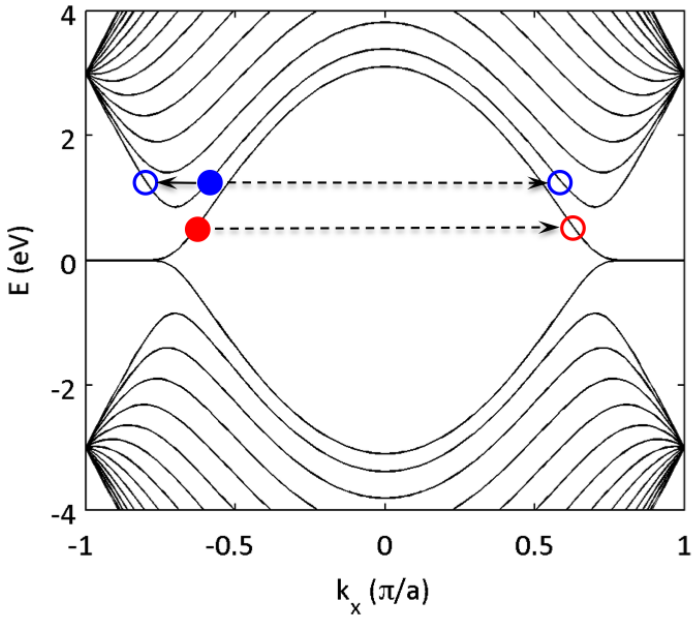

Figure 25: An illustration of the PCC in graphene nanoribbon with edge states. For electrons at normal state (solid blue), both intervalley (dashed arrow) and intravalley scattering (solid arrow) can happen. However, for electrons on the edge state band, only intervalley scattering can happen.

momentum requires large momentum from scattering, which can only be provided by short-range scatters like lattice defects[113]. Therefore, in a high quality graphene nanoribbon, the flat-band channel is a PCC which has conductance equals $2e^2/h$[113]. The total conductance of a graphene nanoribbon are the sum of the conductance of all occupied channels, among which the flat-band channel is the only channel that remains perfect despite the length of the ribbon while the transmission coefficient of other channels decreases as the increase of the length of the ribbon. As a result, the conductance of a long graphene nanoribbon ($\sim 1\mu m$) is dominated by the PCC and should have a value close to $2e^2/h$[113][112].

4.1.2.3 Electron tunneling through a graphene PN junction

Electron tunneling in a graphene PN junction differs from the way it is in regular PN junctions. In a regular junction, electrons have very little possibility to tunnel through the junction since the electron movement is blocked by the strong built-in electric field. In contrast, electrons have a much higher possibility to tunnel through a graphene PN junction

as a result of the absence of the band gap and the linear dispersion relation in graphene. The principle of the electron tunneling process in a graphene PN junction is illustrated in the abrupt junction model (a step-like potential)[10]. In this model, the transmission coefficient of an electron through a PN junction with equal density of electrons and holes is[114]

$$|T_{step}|^2 = \cos^2\theta, \tag{24}$$

in which θ is the incidence angle of the electron. In the case of normal incidence, the PN junction is transparent, which is not surprising since normal back scattering is forbidden in defect free graphene. When electrons are incident at an angle, back scattering occurs. The transmission coefficient becomes less than one and decreases quickly as the incidence angle increases.

A PN junction model closer to the reality is the smooth junction, in which a smooth transition region with uniform electric field is added between the P- and N-doped regions. The transmission coefficient of an electron in a smooth junction with equal density of electrons and holes is [114]

$$T_{k_y}^2 = e^{-\pi\hbar v_F k_y^2/(eE)}, \tag{25}$$

in which v_F is the Fermi velocity, k_y is the lateral momentum of an electron, and E is the uniform electric field inside the junction [114][7]. In this model, the PN junction is still transparent to normal incident electrons, and the transmission coefficient decreases faster as the incidence angle increases than for an abrupt junction. In graphene nanoribbons, since the PCC (see the last subsection) is the only channel with normal incidence angle ($k_y = 0$), its contribution to total conductance will become more significant when a PN junction is present, which can be achieved by fabricating a top gate perpendicular to the nanoribbon.

4.2 Device fabrication and calibration

4.2.1 Device fabrication

The fabrication of sidewall graphene nanoribbon devices follows the templated graphene technique [92] discussed in the previous chapter. For nanoribbon growth, the sidewall template has to be just a few nanometers in height so that the subsequently formed graphene

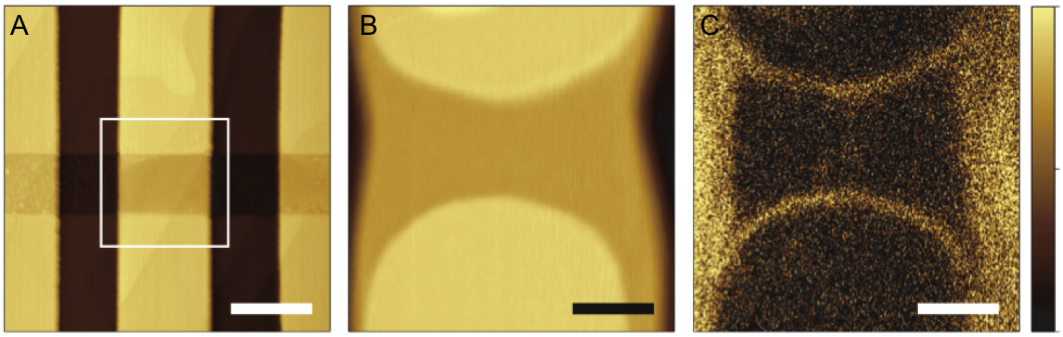

Figure 26: AFM/EFM observation of sidewall graphene nanoribbons of width 40 nm. (A) AFM topography of patterned SiC structure on (0001) before graphene growth. Horizontal trench of depth 20 nm (to become the active device area) is flanked by trenches of depth 100 nm (to become interconnects). (B) AFM (topography) detail of white outlined area in a following graphene growth. SiC step bunching and step flow cause the patterned steps to become atomically flat semicircular plateaus atop an atomically flat terrace. (C) Corresponding EFM amplitude detail highlights graphene nanoribbons on $(1\bar{1}0n)$ relative to surrounding substrate. Given the finite size of the conducting probe tip (radius, $\sim$ 20 nm), the width of the graphene nanoribbon is estimated at $\sim$ 40 nm. Wider interconnect-like graphene ribbons at left and right join the nanoribbon device to the larger circuit. Scale bars and color scales (far right) in (A), (B), and (C) are 1 μm, 200 nm, 200 nm, 0-140 nm, 0-87 nm and 3.7-4.4 V, respectively.

nanoribbons are narrow enough to cause significant transverse confinement of electrons. A SiC template for the graphene nanoribbon device is fabricated in two steps. The first step etches a pair of deep trenches (200nm deep) for the growth of graphene leads that connect nanoribbons with metal contacts. The second step etches a shallow trench perpendicular to the first two trenches with just a few nanometers in depth. A pair of graphene nanoribbons will then form along these sidewalls and seamlessly connect to the leads. An example of patterned SiC surface is shown in Figure 26(A). After high temperature annealing in the CCS furnace, the shallow-etched sidewalls will be rounded as a result of the mass flow of the SiC surface (Figure 26(B)&(C)). For some devices, the shallow etching step is skipped since the natural step bunching of SiC is sufficient to provide sidewall templates for graphene nanoribbon growth, an example of a natural step graphene nanoribbon is shown in Figure 33.

The results of graphene growth can be examined with the electrostatic force microscopy (EFM), which highlights the surface areas covered with graphene. Unwanted graphene ribbons near the devices can be removed by the lithographically patterned O_2 plasma etching,

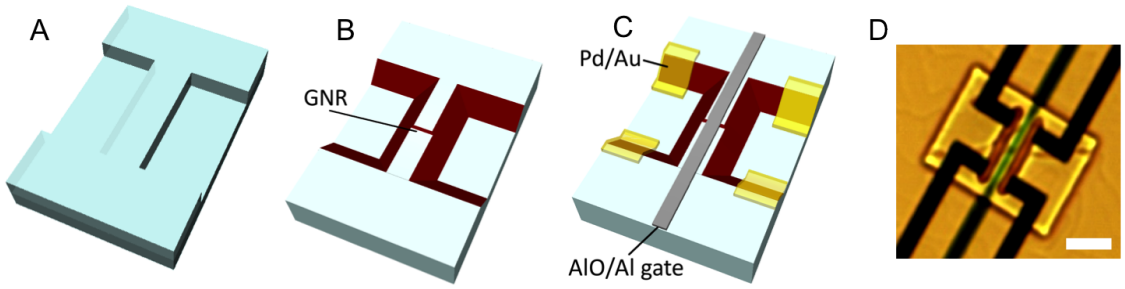

Figure 27: Schematics of device preparation. (A) Deep trenches are patterned in SiC (0001) for contacts leads. (B) After graphitization both the graphene nanoribbon (GNR) and wide graphene strips form preferentially on faceted SiC. (C) The completed device after deposition of gates (Al_2O_3 topped with Al) and Pd/Au contacts. (D) Optical image of a real device. Contacts appear in black, central gate green. Scale bar is $4\mu m$.

which uses the EFM image as the reference(Figure 28(B)). It is worth to note that this etching step only affects unwanted graphene and the target graphene nanoribbon is intact and never exposed to any form of etching since this nanoribbon is protected by the etching mask.

After the O_2 plasma etching, 20nm palladium and 40nm gold are deposited and lift-off on graphene that produces low resistance Ohmic with the graphene leads on the deep-etched sidewalls. In some devices, a local top gate is fabricated before the metal contact fabrication. This gate is comprised of 20nm aluminum oxide, which serves as the dielectric, and 40nm aluminum, which serves as the gate electrode. The deposition of the aluminum oxide and aluminum uses the slow-evaporation technique discussed in Chapter II. The entire fabrication process is illustrated in Figure 27.

4.2.2 Gate capacitance calibration

The local top gate tunes the carrier density in the graphene nanoribbon by forming a capacitor between the nanoribbon and the gate electrode. The gate capacitance is calibrated using a Hall bar made of monolayer graphene and covered with a local gate. The Hall bar was used to measure the carrier density in graphene at different gate voltages. The normal Hall bar measurement uses the time-consuming magnetic sweeps. An alternative solution which is used in this thesis sweeps the gate voltage V_g at different magnetic fields (B). The Hall voltage V_H as a function of gate voltage is recorded at $\pm$B, and the Hall coefficient can

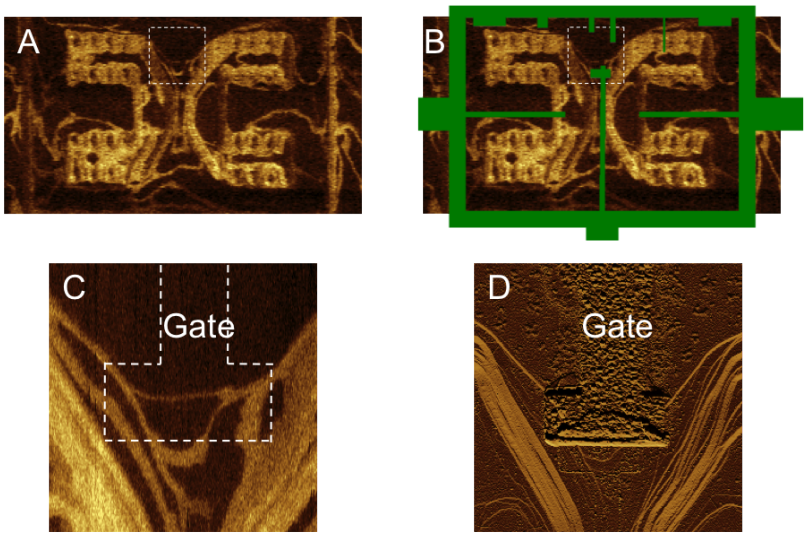

Figure 28: Etching of the graphene ribbons bridging the contact. (A) EFM image of the whole device showing the four wide contact strips and multiple bridging ribbons. The light color is graphene on the SiC substrate. (A) Patterned area for O_2 plasma etching: the green area is etched away. (C) Zoomed EFM image of the dotted square in (A) showing the selected ribbon and location of the gate. (D) AFM image of the same area as (C) after etching and gate deposition.

be calculated from $V_H(V_G, B)$ as

$$R_H(V_g) = \frac{V_H(V_g, B) - V_H(V_g, -B)}{2IB}, \tag{26}$$

in which I is the current in the Hall bar. As $R_H/B = 1/ne$[37], in which e is the charge of a electron, the relation between the carrier density n and the gate voltage can be measured(Figure 29). The gate capacitance is estimated using the slope of $n - V_g$ curve and is estimated to be $0.97 \times 10^{12} cm^{-2}/V$ at low temperature. The dielectric constant of the deposited aluminum oxide can be calculated using the parallel capacitor model $C/A = \epsilon\epsilon_0/d$, in which ϵ is the dielectric constant, C/d is the gate capacitance, and d is the dielectric thickness. The estimated ϵ is about 3 at low temperature and 7 at room temperature. The origin of change of dielectric constant is to be explored.

4.2.3 Ribbon width estimation using EFM

The sidewall graphene ribbons cannot be directly observed in topography imaging tools such as AFM and SEM as the topography feature of the graphene ribbon overlaps with that of the SiC sidewall. In contrast, EFM can still image graphene by measuring the

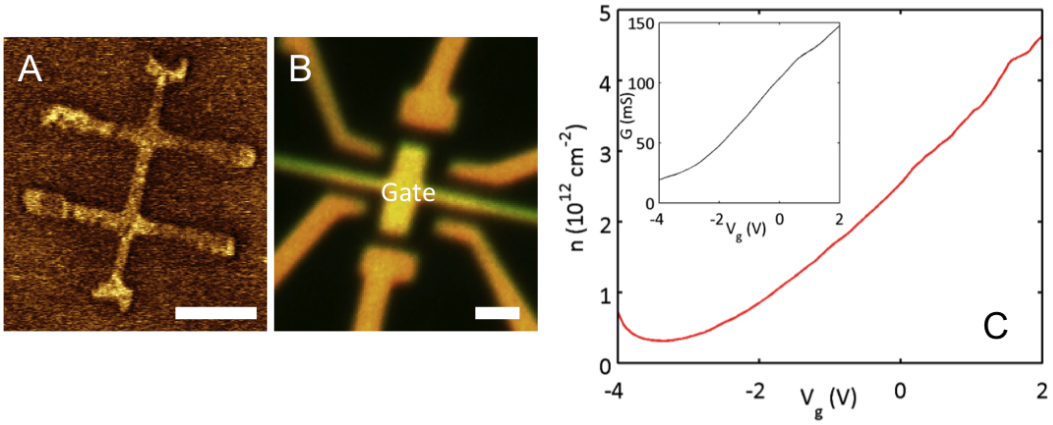

Figure 29: Gate calibration. (A) EFM image of a single layer graphene Hall bar on SiC (0001) face. (B) Optical image for the same Hall bar after gate and contacts were added. Scale bar is $2\mu m$. (C) Carrier density n as a function of gate voltage from Hall measurements (the charge carriers are actually electrons). In the linear region, $n = 0.95 \times 10^{12} cm{-}2/V$. The curve flattens out near the Dirac point (mixed n-p carriers). Inset: Four-point conductance as a function of gate voltage. The Gate to Source resistance is a few $G\Omega/\mu m^2$.

surface potential difference. The resolution of EFM is limited by the dimension of the EFM tip, which is typically about 30nm. This resolution starts to show its limit during the width measurement of graphene nanoribbons. The measured width stops scaling with the real width of a ribbon when the width becomes less than the tip radius. However, this limit can be overcame by modeling the electrostatic force between the tip and the surface. The EFM profile across an abrupt border between two areas with different surface potential is described as[115]

$$F(x - x_0) \propto C - \left(1 + \frac{2Rd}{(x - x_0)^2}\right)^{-1/2}, \tag{27}$$

in which R is the radius of the tip, d is the tip sample distance, x_0 is the position of the border, x is the position of the tip, and C is a constant. The term Rd can be estimated by comparing this equation with experimental measured profile (Figure 30(D)). The Rd value that gives the best fit with the experimental data is $Rd = 264.5nm^2$. As $d = 12.5nm$ is a parameter set by the user of the equipment, the tip radius is estimated to be $21.2nm$.

To applied the estimated tip radius to ribbon width measurements, the Equation (27)

has to be converted into a format appropriate for ribbons. A nanoribbon is a narrow domain sandwiched between two large domains. Therefore, a nanoribbon can be viewed as two domain boundaries separated by the distance equals the width of the ribbon. As the electrostatic force between the tip and a surface is linearly proportional to the surface potential, the superposition principle can be used. The EFM profile of a graphene nanoribbon can be derived from subtracting the EFM profile for two domains with the same profile shifted by Δx, which equals the width of the ribbon. Thus the ribbon profile can be expressed as

$$F_{ribbon}(\Delta x) = F(x - x_0) - F(x - x_0 - \Delta x). \tag{28}$$

This subtraction process is illustrated in Figure 30(C) and the EFM profile of a nanoribbon calculated using equation (28) is plotted in Figure 30(E). Both the height (H_{EFM}) and the full width at half maximum (W_{EFM}) of the profile increase with increasing Δx. H_{EFM} and W_{EFM} vs. Δx is plotted in Figure 30(F). According to Figure 30(F), W_{EFM} gives a good estimation of the ribbons width when the ribbon width is much larger than the tip radius. However, when the ribbon width approaches the tip radius or becomes even less, the W_{EFM} no longer scales with the ribbon width and eventually saturates. Meanwhile, H_{EFM} becomes a better indicator of the ribbon width, decreasing almost linearly with the reduction of the ribbon width all the way to zero. This is trend in simulation is confirmed by the EFM image in Figure 30(B). The EFM amplitude at the nanoribbon is only 1/3 to 1/2 of the amplitude at wide graphene region. Using the relation between H_{EFM} and Δx, the narrowest part of this ribbon is estimated to be 15nm.

4.3 Material characterization

4.3.1 Raman spectroscopy

As one of the least ambiguous techniques to determine graphene, Raman spectroscopy is used to detect graphene sidewall nanoribbons. A typical spectrum of a graphene nanoribbon grown on bunched SiC step edges is plotted in Figure 31. This spectrum is obtained by subtracting the SiC spectrum from the raw data. In this spectrum, all three major peaks of graphene are present, locating at 1368.4 cm^{-1}, 1607.8 cm^{-1}, and 2733.1 cm^{-1} for the peak

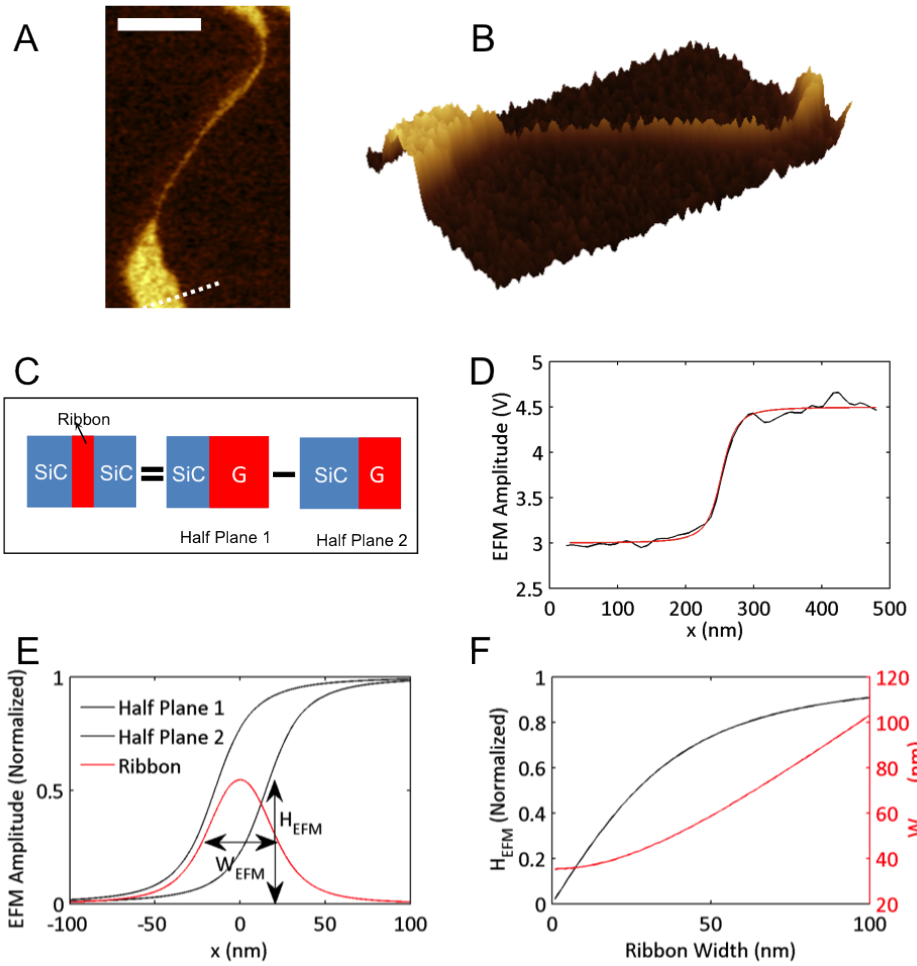

Figure 30: Ribbon width measurement with EFM. (A) and (B) EFM image of a graphene nanoribbon displayed in 3D and 2D color mapping. The EFM amplitude is notably reduced on the narrow ribbon (B). The narrowest part of this ribbon was estimated to be 15nm. Scale bar 500nm. (C) Schematics of the two half planes used to model the apparent width and height of the EFM signal across a narrow ribbon. (D) Black line: Measured EFM amplitude profile of an abrupt surface potential change from graphene to substrate on a flat region (dotted line in (A)). Red line: Fit to Eq. (28). The tip radius was estimated to be 21.2nm. (E) The two half plane EFM amplitude (black lines) and the resulting EFM trace across the ribbon (red). (F) Calculated EFM amplitude and EFM width vs. ribbon width based on the modeled double step in (E) (tip radius=21.2nm). Scale bar: 500nm.

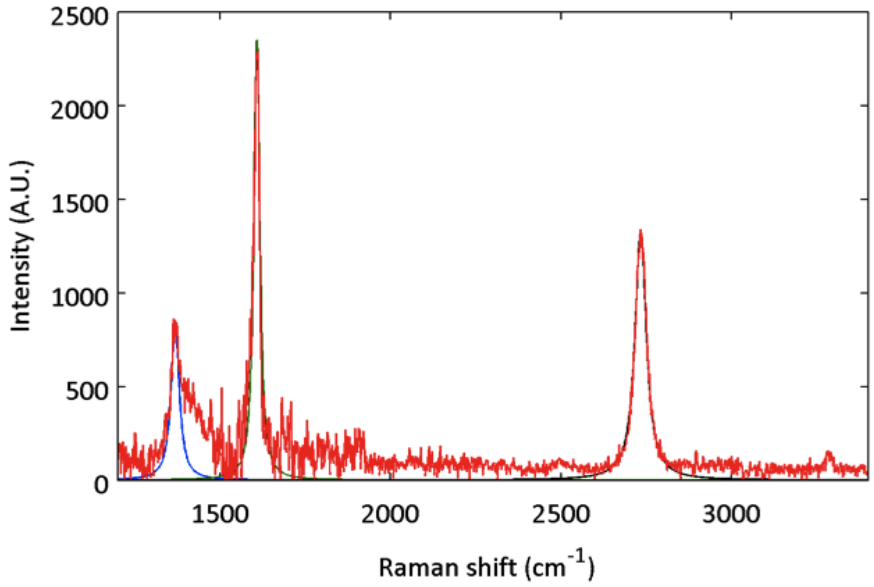

Figure 31: A typical Raman spectrum of a graphene nanoribbon. All three peaks can be fitted with a single Lorentizian as shown in blue, green, and black. The fitted peak positions for the D, G, 2D peaks are 1368.4, 1607.8, and 2733.1cm^{-1}, and the peak FWHMs are 28.3, 19.8 and 39.6cm^{-1}, respectively.

D, G, and 2D respectively. The 2D peak can be fitted to a single Lorentizan with the FWHM equals 39.6 cm^{-1}, suggesting a monolayer graphene[69][116]. The relative strong D peak does not necessarily indicates lattice defects in the nanoribbon. Instead, it is attributed to the graphene edge since edges breaks the translational symmetry of 2-D graphene lattice thereby allowing the transition responsible for the D peak[69]. The position of three peaks are similar to their position for Si-face graphene, which is usually n-doped[96] and contains strain[116].

4.3.2 I-V spectroscopy

The resistance distribution along a graphene nanoribbon can be directly observed by I-V spectroscopy, which has been introduced in Chapter III. The conducting AFM tip is in direct contact with the graphene nanoribbon to measure the resistance between the tip and the graphene drain contact. The resistance distribution is measured by taking a series of current-voltage response curves (I-V) along the nanoribbon. For metallic ribbon, the I-V curves are linear and the slope of the curves represents the measured resistance. Figure

32(A) illustrates the setup of this measurement and an example of I-Vs curve is shown in Figure 32(B). The current meter in Figure 32(A) is included as part of the AFM system, the voltage sweep is controlled by the software and the ribbon is connected to a clean ground through the contact that is not used in the I-V sweep that reduces the measurement noise. In a resistance(conductance) map, the I-V spectra are taken at each location in the mapping matrix and converted to resistance (conductance). A high resolution mapping usually takes an entire day.

The conductance map and the EFM image of a graphene nanoribbon is shown in Figure 32(C). All measurements are done in air at room temperature. The drain contact is on the left hand side, not included in the plot. The surface area with graphene nanoribbon shows significant conductance while the rest of the surface is insulating. The general trend of the conductance along ribbon can be seen in the three-dimensional plot. The total resistance measured in a I-V spectrum can be split into four terms:

$$R_{total} = R_{ribbon} + R_{tipC} + R_{dg} + R_{circuit}. \tag{29}$$

The ribbon resistance R_{ribbon} is the targeted term and has to change monotonically along the nanoribbon. The last two terms includes the drain-graphene contact resistance (R_{dg}) and other resistance ($R_{circuit}$) included in the circuit. Both terms are constant during an I-V spectra mapping. The only term can add fluctuation in the total the resistance is the tip-ribbon contact resistance (R_{tipC}). This resistance is very sensitive to the surface topography and contact area. One way to reduce the effect of this contact resistance is to select the minimum resistance in every cross section of in the resistance map and the minimum resistance to represent the ribbon resistance the longitudinal location. Figure 32(B) is plotted in this way. Each data point is the minimum resistance among the resistance value taken at the same x. The resistance change between $0.1 < x < 0.7\mu m$ is $5k\Omega$, corresponding to a square resistance $\sim 0.5k\Omega$. This result suggest that the sidewall graphene nanoribbons are very conductive even at room temperature.

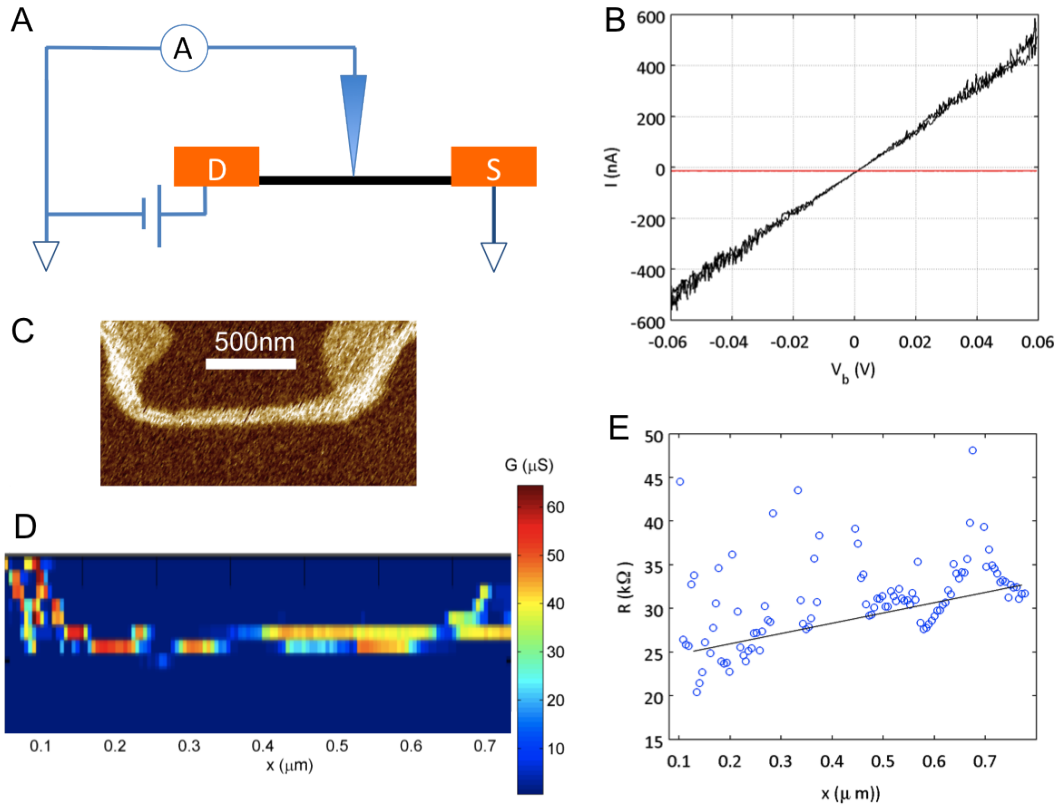

Figure 32: (A) An illustration of the operation principle of I-V spectrocopy. For a nanoribbon sample, the current flows from the AFM tip into the ribbon and collected in the drain contact ("D"). (B). Comparison of the I-Vs collected on graphene (black) and on the SiC surface (red). It is worth to note that the current at zero bias voltage is not zero for both case. (C) Conductance mapping of a graphene nanoribbon converted from I-V spectroscopy mapping. The drain contact is on the left hand side of the image. (D) The minimum resistance at each longitudinal position converted from the same I-V spectroscopy mapping data as in (C).

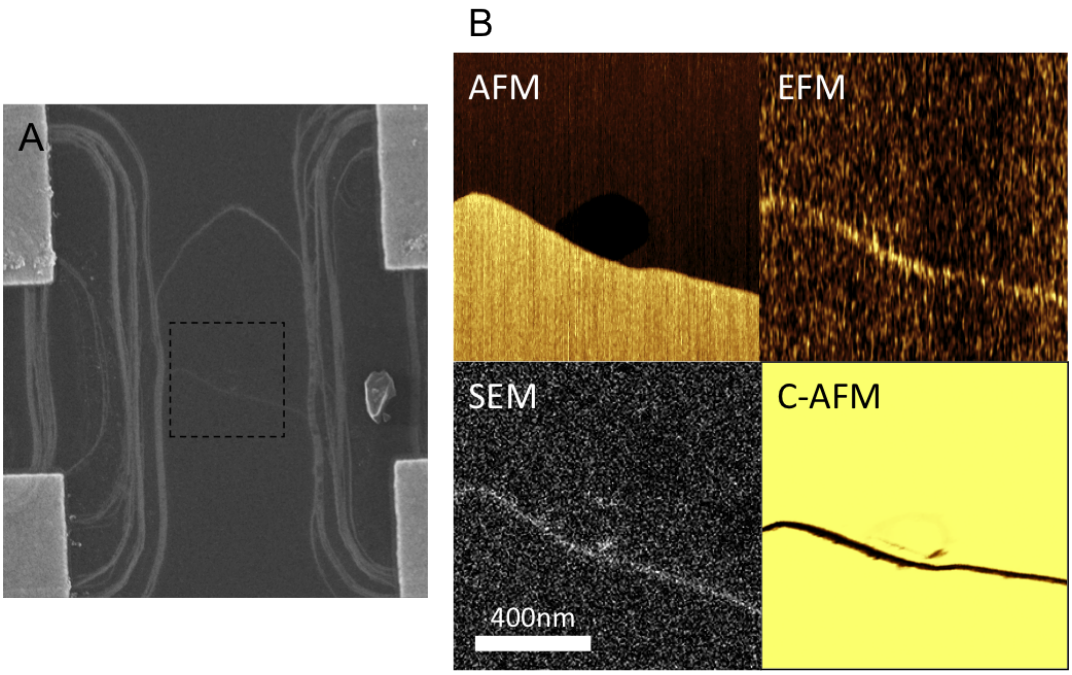

Figure 33: Ribbon grown on the sidewall of a SiC step (conducting 6H-SiC substrate). The SiC step results from a natural step flow during high temperature annealing for graphitization (A) SEM image of a device after contact patterning, featuring two ribbons bridging the graphene contact strips. The ribbon inside the dashed square is imaged with different techniques in (B). (B) Imaging of a single nanoribbon at the same scale with AFM (the SiC step height is 3.3 nm), EFM (the bright contrast indicates a change in the surface potential), SEM (acceleration voltage 30kV) and conductive AFM (the dark contrast indicates more conducting area).

4.3.3 Comparison of microscopy tools on sidewall nanoribbons

Many imaging tools are used in this thesis to directly observe graphene nanoribbons. Figure 33 includes images of a sidewall graphene nanoribbon device taken with SEM, AFM, EFM, and C-AFM. SEM and AFM only shows contrast for topography change while EFM and C-AFM can accurately locate the graphene nanoribbon.

4.4 Transport measurement

4.4.1 Results

Figure 34 shows results for sample S1 which is a $W = 27nm$ wide, $L = 370nm$ long sidewall ribbon that is seamlessly connected to graphene leads.Two metal contacts are applied to the graphene contacts on each side of the leads to facilitate 4-point transport measurements.

Figure 34 also shows transport properties of sample S1 that are typical for all of the ribbons measured. A weak temperature dependent zero-bias anomaly (ZBA) [117] is observed for $T < 100K$, (Figure 34(D)) and the resistance increases by less than 10% from 100 K to 300 K for all of the ribbons. The observed asymmetry in ZBA may reflect the geometrical asymmetry (note that the leads and the ribbon are both n-doped due to the graphene-substrate interface, see below). The magneto-conductance shows a minimum at $B = 0$. The width, amplitude, and temperature dependence of this weak localization feature, as well as the zero-bias anomaly, is similar to that observed in carbon nanotubes [118]. It is convenient to express the conductance g of these nanoribbons in units of $G_0 = \frac{1}{2}R_0 = \frac{e^2}{h} \sim (25.8k\Omega)^{-1}$, consequently $g = 1/R = 0.65G_0$.

For a diffusive graphene ribbon of width W and length L, the conductance g and conductivity G are related by $G = gL/W$. For example, L/W for ribbon S1 is 37 so that its conductivity (assuming diffusive transport) is $G_{rib} = 37 \times 0.65G_0 = 25G_0$. It is known that epitaxial graphene ribbons are charged due to the interface and that the charge density $n \simeq -4 \times 10^{12} cm^{-2}$ ([18], [99]). Assuming diffusive transport [119] $G = ne\mu$, so that the mobility $\mu \simeq 1600 cm^2 V^{-1} s{-}1$, which is comparable to two-dimensional Si-face epitaxial graphene on SiC([18], [44]) and exfoliated graphene on SiO_2 [41]. These measured parameters are typical for sidewall ribbons produced in this study.

Deeper insight is gained by applying a top gate to the sidewall ribbon [92]. The top gate consists of an aluminum oxide layer ($20nm$) on top of which the aluminum layer is deposited. Therefore the graphene charge density n under the gate can be continuously adjusted from p to n^* by applying a gate potential V_g, $n = -0.7 \times 10^{12}\ V_g\ cm^{-2}/V$ according to the dielectric constant of aluminum oxide at low temperature measured in section 4.2.2. The ungated portions of the structure are n doped ([18], [99]) (Environmental doping can significantly alter the charge density of unprotected graphene [34]).

Sample S2 (Figure 35) also consists of a graphene ribbon ($L = 1.6\mu m$, $W = 39nm$) connected to wide graphene leads. The top gate covers half of the ribbon and part of one lead, to produce effectively a single junction on the graphene ribbon (i.e. either np

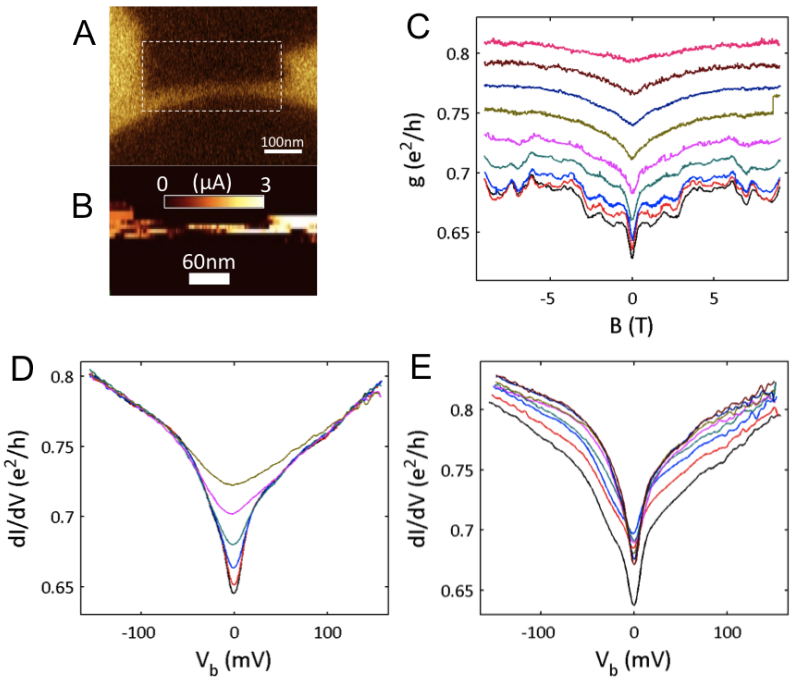

Figure 34: Sample S1: ungated 27 nm × 0.37 μm sidewall ribbon with wide leads. (A) EFM image showing graphene ribbon and leads. (B) I-V spectroscopy of the area outlined in (A) mapping the current intensity from the AFM tip through the ribbon to the grounded right lead. (C) Conductance versus magnetic field at T = 4, 7, 12, 20, 35, 55, 80, 120, 180K (bottom to top) showing weak localization and conductance fluctuation features. (D) Four point ribbon conductance versus bias voltage at T = 4, 7, 12, 20, 35, 55K showing pronounced positive-negative asymmetry and convergence of the curves at high bias. (E) Conductance versus bias voltage at T = 4K for various magnetic fields (B = 0, 1, 2, 3, 4, 5, 6, 7T), showing a slight magnetic field effect.

or nn^*). Two metal contacts are attached to each of the graphene leads to facilitate 4-point transport measurements (Figure 35(D)). The magnetic field response (Figure 35(E)) and the ZBA (Figure 35(B)) are essentially similar to those observed for the simple ribbon (Figure 34). The response to the gate is asymmetric. For a negative gate voltage $-3V < Vg < 0$ corresponding to a charge density change on the ribbon $D_n \simeq 2.1 \times 10^{12}/cm^2$, the conductance varies by (only) 15%. However, when a positive gate voltage is applied, $0 < Vg < +3V$, the conductance increases by ∼50%. The minimum conductance is $g_{min} \simeq 1G_0$, consequently the minimum conductivity (defined by $G_{min} = g_{min}L/W$) $G_{min} > 25G_0$. This is much greater than predicted or observed for diffusive neutral 2D graphene ([41], [120]). The differential conductance (dI/dV) versus V_g and V_b (Figure 34(C)) shows diagonal features that scale with $V_g/V_b = 1.4$. Coulomb blockade diamond features observed at low tempearture by others ([52],[107],[108],[6],[121]), are not seen in these ribbons.

Sample S3 (Figure 36) is another ribbon ($L = 1.06\mu m$, $W = 35nm$) where unlike S2, only the central part is covered by the top gate. This geometry produces a device with 2 junctions that can be npn or nn^*n biased. Its response is similar to that observed in the single junction device (Figure 35). Figure 36(E) shows the conductance g (V_g) of S3 as a function of the gate voltage for temperatures ranging from 4 K to 55 K. For all temperatures, g ($V_g < 0$) is essentially constant ($g \sim 0.3G_0; D_g \simeq 15\%$). For $V_g > 0$, it increases to $g \sim 0.6G_0$ for $V_g = 2V$ ($n = -1.4 \times 10^{12}/cm^2$). Note that superimposed conductance oscillations are observed at low temperatures. The conductance remains relatively large for all gate voltages and temperatures. Both the magnetic field response (Figure 36(D)) and the ZBA (Figure 36(B)) are similar to the simple ribbon (Figure 34) and the single junction device (Figure 35). The features of dg/dV_g (plotted as a function of B and V_g) are essentially independent of magnetic field. The diagonal features in the differential conductance (dI/dV) versus V_g and V_b (Figure 36(C)) scale with $V_g/V_b = 0.9$; no Coulomb blockade diamonds ([52],[107],[108], [6],[121]) are observed.

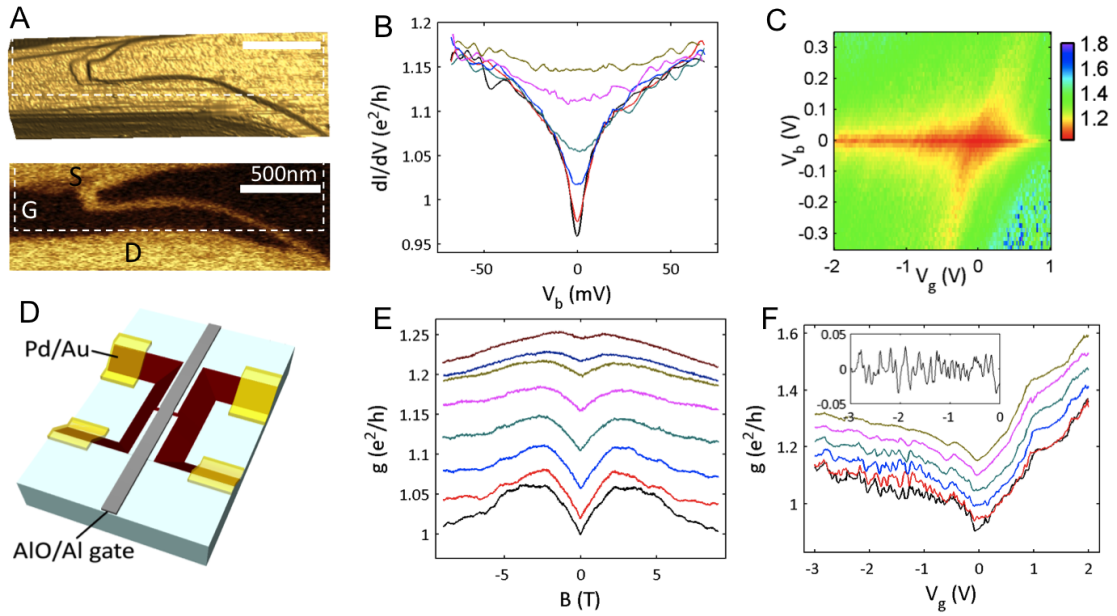

Figure 35: Sample S2: gated single junction sidewall ribbon with source (S), drain (D) and gate (G). (A) AFM topography (top) and EFM (bottom) images showing the graphene ribbon; dashed white line shows the outline of the Al gate (20 nm thick Al_2O_3 dielectric) that covers about 70% of the ribbon and the source lead. (B) Differential conductance versus bias voltage at T = 4, 7, 12, 20, 35, 55 K. (C) Differential conductance (color scale in units of G_0) versus V_b and V_g at T = 4 K. The conductance minimum position increases with increasing V_g: $dVb/dV_g \simeq 1.4$. (D) Schematic diagram of gated sidewall ribbons. (E) Conductance versus magnetic field ($V_g = 0$) for T = 4, 7, 12, 20, 35, 55, 80, 120 K (bottom to top) showing a broad weak localization dip. (F) Conductance versus gate voltage at T = 4, 7, 12, 20, 35, 55 K showing typical ballistic channel Klein tunneling features. The minimum conductance is about 1 G_0. The Vg induced conductance fluctuations are much larger than in (E). Inset: conductance oscillations (in units of G_0) at 4K after background subtraction.

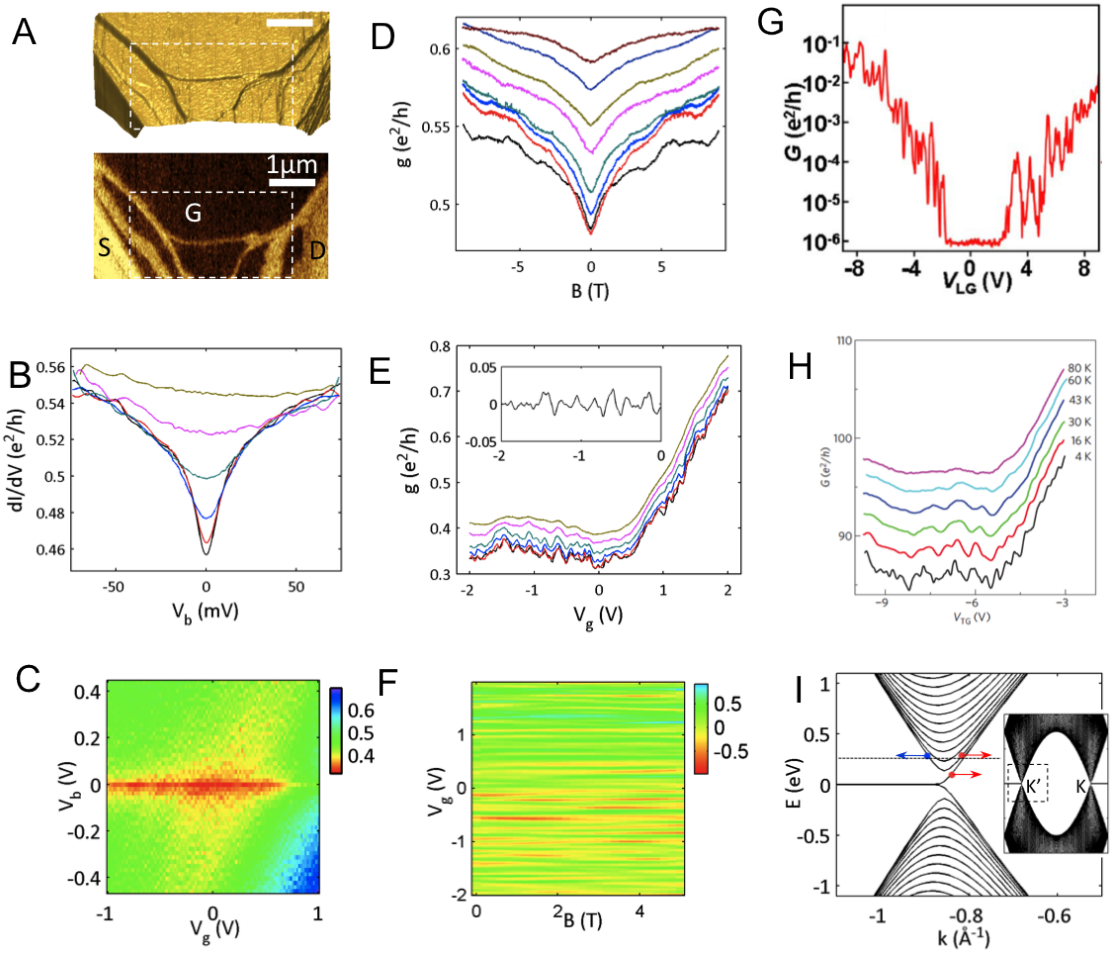

Figure 36: Sample S3: gated double junction sidewall ribbon. (A) AFM topography (top) and EFM (bottom) images; dashed white line shows outline of the Al gate (20 nm thick Al_2O_3 dielectric) that covers the central part of the ribbon. The downward extending branches have been lithographically cut, confining transport to the upper ribbon. (B) Differential conductance versus bias voltage at T = 4, 7, 12, 20, 35, 55 K. (C) Differential conductance (color scale in units of G_0) versus V_b and V_g at T = 4 K. (D) Conductance versus magnetic field at T = 4, 7, 12, 20, 35, 55, 80, 120 K. (E) Conductance versus gate voltage for T = 4, 7, 12, 20, 35, 55 K. (F) dg/dV_g (color scale, in units of G_0/V) versus gate voltage and magnetic field. (G) Conductance versus back gate voltage for an exfoliated graphene ribbon ($L = 100nm$, $W = 30nm$) from Ref. [6]. The large conductance change and the conductance fluctuations result primarily from Coulomb blockade effects. (H) Conductance versus gate voltage for a wide ribbon ($\sim 10\mu m$) with a narrow channel ($40nm$) for T = 4, 16, 30, 43, 60, 80 K, from Ref. [7] showing the Klein tunneling effect. Note the qualitative resemblance with Fig. 3e. (I) (Inset) Tight binding band structure of a $21nm$ zigzag ribbon. Main panel, detail near the K point showing the unique edge state and the subbands (after Ref. wakabayashi2007), blue: left moving, red: right moving. The dashed line corresponds to the Fermi energy at a charge density of $-4 \times 10^{12} cm^{-2}$.

4.4.2 Analysis

The response of these graphene ribbons can be contrasted to transport measurements on back-gated exfoliated graphene, where the typical device consists of a lithographically patterned, exfoliated wide graphene Hall bar on an oxidized silicon wafer ([41], [42]). Back-gating allows the charge density n of the entire graphene structure to be uniformly adjusted by applying a potential V_{bg} to the gate (there are no junctions). Consequently, in these 2D diffusive graphene Hall bars the conductivity follows the channel charge density: $G = ne\mu$, resulting in a characteristic symmetric V shaped ambipolar response $G(V_{bg})$ with respect to the charge neutrality point [41].

Very narrow, conventionally patterned back-gated exfoliated graphene ribbons have a related ambipolar response ([52], [107], [48], [6], and [121]). However, at low temperatures, their minimum conductivities are greatly suppressed (by as much as a factor of 10^{-4}) compared to wide ribbons. As for wide ribbons, transport in narrow exfoliated ribbons is diffusive but scattering at the edges so severely reduces the scattering length that strong localization effects are observed. This is revealed by the coupled quantum dot Coulomb blockade signature, which is significantly, if not primarily, responsible for the large conductance decrease near charge neutrality ([107], [6], and [121]). Specifically, the on-state conductance of these 30 nm wide 100 nm long lithographically patterned (exfoliated graphene) ribbons are of the order of $g_{on} \sim 0.1G_0$, while the off-state minimum conductance (at the charge neutrality point) is about $g_{off} \sim 10^{-5}G_0$ so that $g_{on}/g_{off} \simeq 10^4$ [6] . In contrast, for our ribbons $g_{on}/g_{off} < 2$. This ratio is even much less than that observed in 2D diffusive graphene where $g_{on}/g_{off} > 10$ for comparable charge densities.

Assuming diffusive transport, the minimum conductivities $G_{off} = g_{off}L/W$ for this micrometer long ribbons are an order magnitude greater than for the exfoliated narrow graphene ribbons mentioned above, and at the same time much greater than the theoretical minimum conductivity of 2D graphene in the diffusive regime [120] (i.e. $4G_0/\pi$). This observation suggests that these ribbons are ballistic conductors (as verified below) and confirms that our graphene ribbons are metallic and not semiconducting.

The gating response of sample S2 and S3 (Figure 35(F), Figure 36(E)) is clearly very

different than for patterned exfoliated 100 nm and long and 30 nm wide ribbons (Figure 35(G)). On the other hand, the gating response (apart from an overall scale factor) is qualitatively strikingly similar to that observed by Young et al. [7] (Figure 35(H)) for very short, wide channels ($L = 40nm$; $W = 10,000nm$). Even the oscillations have a similar appearance. Transport in these wide, gated ribbons is well-understood ([7], [122]). There, the conductance is dominated by the transmission at the charge density junctions produced by the gate. For npn junctions normally incident charge carriers are perfectly transmitted through the np/pn junctions as a manifestation of Klein tunneling ([7], [122],[114]): a right-moving electron normally incident on the np junction, will be converted to a left-moving hole at the junction and the inverse conversion occurs at the pn junction. If furthermore transport in the channel is ballistic, then normally incident electrons will be perfectly transmitted through the structure. Transmission at non-normal incidence is exponentially suppressed (see below). As a result the conductance is essentially constant in the npn junction, independent of the charge density (i.e. independent of V_g for $Vg < 0$) [108]. For nn^*n junctions the reflection of non-normal incident electrons is only partial and the conductance depends on V_g, explaining the observed npn/nn^*n asymmetry. The observed, small conductance oscillations result from Fabry-Perrot interference [7]. Since the described effect requires ballistic transport in the channel region, it is very surprising to see it in a long narrow graphene ribbon, and not only indicates that our graphene ribbons are ballistic conductors but in addition that there is no energy gap: i.e., they are metallic.

Quantitatively, the transmission probability $T(k_y)$ through a pn (or np) graphene junction (assuming ballistic transport) is shown in Equation 25. Therefore the conductance g through an npn structure (for metallic zig-zag ribbons ([113]), see below) is [122]

$$g = 2G_0 \sum_{m_y=-m_y^{max}}^{m_y=m_y^{max}} \exp - \left(\frac{2\sqrt{\pi} d_j (2\pi m_y/W)^2}{\sqrt{n_1} + \sqrt{n_2}} \right) \tag{30}$$

where d_j is the width of the junction assuming a constant electric field E_J, n_1, and n_2 are the charge densities on either side of the two junctions, W is the width of the ribbon and m_y is the subband index. Because of exponential suppression (Equation 30) under npn bias only the $m_y = 0$ subband transmits through the np-junctions in narrow ribbons for which

the inter-subband energy gaps are significant. If transport of the $m_y = 0$ channel is ballistic through the ribbon, then the junctions determine the device conductance which in the ideal case is $g = 2G_0$. In the forward biased nn^*n case the $m_y \neq 0$ channels are not suppressed. The conductance is expected to increase with increasing V_g as observed both here and in other devices [7].

However, because the conductance increases only slightly under nn^*n bias, it is clear that even then transport is dominated by the $m_y = 0$ channel. The characteristic subband spacing in graphene ribbons is on the order of $D_E \sim 1eV/W$, where W is the width in nanometers ([18], [104]). Assuming ballistic conductance in the ribbon and that the charge density in the leads $n \sim -4 \times 10^{12} cm^{-2}$ (see above), then the conductance for a $23nm$ wide ballistic ribbon should saturate at $g \sim 10G_0$ in the nn^*n case. In contrast, only a relatively small conductance increase is observed when the ribbon is negatively biased (Figure 35(F) and 36(E)). We conclude that in our ribbons the mean free paths of the $m_y \neq 0$ channels are much shorter than for $m_y = 0$ even in the nn^*n case.

The above observation is important since the $m_y = 0$ channel corresponds with the dispersionless channel that is present only in metallic ribbons (Figure 36(I)). In the perfect ballistic case the conductance $g = 2G_0$ ([119], [113], [112]). We observe $g \simeq G_0$, which implies that the transmission coefficient T_{my} for this channel (in the Landauer picture [119]) is $T \simeq 0.5$, which is quite large considering that two (imperfect) junctions and a micron long graphene ribbon channel are involved. These observations indicate that the mean free path of the $m_y = 0$ channel is on the order of microns. This conclusion is confirmed by the slight, and essentially gate voltage independent, conductivity decrease as the temperature is lowered. The nearly temperature independent conductivity also precludes an energy gap and confirms that the ribbon has a metallic subband (the $m_y = 0$ subband, i.e. the edge state). Note that the temperature dependence is strongly suppressed for non-zero bias (see Figure 34(D), 35(B), and 36(B)), indicating that it is related to electron-electron scattering and not electron-phonon scattering.

Summarizing, the experimental data show that transport in micron length sidewall graphene ribbons is dominated by a single metallic subband ($m_y = 0$) with a large mean

free path; the $m_y \neq 0$ subbands in these ribbons have considerably shorter mean free paths. These properties apply over the entire temperature range $(4K - 300K)$ investigated. The observations are in good agreement with predictions of a robust perfectly conducting metallic subband described by Wakabayashi et al. ([113], [112])in graphene ribbons in general (except perfect armchair ribbons). Specifically, they predict that the $m_y = 0$ subband corresponding to the edge state for zigzag-like boundaries is perfectly conducting as long as inter-valley scattering is suppressed. This edge state, that is generally present ([113], [112], [123])(except for armchair ribbons) contributes $2G_0$ to the conductance (not $4G_0$ as for the other subbands), due to its unique structure (36(I)). The other subbands are susceptible to scattering-induced localization, so that for a sufficiently long ribbon only the edge state survives and $g = 2G_0$. Moreover, transport in the edge state is valley polarized: transport is in opposite valleys for opposite directions of current flow and also for opposite carrier polarity (cf Figure 36(I)) ([113], [112], [123]). Within a specific valley (K or K) at a specific energy, all $m_y \neq 0$ subbands have both forward moving and backward moving components (see Figure 36(I)) so that any disorder can backscatter charge carriers in those subbands. In contrast, inter-valley scattering (K to K) is required by backscatter charge carriers in the $m_y = 0$ subband, and this requires atomic scale roughness ([113], [112], [123]).

The analogy with carbon nanotubes is striking. A singular perfectly conducting channel has also been predicted [124] for metallic carbon nanotubes with $G = 4e^2/h$ and has been observed experimentally both in single wall [105] and multi-wall [106] carbon nanotubes (for nanotubes, as for graphene ribbons here, the overall transmission is reduced by a factor of about 2). In analogy with that work we refer to our graphene ribbons as ballistic rather than perfectly conducting as suggested in Refs. ([113], [124]).

Ballistic transport has not been observed in graphene nanoribbons patterned on exfoliated graphene flakes due to strong localization effects caused by atomic scale edge roughness ([52], [107], [48], [6], [121]). It is likely that the edge passivation (i.e. termination in the silicon carbide [125]) of the annealed graphene ribbons in this study inhibits the opening of a band gap (predicted [126] and observed in some studies ([127], [128])). Furthermore, because the ribbons are annealed at high temperatures the edges are expected to

be atomically smooth. This explains why the ribbons exhibit the predicted robust metallic subbands ([113], [112], [123]). It is further relevant that even conventionally patterned epitaxial graphene ribbons also have greater mobilities than exfoliated graphene ribbons [99] probably because of their superior interface with the substrate. We also suspect that the substrate adhesion of transferred graphene is not uniform and therefore particularly problematic for nanolithographically patterned structures by adding to the edge disorder.

The small conductance fluctuations (Figure 36(E)) of the order of $D_R \simeq 1kW$ ($D_g \simeq 0.02G_0$) are reminiscent of those observed in ballistic short channels where they are related to Fabry-Perrot fringes mediated by the junctions [7]. The oscillations here are probably related to the opening of subbands in the ribbons as predicted in [112]. The energy levels in a ribbon of width W are approximately given by [19]:

$$E_{m_y} \simeq \left((m_y \pi \hbar v_F/W)^4 + (2m_y eBv^2\hbar)^2)\right)^{1/4}, \tag{31}$$

where v_F is the Fermi velocity ($v_F \simeq 1.1\times10^6 m/s$) and m_y is the subband index. For ribbons with $W < 50nm$ and $|E_F| < 0.5eV$ the first term dominates and $E_m(B)$ is essentially insensitive to B for $|B| < 5T$. This explains why the fine structure features in Figure 36(F) do not obviously disperse with B (in contrast to Ref. [7]). It is relevant that these oscillations must be related to the junctions and not to the lead-to-ribbon contacts, because the oscillations are sensitive to the gate potential. Also note that the knee in $g(V_g)$ is expected to correspond with the charge neutrality point. This occurs in sample S3 at $V_g = 0.5V$ and corresponds to an induced charge density of $n \simeq -0.35 \times 10^12/cm^2$. This residual p-doping compensates the interface doping due to the gate dielectric as is often observed and is consistent with the observation that the fine structure pattern has an approximate symmetry about that point (Figure 36(E)).

Magnetic field induced conductance fluctuations d_g are remarkably small ($d_g \simeq 0.005G_0$ at $4K$). On the other hand, a broad ($D_B \simeq 5T$) and relatively larger ($D_g < 0.03G_0$), temperature dependent weak localization-like feature with $D_B \simeq 1T$ is observed (Figure 34(C), 35(E), 36(D)). It is reminiscent of the related weak localization peak observed in carbon nanotubes [118]. As for nanotubes, the significant width may result from the flux

cancellation effects in narrow structures [119].

All of the samples studied exhibit a temperature dependent zero bias anomaly [117] with an amplitude of about 15% of the high bias conductance and a full width of about $15 - 20mV$ (Figure 36(B)). A log-log plot $g(V_b)$ shows that the curves obtained at various temperatures converge to a line with a slope $a = 0.05$ independent of magnetic field (for $B < 6T$) or V_g, indicating conductance corrections that are not inconsistent with a power law. The value of a is sample dependent and varies from 0.03 to 0.11 (Figure 34(D), 35(B), and 36(B)). This slope is considerably smaller than observed in carbon nanotubes [117], where it is between 0.2 and 0.6 depending on the contacts. In nanotubes the effect has been related to the Luttinger liquid behavior. Whether an equivalent explanation applies here remains to be seen, but it is expected on general grounds that the ZBA is related to electron-electron interactions.

4.4.3 Conclusion

The experiments described here provide conclusive evidence that thermal annealing of steps on the (0001) face of 4H SiC produces ballistic graphene nanoribbons. The experiments are consistent with predictions of robust ballistic transport in nanoribbons through valley polarized edge states. The single channel edge state is particularly insensitive to the precise ribbon geometry. Therefore, the ribbons can function as leads that are analogous to mono-mode optical fibers. The structured growth methods developed here are readily extended to produce interconnected graphene ribbons of arbitrary width on a wafer scale without post-growth lithography thereby providing a viable platform for saleable graphene nanoelectronics. Furthermore, in analogy with bifurcated carbon nanotubes [129], bifurcated graphene ribbons are expected to function as electronic switches, which will be an important departure from field effect switches possibly facilitating an electronics paradigm based on valley-polarized electrons [123].

CHAPTER V

CONCLUDING REMARKS

Graphene has been an extremely active research field during the past decade. As one of the most important branch, epitaxial graphene has showed its importance in fundamental research and potential for industrial applications. The confinement-control sublimation(CCS) growth technique optimize the epitaxial graphene growth. In this thesis, the Quantum Hall effect was observed on monolayer graphene on both Si- and C-faces. The CCS technique is extended to selectively grow graphene on SiC sidewalls on the Si-terminated face so that the lithography patterned SiC can be used as templates to directly grow graphene patterns, avoiding the lithographically tailoring of graphene in device fabrication, which causes serious damages on the edge of graphene. This templated growth method has great advantages for fabricating nano-scale graphene devices. Experiments in this thesis show that graphene nanoribbons selectively grow on sidewalls are metallic and near ballistic, consistent with the prediction of theories[113].

In future works, epitaxial graphene on Si- and C- surfaces will continue to be great platforms for fundamental research and analog devices fabrication. The crystal quality, grain size, and compatibility to the industry platform is outstanding among varies forms of graphene. Meanwhile, the ballistic sidewall graphene nanoribbon suggests another possibilities for electronic devices based on quantum interference of electron waves. Also, the edge states in graphene nanoribbons might contain unique ferromagnetic properties, which could be important for spintronics[126].

REFERENCES

[1] K. S. Novoselov, A. K. Geim, S. V. Morozov, D. Jiang, Y. Zhang, S. V. Dubonos, I. V. Grigorieva, and A. A. Firsov, "Electric field effect in atomically thin carbon films," *Science*, vol. 306, no. 5696, pp. 666–669, —2004—.

[2] X. Li, W. Cai, J. An, S. Kim, J. Nah, D. Yang, R. Piner, A. Velamakanni, I. Jung, E. Tutuc, S. K. Banerjee, L. Colombo, and R. S. Ruoff, "Large-area synthesis of high-quality and uniform graphene films on copper foils," *Science*, vol. 324, no. 5932, pp. 1312–1314, —2009—.

[3] G. Eda, G. Fanchini, and M. Chhowalla, "Large-area ultrathin films of reduced graphene oxide as a transparent and flexible electronic material," *Nature Nanotechnology*, vol. 3, no. 5, pp. 270–274, —2008—.

[4] F. Ming, *Theoretical studies of the epitaxial growth of graphene.* Ph. D. thesis, —2011—.

[5] G. Seol, Y. Yoon, J. K. Fodor, J. Guo, A. Matsudaira, D. Kienle, G. Liang, G. Klimeck, M. Lundstrom, and A. I. Saeed, "CNTbands," —2006—.

[6] B. Ozyilmaz, P. Jarillo-Herrero, D. Efetov, and P. Kim, "Electronic transport in locally gated graphene nanoconstrictions," *Applied Physics Letters*, vol. 91, no. 19, pp. 192107–3, —2007—.

[7] A. F. Young and P. Kim, "Quantum interference and Klein tunneling in graphene heterojunctions," *Nature Physics*, vol. 5, no. 3, pp. 222–226, —2009—.

[8] P. R. Wallace, "The band theory of graphite," *Physical Review*, vol. 71, no. 9, pp. 622–634, —1947—.

[9] M. Sprinkle, D. Siegel, Y. Hu, J. Hicks, A. Tejeda, A. Taleb-Ibrahimi, P. Le Fevre, F. Bertran, S. Vizzini, H. Enriquez, S. Chiang, P. Soukiassian, C. Berger, W. A. de Heer, A. Lanzara, and E. H. Conrad, "First direct observation of a nearly ideal graphene band structure," *Physical Review Letters*, vol. 103, no. 22, p. 226803, —2009—.

[10] M. I. Katsnelson, K. S. Novoselov, and A. K. Geim, "Chiral tunnelling and the Klein paradox in graphene," *Nature Physics*, vol. 2, no. 9, pp. 620–625, —2006—.

[11] D. K. Efetov and P. Kim, "Controlling electron-phonon interactions in graphene at ultrahigh carrier densities," *Physical Review Letters*, vol. 105, no. 25, p. 256805, —2010—.

[12] J. Gonzalez, F. Guinea, and M. A. H. Vozmediano, "Electron-electron interactions in graphene sheets," *ArXiv*, vol. arXiv:cond-mat/0007337v1, —2000—.

[13] J. J. Lin and J. P. Bird, "Recent experimental studies of electron dephasing in metal and semiconductor mesoscopic structures," *Journal of Physics-Condensed Matter*, vol. 14, no. 18, pp. R501–R596, —2002—.

[14] R. Rosei, M. De Crescenzi, F. Sette, C. Quaresima, A. Savoia, and P. Perfetti, "Structure of graphitic carbon on Ni(111): A surface extended-energy-loss fine-structure study," *Physical Review B*, vol. 28, no. 2, pp. 1161–1164, —1983—.

[15] N. A. Kholin, E. V. Rut'kov, and A. Y. Tontegode, "The nature of the adsorption bond between graphite islands and iridium surface," *Surface Science*, vol. 139, no. 1, pp. 155–172, —1984—.

[16] H. Zi-Pu, D. F. Ogletree, M. A. Van Hove, and G. A. Somorjai, "LEED theory for incommensurate overlayers: Application to graphite on Pt(111)," *Surface Science*, vol. 180, no. 23, pp. 433–459, —1987—.

[17] I. Forbeaux, J. M. Themlin, and J. M. Debever, "Heteroepitaxial graphite on 6H-SiC(0001): Interface formation through conduction-band electronic structure," *Physical Review B*, vol. 58, no. 24, pp. 16396–16406, —1998—.

[18] C. Berger, Z. M. Song, T. B. Li, X. B. Li, A. Y. Ogbazghi, R. Feng, Z. T. Dai, A. N. Marchenkov, E. H. Conrad, P. N. First, and W. A. de Heer, "Ultrathin epitaxial graphite: 2D electron gas properties and a route toward graphene-based nanoelectronics," *Journal of Physical Chemistry B*, vol. 108, no. 52, pp. 19912–19916, —2004—.

[19] C. Berger, Z. Song, X. Li, X. Wu, N. Brown, C. Naud, D. Mayou, T. Li, J. Hass, A. N. Marchenkov, E. H. Conrad, P. N. First, and W. A. de Heer, "Electronic confinement and coherence in patterned epitaxial graphene," *Science*, vol. 312, no. 5777, pp. 1191–1196, —2006—.

[20] W. A. de Heer, C. Berger, M. Ruan, M. Sprinkle, X. Li, Y. Hu, B. Zhang, J. Hankinson, and E. Conrad, "Large area and structured epitaxial graphene produced by confinement controlled sublimation of silicon carbide," *Proceedings of the National Academy of Sciences of the United States of America*, vol. 108, no. 41, pp. 16900–16905, —2011—.

[21] S. Bae, H. Kim, Y. Lee, X. Xu, J.-S. Park, Y. Zheng, J. Balakrishnan, T. Lei, H. Ri Kim, Y. I. Song, Y.-J. Kim, K. S. Kim, B. Ozyilmaz, J.-H. Ahn, B. H. Hong, and S. Iijima, "Roll-to-roll production of 30-inch graphene films for transparent electrodes," *Nature Nanotechnology*, vol. 5, no. 8, pp. 574–578, —2010—.

[22] K. S. Kim, Y. Zhao, H. Jang, S. Y. Lee, J. M. Kim, K. S. Kim, J.-H. Ahn, P. Kim, J.-Y. Choi, and B. H. Hong, "Large-scale pattern growth of graphene films for stretchable transparent electrodes," *Nature*, vol. 457, no. 7230, pp. 706–710, —2009—.

[23] A. Reina, X. Jia, J. Ho, D. Nezich, H. Son, V. Bulovic, M. S. Dresselhaus, and J. Kong, "Large area, few-layer graphene films on arbitrary substrates by chemical vapor deposition," *Nano Letters*, vol. 9, no. 1, pp. 30–35, —2008—.

[24] Z. Sun, Z. Yan, J. Yao, E. Beitler, Y. Zhu, and J. M. Tour, "Growth of graphene from solid carbon sources," *Nature*, vol. 468, no. 7323, pp. 549–552, —2010—.

[25] C. Mattevi, H. Kim, and M. Chhowalla, "A review of chemical vapour deposition of graphene on copper," *Journal of Materials Chemistry*, vol. 21, no. 10, pp. 3324–3334, —2011—.

[26] N. R. Gall, E. V. Rut'kov, and A. Y. Tontegode, "Interaction of silver atoms with iridium and with a two-dimensional graphite film on iridium: Adsorption, desorption, and dissolution," *Physics of the Solid State*, vol. 46, no. 2, pp. 371–377, —2004—.

[27] A. T. N'Diaye, S. Bleikamp, P. J. Feibelman, and T. Michely, "Two-dimensional Ir cluster lattice on a graphene moire on Ir(111)," *Physical Review Letters*, vol. 97, no. 21, p. 215501, —2006—.

[28] S. Marchini, S. Gunther, and J. Wintterlin, "Scanning tunneling microscopy of graphene on Ru(0001)," *Physical Review B*, vol. 76, no. 7, p. 075429, —2007—.

[29] P. Y. Huang, C. S. Ruiz-Vargas, A. M. van der Zande, W. S. Whitney, M. P. Levendorf, J. W. Kevek, S. Garg, J. S. Alden, C. J. Hustedt, Y. Zhu, J. Park, P. L. McEuen, and D. A. Muller, "Grains and grain boundaries in single-layer graphene atomic patchwork quilts," *Nature*, vol. 469, no. 7330, pp. 389–392, —2011—.

[30] S. Stankovich, R. D. Piner, X. Chen, N. Wu, S. T. Nguyen, and R. S. Ruoff, "Stable aqueous dispersions of graphitic nanoplatelets via the reduction of exfoliated graphite oxide in the presence of poly(sodium 4-styrenesulfonate)," *Journal of Materials Chemistry*, vol. 16, no. 2, pp. 155–158, —2006—.

[31] G. Eda, C. Mattevi, H. Yamaguchi, H. Kim, and M. Chhowalla, "Insulator to semimetal transition in graphene oxide," *The Journal of Physical Chemistry C*, vol. 113, no. 35, pp. 15768–15771, —2009—.

[32] A. B. Kaiser, C. Gmez-Navarro, R. S. Sundaram, M. Burghard, and K. Kern, "Electrical conduction mechanism in chemically derived graphene monolayers," *Nano Letters*, vol. 9, no. 5, pp. 1787–1792, —2009—.

[33] A. J. Van Bommel, J. E. Crombeen, and A. Van Tooren, "LEED and Auger electron observations of the SiC(0001) surface," *Surface Science*, vol. 48, no. 2, pp. 463–472, —1975—.

[34] X. Wu, Y. Hu, M. Ruan, N. K. Madiomanana, J. Hankinson, M. Sprinkle, C. Berger, and W. A. de Heer, "Half integer quantum Hall effect in high mobility single layer epitaxial graphene," *Applied Physics Letters*, vol. 95, no. 22, p. 223108, —2009—.

[35] M. Orlita, C. Faugeras, P. Plochocka, P. Neugebauer, G. Martinez, D. K. Maude, A. L. Barra, M. Sprinkle, C. Berger, W. A. de Heer, and M. Potemski, "Approaching the Dirac point in high-mobility multilayer epitaxial graphene," *Physical Review Letters*, vol. 101, no. 26, p. 267601, —2008—.

[36] N. W. Ashcroft and N. Mermin, *Solid State Physics*. Brooks Cole, 1st ed., —1976—.

[37] S. Datta, *Electronic Transport in Mesoscopic Systems*. Cambridge University Press, 1st ed., —1995—.

[38] N. Tombros, C. Jozsa, M. Popinciuc, H. T. Jonkman, and B. J. van Wees, "Electronic spin transport and spin precession in single graphene layers at room temperature," *Nature*, vol. 448, no. 7153, pp. 571–574, —2007—.

[39] L. Landau and I. M. Lifshitz, *Quantum Mechanics Non-Relativistic Theory*, vol. 3. Butterworth-Heinemann, 3rd ed., —1981—.

[40] S. G. Sharapov, V. P. Gusynin, and H. Beck, "Magnetic oscillations in planar systems with the Dirac-like spectrum of quasiparticle excitations," *Physical Review B*, vol. 69, no. 7, p. 075104, —2004—.

[41] K. S. Novoselov, D. Jiang, F. Schedin, T. J. Booth, V. V. Khotkevich, S. V. Morozov, and A. K. Geim, "Two-dimensional atomic crystals," *Proceedings of the National Academy of Sciences of the United States of America*, vol. 102, no. 30, pp. 10451–10453, —2005—.

[42] Y. B. Zhang, Y. W. Tan, H. L. Stormer, and P. Kim, "Experimental observation of the quantum Hall effect and Berry's phase in graphene," *Nature*, vol. 438, no. 7065, pp. 201–204, —2005—.

[43] J. H. Chen, C. Jang, M. Ishigami, S. Xiao, W. G. Cullen, E. D. Williams, and M. S. Fuhrer, "Diffusive charge transport in graphene on SiO_2," *Solid State Communications*, vol. 149, no. 27-28, pp. 1080–1086, —2009—.

[44] Y.-M. Lin, C. Dimitrakopoulos, K. A. Jenkins, D. B. Farmer, H.-Y. Chiu, A. Grill, and Ph. Avouris, "100-Ghz transistors from wafer-scale epitaxial graphene," *Science*, vol. 327, no. 5966, p. 662, —2010—.

[45] S. M. Sze, *Physics of Semiconductor Devices*. Wiley-Interscience, 2nd ed., —1981—.

[46] K. Nakada, M. Fujita, G. Dresselhaus, and M. S. Dresselhaus, "Edge state in graphene ribbons: Nanometer size effect and edge shape dependence," *Physical Review B*, vol. 54, no. 24, pp. 17954–17961, —1996—.

[47] M. Y. Han, B. Ozyilmaz, Y. Zhang, and P. Kim, "Energy band-gap engineering of graphene nanoribbons," *Physical Review Letters*, vol. 98, no. 20, p. 206805, —2007—.

[48] Z. Chen, Y.-M. Lin, M. J. Rooks, and P. Avouris, "Graphene nano-ribbon electronics," *Physica E-Low-Dimensional Systems & Nanostructures*, vol. 40, no. 2, pp. 228–232, —2007—.

[49] J. O. Sofo, A. S. Chaudhari, and G. D. Barber, "Graphane: A two-dimensional hydrocarbon," *Physical Review B*, vol. 75, no. 15, p. 153401, —2007—.

[50] J. A. Yan, L. Xian, and M. Y. Chou, "Structural and electronic properties of oxidized graphene," *Physical Review Letters*, vol. 103, no. 8, p. 086802, —2009—.

[51] J. Jackson, *Classical Electrodynamics*. Wiley, 3rd ed., —1998—.

[52] M. Y. Han, J. C. Brant, and P. Kim, "Electron transport in disordered graphene nanoribbons," *Physical Review Letters*, vol. 104, no. 5, p. 056801, —2010—.

[53] Y. Yang and R. Murali, "Impact of size effect on graphene nanoribbon transport," *IEEE Electron Device Letters*, vol. 31, no. 3, pp. 237–239, —2010—.

[54] L. Jiao, L. Zhang, X. Wang, G. Diankov, and H. Dai, "Narrow graphene nanoribbons from carbon nanotubes," *Nature*, vol. 458, no. 7240, pp. 877–880, —2009—.

[55] L. Jiao, X. Wang, G. Diankov, H. Wang, and H. Dai, "Facile synthesis of high-quality graphene nanoribbons," *Nature Nanotechnology*, vol. 5, no. 5, pp. 321–325, —2010—.

[56] D. C. Elias, R. R. Nair, T. M. G. Mohiuddin, S. V. Morozov, P. Blake, M. P. Halsall, A. C. Ferrari, D. W. Boukhvalov, M. I. Katsnelson, A. K. Geim, and K. S. Novoselov, "Control of graphene's properties by reversible hydrogenation: Evidence for graphane," *Science*, vol. 323, no. 5914, pp. 610–613, —2009—.

[57] X. Wu, M. Sprinkle, X. Li, F. Ming, C. Berger, and W. A. de Heer, "Epitaxial-graphene/graphene-oxide junction: An essential step towards epitaxial graphene electronics," *Physical Review Letters*, vol. 101, no. 2, p. 026801, —2008—.

[58] R. R. Nair, W. Ren, R. Jalil, I. Riaz, V. G. Kravets, L. Britnell, P. Blake, F. Schedin, A. S. Mayorov, S. Yuan, M. I. Katsnelson, H.-M. Cheng, W. Strupinski, L. G. Bulusheva, A. V. Okotrub, I. V. Grigorieva, A. N. Grigorenko, K. S. Novoselov, and A. K. Geim, "Fluorographene: A two-dimensional counterpart of teflon," *Small*, vol. 6, no. 24, pp. 2877–2884, —2010—.

[59] H. Zhang, E. Bekyarova, J. W. Huang, Z. Zhao, W. Z. Bao, F. L. Wang, R. C. Haddon, and C. N. Lau, "Aryl functionalization as a route to band gap engineering in single layer graphene devices," *Nano Letters*, vol. 11, no. 10, pp. 4047–4051, —2011—.

[60] F. J. Giessibl, "Advances in atomic force microscopy," *Reviews of Modern Physics*, vol. 75, no. 3, pp. 949–983, —2003—.

[61] E. Stolyarova, D. Stolyarov, K. Bolotin, S. Ryu, L. Liu, K. T. Rim, M. Klima, M. Hybertsen, I. Pogorelsky, I. Pavlishin, K. Kusche, J. Hone, P. Kim, H. L. Stormer, V. Yakimenko, and G. Flynn, "Observation of graphene bubbles and effective mass transport under graphene films," *Nano Letters*, vol. 9, no. 1, pp. 332–337, —2008—.

[62] T. Fukuma, K. Kobayashi, K. Matsushige, and H. Yamada, "True atomic resolution in liquid by frequency-modulation atomic force microscopy," *Applied Physics Letters*, vol. 87, no. 3, p. 3, —2005—.

[63] C. A. J. Putman, K. O. Vanderwerf, B. G. Degrooth, N. F. Vanhulst, and J. Greve, "Tapping mode atomic-force microscopy in liquid," *Applied Physics Letters*, vol. 64, no. 18, pp. 2454–2456, —1994—.

[64] S. Xu and M. F. Arnsdorf, "Electrostatic force microscope for probing surface charges in aqueous solutions," *Proceedings of the National Academy of Sciences*, vol. 92, no. 22, pp. 10384–10388, —1995—.

[65] ParkSystem EFM Manual.

[66] T. Filleter, K. V. Emtsev, T. Seyller, and R. Bennewitz, "Local work function measurements of epitaxial graphene," *Applied Physics Letters*, vol. 93, no. 13, —2008—.

[67] ParkSystem I-AFM Manual.

[68] D. Gardiner, *Pratical Raman Spectroscopy*. Springer, 1 ed., —1989—.

[69] A. C. Ferrari, J. C. Meyer, V. Scardaci, C. Casiraghi, M. Lazzeri, F. Mauri, S. Piscanec, D. Jiang, K. S. Novoselov, S. Roth, and A. K. Geim, "Raman spectrum of graphene and graphene layers," *Physical Review Letters*, vol. 97, no. 18, p. 187401, —2006—.

[70] A. C. Ferrari and J. Robertson, "Interpretation of Raman spectra of disordered and amorphous carbon," *Physical Review B*, vol. 61, no. 20, pp. 14095–14107, —2000—.

[71] L. M. Malard, J. Nilsson, D. C. Elias, J. C. Brant, F. Plentz, E. S. Alves, A. H. Castro Neto, and M. A. Pimenta, "Probing the electronic structure of bilayer graphene by Raman scattering," *Physical Review B*, vol. 76, no. 20, p. 201401, —2007—.

[72] C. Faugeras, A. Nerriere, M. Potemski, A. Mahmood, E. Dujardin, C. Berger, and W. A. de Heer, "Few-layer graphene on sic, pyrolitic graphite, and graphene: A Raman scattering study," *Applied Physics Letters*, vol. 92, no. 1, p. 3, —2008—.

[73] A. Das, S. Pisana, B. Chakraborty, S. Piscanec, S. K. Saha, U. V. Waghmare, K. S. Novoselov, H. R. Krishnamurthy, A. K. Geim, A. C. Ferrari, and A. K. Sood, "Monitoring dopants by raman scattering in an electrochemically top-gated graphene transistor," *Nature Nanotechnology*, vol. 3, no. 4, pp. 210–215, —2008—.

[74] S. A. Campbell, *Fabrication Engineering at the Micro and Nanoscale*. Oxford University Press, USA, 3rd ed., —2007—.

[75] J. N. Randall, D. C. Flanders, N. P. Economou, J. P. Donnelly, and E. I. Bromley, "High-resolution ion-beam lithography at large gaps using stencil masks," *Applied Physics Letters*, vol. 42, no. 5, pp. 457–459, —1983—.

[76] H. Namatsu, T. Yamaguchi, M. Nagase, K. Yamazaki, and K. Kurihara, "Nanopatterning of a hydrogen silsesquioxane resist with reduced linewidth fluctuations," *Microelectronic Engineering*, vol. 4142, no. 0, pp. 331–334, —1998—.

[77] V. Passi, A. Lecestre, C. Krzeminski, G. Larrieu, E. Dubois, and J.-P. Raskin, "A single layer hydrogen silsesquioxane (HSQ) based lift-off process for germanium and platinum," *Microelectronic Engineering*, vol. 87, no. 10, pp. 1872–1878, —2009—.

[78] A. E. Grigorescu, M. C. van der Krogt, C. W. Hagen, and P. Kruit, "10nm lines and spaces written in HSQ using electron beam lithography," *Microelectronic Engineering*, vol. 84, no. 58, pp. 822–824, —2007—.

[79] E. Mohajerani, F. Farajollahi, R. Mahzoon, and S. Baghery, "Morphological and thickness analysis for PMMA spin coated films," *Journal of Optoelectronics and Advanced Materials*, vol. 9, no. 12, pp. 3901–3906, —2007—.

[80] M. Lazar, H. Vang, P. Brosselard, C. Raynaud, P. Cremillieu, J. L. Leclercq, A. Descamps, S. Scharnholz, and D. Planson, "Deep SiC etching with RIE," *Superlattices and Microstructures*, vol. 40, no. 4-6, pp. 388–392, —2006—.

[81] G. Saggio, E. Verona, P. Di Rosa, S. La Monica, R. Salotti, and L. Schirone, "Reactive ion etching characterization of α-SiC: H in CF_4/O_2 plasma," *Materials Science and Engineering: B*, vol. 29, no. 1-3, pp. 176–180, —1995—.

[82] Y. Xuan, Y. Q. Wu, T. Shen, M. Qi, M. A. Capano, J. A. Cooper, and P. D. Ye, "Atomic-layer-deposited nanostructures for graphene-based nanoelectronics," *Applied Physics Letters*, vol. 92, no. 1, p. 3, —2008—.

[83] R. Burdett, "Amplitude modulated signals: The lock-in amplifier," in *Handbook of Measuring System Design*, John Wiley & Sons, Ltd, —2005—.

[84] H. Morkoc, S. Strite, G. B. Gao, M. E. Lin, B. Sverdlov, and M. Burns, "Large-band-gap SiC, III-V nitride, and II-VI ZnSe-based semiconductor-device technologies," *Journal of Applied Physics*, vol. 76, no. 3, pp. 1363–1398, —1994—.

[85] H. P. Boehm, A. Clauss, U. Hofmann, and G. O. Fischer, "Dunnste kohlenstoff-folien," *Zeitschrift Fur Naturforschung Part B-Chemie Biochemie Biophysik Biologie Und Verwandten Gebiete*, vol. B 17, no. 3, pp. 150–153, —1962—.

[86] P. L. McEuen, M. S. Fuhrer, and H. K. Park, "Single-walled carbon nanotube electronics," *IEEE Transactions on Nanotechnology*, vol. 1, no. 1, pp. 78–85, —2002—.

[87] D. E. Soule and J. W. McClure, "Band structure and transport properties of single-crystal graphite," *Journal of Physics and Chemistry of Solids*, vol. 8, pp. 29–35, —1959—.

[88] R. M. Tromp and J. B. Hannon, "Thermodynamics and kinetics of graphene growth on sic(0001)," *Physical Review Letters*, vol. 102, no. 10, —2009—.

[89] K. V. Emtsev, A. Bostwick, K. Horn, J. Jobst, G. L. Kellogg, L. Ley, J. L. McChesney, T. Ohta, S. A. Reshanov, J. Roehrl, E. Rotenberg, A. K. Schmid, D. Waldmann, H. B. Weber, and T. Seyller, "Towards wafer-size graphene layers by atmospheric pressure graphitization of silicon carbide," *Nature Materials*, vol. 8, no. 3, pp. 203–207, —2009—.

[90] D. L. Miller, K. D. Kubista, G. M. Rutter, M. Ruan, W. A. de Heer, P. N. First, and J. A. Stroscio, "Observing the quantization of zero mass carriers in graphene," *Science*, vol. 324, no. 5929, pp. 924–927, —2009—.

[91] Y. J. Song, A. F. Otte, Y. Kuk, Y. Hu, D. B. Torrance, P. N. First, W. A. de Heer, H. Min, S. Adam, M. D. Stiles, A. H. MacDonald, and J. A. Stroscio, "High-resolution tunnelling spectroscopy of a graphene quartet," *Nature*, vol. 467, no. 7312, pp. 185–189, —2010—.

[92] M. Sprinkle, M. Ruan, Y. Hu, J. Hankinson, M. Rubio-Roy, B. Zhang, X. Wu, C. Berger, and W. A. de Heer, "Scalable templated growth of graphene nanoribbons on sic," *Nature Nanotechnology*, vol. 5, no. 10, pp. 727–731, —2010—.

[93] J. Hass, F. Varchon, J. E. Millan-Otoya, M. Sprinkle, N. Sharma, W. A. De Heer, C. Berger, P. N. First, L. Magaud, and E. H. Conrad, "Why multilayer graphene on 4H-SiC(000-1) behaves like a single sheet of graphene," *Physical Review Letters*, vol. 100, no. 12, —2008—.

[94] S. K. Lilov, "Study of the equilibrium processes in the gas-phase during silicon-carbide sublimation," *Materials Science and Engineering B-Solid State Materials for Advanced Technology*, vol. 21, no. 1, pp. 65–69, —1993—.

[95] D. Hoffman, B. Singh, and J. I. Thomas, *Handbook of Vacuum Science and Technology*. Academic Press, —1997—.

[96] S. Y. Zhou, G. H. Gweon, A. V. Fedorov, P. N. First, W. A. De Heer, D. H. Lee, F. Guinea, A. H. C. Neto, and A. Lanzara, "Substrate-induced bandgap opening in epitaxial graphene," *Nature Materials*, vol. 6, no. 10, pp. 770–775, —2007—.

[97] J. Hicks, K. Shepperd, F. Wang, and E. H. Conrad, "The structure of graphene grown on the SiC (000-1) surface," *Journal of Physics D: Applied Physics*, vol. 45, no. 15, p. 154002, —2010—.

[98] M. Sprinkle, J. Hicks, A. Tejeda, A. Taleb-Ibrahimi, P. Le Fevre, F. Bertran, H. Tinkey, M. C. Clark, P. Soukiassian, D. Martinotti, J. Hass, and E. H. Conrad, "Multilayer epitaxial graphene grown on the sic (000-1) surface; structure and electronic properties," *Journal of Physics D-Applied Physics*, vol. 43, no. 37, —2010—.

[99] W. A. de Heer, C. Berger, X. Wu, P. N. First, E. H. Conrad, X. Li, T. Li, M. Sprinkle, J. Hass, M. L. Sadowski, M. Potemski, and G. Martinez, "Epitaxial graphene," *Solid State Communications*, vol. 143, no. 1-2, pp. 92–100, —2007—.

[100] J. Hass, J. E. Millan-Otoya, P. N. First, and E. H. Conrad, "Interface structure of epitaxial graphene grown on 4h-SiC(0001)," *Physical Review B*, vol. 78, no. 20, —2008—.

[101] D. Sun, Z.-K. Wu, C. Divin, X. Li, C. Berger, W. A. de Heer, P. N. First, and T. B. Norris, "Ultrafast relaxation of excited dirac fermions in epitaxial graphene using optical differential transmission spectroscopy," *Physical Review Letters*, vol. 101, no. 15, —2008—.

[102] D. Sun, C. Divin, C. Berger, W. A. de Heer, P. N. First, and T. B. Norris, "Spectroscopic measurement of interlayer screening in multilayer epitaxial graphene," *Physical Review Letters*, vol. 104, no. 13, p. 136802, —2009—.

[103] Y. Hu, M. Ruan, Z. Guo, R. Dong, J. Palmer, J. Hankinson, C. Berger, and W. A. de Heer, "Structured epitaxial graphene: growth and properties," *Journal of Physics D-Applied Physics*, vol. 45, no. 15, p. 154010, —2012—.

[104] W. A. de Heer, C. Berger, and P. N. First, "Patterned thin film graphite devices and method for making same," —2006—.

[105] A. Javey, J. Guo, Q. Wang, M. Lundstrom, and H. J. Dai, "Ballistic carbon nanotube field-effect transistors," *Nature*, vol. 424, no. 6949, pp. 654–657, —2003—.

[106] S. Frank, P. Poncharal, Z. L. Wang, and W. A. de Heer, "Carbon nanotube quantum resistors," *Science*, vol. 280, no. 5370, pp. 1744–1746, —1998—.

[107] J. B. Oostinga, B. Sacp, M. F. Craciun, and A. F. Morpurgo, "Magnetotransport through graphene nanoribbons," *Physical Review B*, vol. 81, no. 19, p. 193408, —2010—.

[108] P. Gallagher, K. Todd, and D. Goldhaber-Gordon, "Disorder-induced gap behavior in graphene nanoribbons," *Physical Review B*, vol. 81, no. 11, p. 115409, —2010—.

[109] J. Kedzierski, P.-L. Hsu, P. Healey, P. W. Wyatt, C. L. Keast, M. Sprinkle, C. Berger, and W. A. de Heer, "Epitaxial graphene transistors on SiC substrates," *IEEE Transactions on Electron Devices*, vol. 55, no. 8, pp. 2078–2085, —2008—.

[110] J. S. Moon, D. Curtis, M. Hu, D. Wong, C. McGuire, P. M. Campbell, G. Jernigan, J. L. Tedesco, B. VanMil, R. Myers-Ward, J. Eddy, C., and D. K. Gaskill, "Epitaxial-graphene RF field-effect transistors on Si-face 6H-SiC substrates," *IEEE Electron Device Letters*, vol. 30, no. 6, pp. 650–652, —2009—.

[111] R. Krithivasan, Y. Lu, J. D. Cressler, J. S. Rieh, M. H. Khater, D. Ahlgren, and G. Freeman, "Half-terahertz operation of SiGeHBTs," *IEEE Electron Device Letters*, vol. 27, no. 7, pp. 567–569, —2006—.

[112] K. Wakabayashi, Y. Takane, M. Yamamoto, and M. Sigrist, "Edge effect on electronic transport properties of graphene nanoribbons and presence of perfectly conducting channel," *Carbon*, vol. 47, no. 1, pp. 124–137, —2009—.

[113] K. Wakabayashi, Y. Takane, and M. Sigrist, "Perfectly conducting channel and universality crossover in disordered graphene nanoribbons," *Physical Review Letters*, vol. 99, no. 3, p. 036601, —2007—.

[114] V. V. Cheianov and V. I. Falko, "Selective transmission of dirac electrons and ballistic magnetoresistance of n-p junctions in graphene," *Physical Review B*, vol. 74, no. 4, p. 041403, —2006—.

[115] S. Belaidi, F. Lebon, P. Girard, G. Leveque, and S. Pagano, "Finite element simulations of the resolution in electrostatic force microscopy," *Applied Physics a-Materials Science & Processing*, vol. 66, pp. S239–S243, —1998—.

[116] D. S. Lee, C. Riedl, B. Krauss, K. von Klitzing, U. Starke, and J. H. Smet, "Raman spectra of epitaxial graphene on SiC and of epitaxial graphene transferred to SiO_2," *Nano Letters*, vol. 8, no. 12, pp. 4320–4325, —2008—.

[117] M. Bockrath, D. H. Cobden, J. Lu, A. G. Rinzler, R. E. Smalley, L. Balents, and P. L. McEuen, "Luttinger-liquid behaviour in carbon nanotubes," *Nature*, vol. 397, no. 6720, pp. 598–601, —1999—.

[118] C. Schonenberger, A. Bachtold, C. Strunk, J. P. Salvetat, and L. Forro, "Interference and interaction in multi-wall carbon nanotubes," *Applied Physics a-Materials Science & Processing*, vol. 69, no. 3, pp. 283–295, —1999—.

[119] C. W. J. Beenakker and H. Vanhouten, "Quantum transport in semiconductor nanostructures," *Solid State Physics-Advances in Research and Applications*, vol. 44, pp. 1–228, —1991—.

[120] T. Ando, T. Nakanishi, and R. Saito, "Berry's phase and absence of back scattering in carbon nanotubes," *Journal of the Physical Society of Japan*, vol. 67, no. 8, pp. 2857–2862, —1998—.

[121] C. Stampfer, J. Gttinger, S. Hellmller, F. Molitor, K. Ensslin, and T. Ihn, "Energy gaps in etched graphene nanoribbons," *Physical Review Letters*, vol. 102, no. 5, p. 056403, —2009—.

[122] B. Huard, J. A. Sulpizio, N. Stander, K. Todd, B. Yang, and D. Goldhaber-Gordon, "Transport measurements across a tunable potential barrier in graphene," *Physical Review Letters*, vol. 98, no. 23, p. 236803, —2007—.

[123] A. Rycerz, J. Tworzydlo, and C. W. J. Beenakker, "Valley filter and valley valve in graphene," *Nat Phys*, vol. 3, no. 3, pp. 172–175, —2007—.

[124] T. Ando and H. Suzuura, "Presence of perfectly conducting channel in metallic carbon nanotubes," *Journal of the Physical Society of Japan*, vol. 71, no. 11, pp. 2753–2760, —2002—.

[125] W. Norimatsu and M. Kusunoki, "Formation process of graphene on SiC (0001)," *Physica E-Low-Dimensional Systems & Nanostructures*, vol. 42, no. 4, pp. 691–694, —2010—.

[126] Y.-W. Son, M. L. Cohen, and S. G. Louie, "Energy gaps in graphene nanoribbons," *Physical Review Letters*, vol. 97, no. 21, p. 216803, —2006—.

[127] T. Shimizu, J. Haruyama, D. C. Marcano, D. V. Kosinkin, J. M. Tour, K. Hirose, and K. Suenaga, "Large intrinsic energy bandgaps in annealed nanotube-derived graphene nanoribbons," *Nature Nanotechnology*, vol. 6, no. 1, pp. 45–50, —2011—.

[128] X. Wang, Y. Ouyang, X. Li, H. Wang, J. Guo, and H. Dai, "Room-temperature all-semiconducting sub-10-nm graphene nanoribbon field-effect transistors," *Physical Review Letters*, vol. 100, no. 20, p. 206803, —2008—.

[129] P. R. Bandaru, C. Daraio, S. Jin, and A. M. Rao, "Novel electrical switching behaviour and logic in carbon nanotube Y-junctions," *Nature Materials*, vol. 4, no. 9, pp. 663–666, —2005—.

VITA

Ming Ruan was born in Hangzhou, China. He received his B.S. degree in Peking University, Beijing, China in 2007. Then he moved to Atlanta to join the epitaxial graphene lab in Georgia Tech, under the supervision of Professor Walt A. de Heer. His major research areas are epitaxial graphene growth, nanoelectronic device fabrication, and electron transport measurement.